A Detailed Study of the Rotational Augmentation and Dynamic Stall Phenomena for Wind Turbines

Guntur, Srinivas

Publication date:
2013

Document Version
Publisher's PDF, also known as Version of record

A Detailed Study of the Rotational Augmentation and Dynamic Stall Phenomena for Wind Turbines

DTU Vindenergi
PhD Rapport 2013

Srinivas K. Guntur

DTU Wind Energy PhD-0022 (EN)

December 2013

DTU Vindenergi
Institut for Vindenergi

Author: Srinivas K. Guntur
Title: A Detailed Study of the Rotational Augmentation and Dynamic Stall Phenomena for Wind Turbines
Department: Wind Energy

DTU Wind Energy PhD-0022 (EN)
December 2013

Summary (max 2000 characters):
This thesis presents investigations into the aerodynamics of wind turbine rotors, with a focus on the in-board sections of the rotor. Two important aerodynamic phenomena that have challenged scientists over nearly the last half a century are the so-called rotational augmentation and dynamic stall. This thesis presents an investigation into these two phenomena, using data from the MEXICO and the NREL UAE Phase VI experiments, as well as data obtained from full rotor CFD computations carried out using the in-house flow solver Ellipsys3D. The experimental data, CFD data and that from some of the existing reduced order engineering models were analysed to understand rotational augmentation and dynamic stall from a modelling perspective.

The first part of the analysis is concerned with steady state aerodynamics. Data from experiments and CFD were analysed in comparison with some of the existing rotational augmentation models, and the relative advantages of these models have been highlighted. The differences between separation characteristics on an airfoil in stationary vs. rotating conditions have not been clarified in the existing literature on this subject. Detailed flow field data obtained using full rotor CFD data was analysed to identify these differences. Comments are made on the mechanism of stall delay, and the main differences between the skin friction and pressure distribution behaviours in 2D and 3D rotating flows are highlighted.

In a second part of this analysis, dynamic stall has been studied on wind turbine blades using the N-sequence data of the NREL UAE Phase VI experiment. The experimental data is compared with the results from unsteady Delayed Detached Eddy Simulations (DDES). The same conditions are also modelled using a Beddoes-Leishman type dynamic stall model by Hansen et al. (2004), using rotationally augmented steady state polars as the input instead of the typically used 2D (stationary) data. The aim of this part of the work has been to investigate the differences between the stall phenomenon on harmonically pitching blades on a rotating wind turbine and the classic dynamic stall representation in 2D flow, as adopted by the reduced order models used for Blade Element Momentum (BEM) based aeroelastic simulations.

It has been found that by modelling rotational augmentation and dynamic stall, a more accurate representation of rotor aerodynamics is possible. However higher quantitative accuracy of reduced order modelling maybe limited due to the fact that modelling separated flow is a challenge, even using more rigorous methods such as CFD. It has also been identified that a span-wise variation in the blade loading has an influence on the aerodynamics of the sections nearby. This influence, which has to do with trailing of vorticity, is similar to the tip effect and has been found to be important to be corrected for when using BEM based simulation codes. Additionally, comments are made on the use of the inverse BEM method as a means of determining the angle of attack on wind turbine blades in steady as well as in unsteady conditions.

Supervisor(s):
Niels N. Sørensen

Pages: 111
References: 103

Danmarks Tekniske Universitet
Risø Campus
DTU Vindenergi
Building 115
Frederiksborgvej 399
Roskilde 4000
Denmark
www.vindenergi.dtu.dk

Résumé

Denne afhandling beskæftiger sig med vindmølleaerodynamik, med særlig fokus på de indre spanvise dele af vingerne. To vigtige emner, som har beskæftiget forskere i mere end et halvt århundrede er de såkaldte 'stall delay' og dynamisk stall effekter. Det foreliggende Ph.D. arbejde præsenterer en undersøgelse af disse to fænomener ved brug af data fra henholdsvis, MEXICO og NREL UAE Phase VI eksperimenterne, og fra fuldt opløste 3D rotor CFD beregninger lavet med DTU's Navier Stokes kode EllipSys3D. Analyser baseret på disse eksperimentelle og beregnede data samt data fra eksisterende enginiør modeller er udnyttet til a forbedre forståelsen af 'stall delay' og dynamisk stall.

Den første del af analysen fokuserer på stationær aerodynamik. Data fra eksperimenter og CFD analyseres og sammenlignes med adskillige ingeniørmodeller for 'stall delay', og modellernes individuelle fordele og ulemper vurderes. Forskellen mellem separationskarakteristikken for et vingeprofil i stationære og rotorende forhold er ikke fuldt dokumenteret i litteraturen. Det nærværende Ph.D arbejde laver, med udgangspunkt i 3D rotor CFD beregninger, en detaljeret analyse af strømningsfeltet for at identificere disse forskelle. Der kommenteres på mekanismen der ligger til grund for 'stall delay' og sættes fokus på de primære forskelle mellem friktions- og trykfordelinger på profiler i 2D og 3D roterende strømninger.

I den sidste del af arbejdet, analyseres dynamisk stall på vindmøllevinger ved brug af data fra NREL UAE Phase-VI eksperimentet, N-series data. De eksperimentielle data sammenlignes med resultater fra Delayed Detached Eddy Simulations (DDES). Yderligere sammenlignes med en Beddoes-Leishman baseret dynamisk stall model udviklet af Hansen et al. (2004), hvor 3D korrigerede profildata anvendes i stedet for standard 2D profildata. Hovedformålet med denne del af studiet, er at undersøge forskellene mellem dynamisk stall på vinger under en harmonisk variation af pitchvinklen og den typiske 2D dynamisk stall repræsentation, der ofte anvendes i aeroelastiske koder.

Det nærværende studie har vist at man ved brug af modeller for 'stall delay' og dynamisk stall, kan opnå en bedre forudsigelse af lasterne på rotorer. Det er dog stadig klart, at problemer med modellering af separeret strømning, selv ved brug af fulde 3D CFD beregninger, er en kilde til unøjagtighed. Studiet har desuden vist, at ved store spanvise variationer i lasterne, er antagelsen i BEM om radial uafhængighed ikke længere gyldig, noget der kan være væsentlig i specielle lastsituationer. Yderligere er der som en central del af studiet arbejdet med bestemmelse af indfaldsvinkler ved brug af en 'Inverse BEM' teknik, som er vist at være den bedst tilgængelige teknik både for statiske og dynamiske situationer.

Acknowledgements

First and foremost, I would like to express my deep gratitude towards my supervisor, Prof. Niels N. Sørensen, for his guidance and seemingly endless patience. I have learned a lot in the last three years working with him.

I would also like to thank the Aeroelastic Design (AED) staff for the academic support I received from several members, as well as for the hilarious lunch-table conversations on everything ranging from highly important issues to not-so-important issues. It has made my stay at the department very pleasant.

I would like to thank Prof. Scott Schreck for his support during and after my external research stay at NREL, USA, during Summer 2012.

This work was a part of project *SYSWIND*, funded by the European Commission under the framework FP7 programme *Marie Curie*. I would like to thank the organizers of *SYSWIND*, particularly Prof. Biswajith Basu (Trinity College Dublin, Ireland), for the number of summer schools and seminars organized as a part of this project.

Last but most definitely not the least, cheers to all of the fellow PhD students at the wind energy division−particularly my officemates, Carlo, David, Ivan, Joachim, Leo and Witold, for helping maintain an atmosphere in our office that is not only congenial for work, but also pleasant, informal and light-hearted, and hence memorable.

In theory there is no difference between theory and practice. In practice there is.

Yogi Berra

Contents

List of Figures

List of Tables

Nomenclature

α	Angle of attack [°]
β	Blade pitch angle [°]
μ	Dynamic viscosity of air [kg/m s]
ν	Kinematic viscosity of air [m/s]
Ω	Blade pitching frequency [rad/s]
ω	Rotor rotation speed [rad/s]
ϕ	Local inflow angle [°]
θ	Local twist [°]
a	Axial induction factor [-]
a'	Tangential induction factor [-]
B	Number of blades [-]
c	Airfoil chord [m]
C_D	Coefficient of drag [-]
C_L	Coefficient of lift [-]
C_N	Normal force coefficient, normal to the airfoil chord [-]
c_p	Coefficient of pressure [-]
C_T	Tangential force coefficient, along the airfoil chord [-]
CN	Normal force coefficient, normal to the rotor plane [-]
CT	Tangential force coefficient, in the rotor plane [-]
K	Reduced frequency of pitching [-]
R	Rotor radius [m]
r	Radial distance from the rotor axis [m]
U_∞	Free stream wind velocity [m/s]
Re	Reynolds number [-]

Chapter 1

Introduction

The importance of renewable energy in tomorrow's energy market becomes evident from the energy policies of different nations, both developed and developing, around the world for the next few decades. According to the International Energy Agency's report World Energy Outlook 2012, the projected share of renewables in the worldwide electricity generation reaches 31% by 2035, a quarter of which is from wind power alone [5]. It is for this reason, despite the basic concept of generating power from wind being centuries old, that research in wind turbine engineering is rapidly gaining interest today. Wind turbine engineering consists of many different fields within, e.g., structural design, aerodynamics, control engineering, planning and economics. This thesis is concerned with the aerodynamics of wind turbines.

1.1 Background

Schepers [6] explains that wind energy aerodynamics can be divided into two areas: rotor aerodynamics and wind farm aerodynamics. The current work is related to the former area. In order to study wind turbine rotor aerodynamics, one needs to be able to model the rotor at its operating conditions and its interaction with the wind to a certain degree of accuracy. Several techniques exist by which this is traditionally done, e.g. Computational Fluid Dynamics (CFD) methods, vortex methods, and Blade Element Momentum (BEM) methods, each having their own advantages. With increasing focus on lowering the cost of a wind turbine over its lifetime, there is a need to improve models used for the design of the wind turbine. With the advent of faster computers, there has been a significant reduction in the computational time of the CFD methods, but they still remain too expensive to be used as aeroelastic design codes. In fact, all modern aeroelastic design codes are based on the BEM theory owing to its simplicity

[7]. The BEM-based methods are inherently much faster than the CFD methods, but they are not capable of modelling all of the aerodynamic phenomena that occur on a real turbine. Therefore, the task of improving the aerodynamic models to be both cheap and accurate leads to two possible strategies: improving the accuracy of the BEM based codes, or drastically decreasing the costs of computational methods. The latter may be a possibility in future, but with the current technology the former is a more feasible strategy.

The BEM theory models a wind turbine with the help of a set of ideal assumptions, discussed in Chapter 2. Engineering add-ons are typically used in the BEM-based codes to correct for the aerodynamic effects present on a real turbine that are not modelled in the classical BEM. The following are some examples:

For simplicity, the wind turbine rotor is assumed to be an actuator disc of infinite number of blades in the BEM theory. As a result, modelling a real rotor with finite number of blades introduces an error in the loads estimated in the tip region. To correct for these effects, tip loss correction factors are used, e.g., see [8–11].

The rotor of a real wind turbine is supported by a tower. The presence of the tower influences the incoming wind, and its effect is felt by the blade every time it passes the tower. This effect must be taken into account using a tower model, e.g., see [12].

BEM codes require the lift and drag polars of the airfoils used on the rotor blades as an input. Typically, the lift and drag polars are determined using wind tunnel experiments of the airfoil sections in uni-directional flow, or from 2D CFD computations. It is observed that often the measured lift in the inboard parts of a rotor are higher than the corresponding 2D value. This effect is called the rotational augmentation effect, and is described in detail in Chapter 4.

When an airfoil undergoes an unsteady change in its angle of attack, a phenomenon known as dynamic stall occurs, where the airfoil temporarily experiences lift coefficients that are significantly different than its 2D values [13]. This can happen due to unsteady effects such as yawed flow, inflow turbulence, wind shear, etc. Various dynamic stall models exist which can be used with BEM codes, see [13].

1.2 Current work

There has been significant effort in each of these areas over the last few decades, as highlighted in [6]. However, some uncertainty in the estimation of loads in the inboard parts of the blades remains today, despite the years of research in this area. The aim of

this thesis is to present a detailed analysis of the rotational augmentation and dynamic stall phenomena on wind turbines. The analysis presented in this thesis can be divided into two parts: the first part addresses rotational augmentation, and the second presents an analysis of dynamic stall together with rotational augmentation.

The purpose of the first part of the analysis has been to address the following two issues:

1. Investigation of the behaviour of the existing engineering models for rotational augmentation (described in Chapter 2). This has been done by applying them to the MEXICO and NREL Phase VI rotors (see [14] and [2], respectively) and comparing them with the experimental data.

2. Investigation of the difference between the flow around an airfoil in 2D flow and on a rotating blade, at a given angle of attack. The experimental data available is limited in resolution and the parameters measured, and a thorough analysis would require a more comprehensive database. Therefore, full rotor CFD computations of the MEXICO rotor were carried out, as will be discussed in Chapter 3. In this part of the study, the surface pressure and skin friction data obtained from CFD computations were used for detailed analysis of the flow around the wind turbine blades.

The second part of the study is concerned with dynamic stall on wind turbine blades. As will be highlighted in Section 2.4, rotational augmentation and dynamics stall have been studied in the past, but independently. The aim of this part of the thesis has been to investigate dynamic stall together with rotational augmentation. The N sequence NREL Phase VI data, which, as will be explained in Chapter 3, consists of a continuously pitching rotor in axial operation. Such data is useful in analysing the effects of dynamic stall and rotational augmentation independently and together. Computational data was also made available by carrying out unsteady CFD computations for the same operating conditions as a few select N sequence cases. This way, comparison between the CFD data and the experimental data yielded a validation of the CFD computations, and comparison between the experimental data and that from the model yielded a validation of the model.

Finally, a case study is presented where selected cases of the N sequence NREL phase VI experiment were simulated using a BEM code, with a chosen rotational augmentation model and a dynamic stall model. The results from this simulation are discussed in comparison with experimental data.

1.3 Publications

A part of the work presented in this thesis has been (or is being) disseminated through the following publications:

- Guntur, S., Sørensen, N.N., Schreck, S., Bergami, L., "Modelling dynamic stall on wind turbine blades under rotationally augmented flow fields". *J. of Wind Energy.* Submitted, September 2013.
- Guntur, S., Sørensen, N.N., "A study on rotational augmentation using CFD analysis of flow in the inboard region of the MEXICO rotor blades". *J. of Wind Energy.* Accepted, August 2013.
- Guntur, S., Sørensen, N.N., "Comments on the research article by Gross et al. (2012)". Letter to the editor, *J. of Wind Energy.* Accepted, August 2013.
- Guntur, S., Sørensen, N.N., Schreck, S. "Dynamic stall on rotating airfoils: A look at the N-sequence data from the NREL Phase VI experiment". *Key Engineering Materials Journal*, 569-570:611-619, July 2013. ISSN 1662-9795.
- Guntur, S., Sørensen, N.N., "An evaluation of several methods of determining the local angle of attack on wind turbine blades". Proc. of Science of Making Torque from Wind, October 2012, Oldenburg, Germany.
- Guntur, S., Bak, C., Sørensen, N.N. "Analysis of 3D Stall Models for Wind Turbine Blades Using Data from the MEXICO Experiment". Proc. of the 13^{th} International Conference on Wind Engineering (ICWE), 2011, Amsterdam, the Netherlands.

1.4 Layout

The layout of this thesis is as follows.

Chapter 2. The next chapter will introduce the reader to the necessary theory of the aerodynamics of wind turbines. The BEM methodology as well as the phenomena of rotational augmentation and dynamic stall are described herein, along with their importance relative to the aeroelastic modelling of wind turbines.

Chapter 3. Analysis in this thesis was carried out using data from two large scale experiments, the MEXICO and the NREL Phase VI experiments, as well as a set of full rotor CFD computations. The details on these data are described, along with a description of the data processing involved.

Chapter 4. This chapter presents the results from the study on rotational augmentation. Lift and drag polars corrected using a set of selected existing rotational augmentation models are compared with the experimental/CFD data and the results are discussed. Thereafter, surface flow patters are studied using the pressure and skin friction data in the inboard locations of the rotor, and these results are discussed.

Chapter 5. This chapter presents the results from the second part of the study, on dynamic stall on the inboard parts of the rotor. Comparisons were made between the CFD data and the experimental data, and later between the experimental data and that from a reduced order model.

Chapter 6. This chapter presents a case study where the NREL Phase VI rotor was simulated using a BEM model along with a rotational augmentation model and a dynamic stall model, for a given set of continuously pitching cases in axial operation. The results from this simulation were compared with those from the experiment, and a discussion on the same is presented.

Chapter 7. The final chapter presents a summary of the work that was presented in the previous chapters, along with recommendations for future work.

Chapter 2

Aerodynamic models

In this chapter, the reader is introduced to the two aerodynamic phenomena that are investigated in this thesis, rotational augmentation and dynamic stall. In order to understand the scope of this study, it is useful to review the BEM theory first.

2.1 The Blade Element Momentum Theory

A wind turbine is a machine that extracts kinetic energy from the wind. As a result, the wind loses momentum as it passes through the rotor. Since wind is not a point mass object but rather a continuum of fluid particles, the loss in its momentum occurs over a control volume far upstream and downstream of the rotor as governed by the equations of conservation of momentum and mass for fluids. Betz and Joukowsky were some of the first to derive an expression for the efficiency for an ideal rotor using a one dimensional momentum theory by approximating the rotor as an actuator disc, as highlighted in [15]. Glauert later developed the 1D momentum theory into a more general theory, which is commonly known as the Blade Element Momentum (BEM) theory [8]. In this method, the rotor is modelled as a series of blade elements, and an iterative process is used to obtain a balance between the forces on the blade elements and the forces on the flow field determines various parameters like the total power, rotor thrust, blade loads, etc.

The BEM theory operates on two fundamental assumptions: that there is no radial dependency, and that forces can be averaged over the individual annuli. Figure 2.1 shows a schematic of an annulus at a radial location r with thickness dr around a three-bladed wind turbine. According to the assumptions, the forces and velocities inside this annular element are not influenced by any other annular element and therefore a wind turbine can be divided into N number of concentric annuli and forces in each annulus

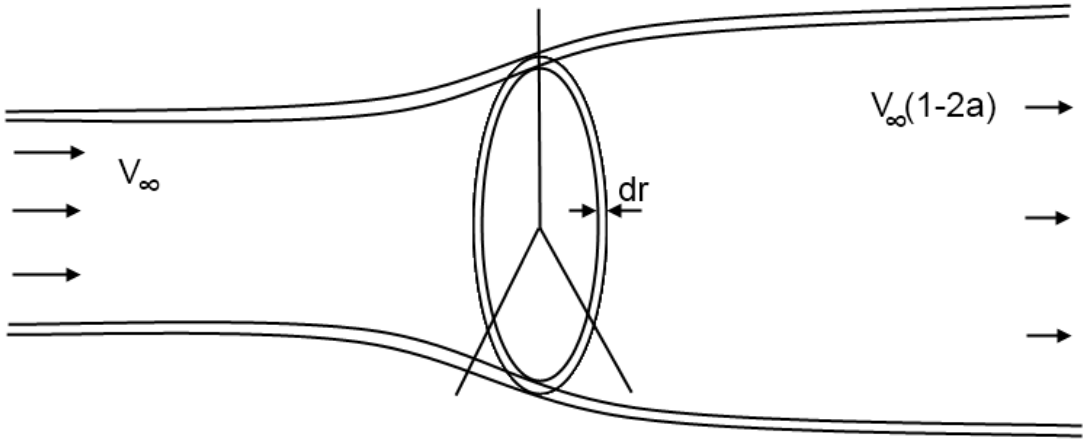

FIGURE 2.1: Schematic of a wind turbine and the annular control volume showing expansion as it passes from upstream of the rotor to downstream.

can be calculated independently. By the second assumption, the average force on the flow field in the annulus is equal to the sum of the forces on the thee individual blade elements. Based on these two assumptions, the idea is to find a balance between the force exerted on the flow field by the blade elements, and the change in the momentum of the fluid between the locations far upstream and far downstream of the rotor.

The classical BEM theory is described in several texts in various levels of detail, e.g., [12, 16]. As an algorithm, it can be summarized as follows.

1. Initialize the axial a and the tangential a' induction factors, typically $a = a' = 0$. The axial induction factor is defined as

$$a = 1 - \frac{U_{ax}}{U_\infty},$$
$$a' = \frac{U_{rot}}{\omega r} - 1, \tag{2.1}$$

   where U_{ax} and U_{rot} are the axial and tangential components of the wind velocity relative to the blade at the rotor plane, respectively.

2. Compute the inflow angle (defined in Figure 2.2)

$$\phi = \frac{(1-a)U_\infty}{(1+a')\Omega r}. \tag{2.2}$$

3. Compute the local angle of attack as $\alpha = \phi - \theta$.

4. Obtain the lift and drag force coefficients, typically a table look up.

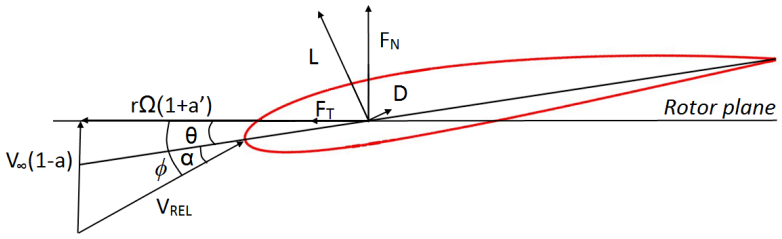

FIGURE 2.2: Schematic the definitions of angles around the airfoil.

5. Compute the normal and tangential forces as

$$\begin{aligned} CN &= C_L \cos\phi + C_D \sin\phi \\ CT &= C_L \sin\phi - C_D \cos\phi. \end{aligned} \tag{2.3}$$

6. Calculate axial and tangential induction as

$$\begin{aligned} a_{new} &= \frac{1}{\frac{4F\sin^2\phi}{\sigma CN} + 1}, \\ a'_{new} &= \frac{1}{\frac{4F\sin\phi\cos\phi}{\sigma CT} - 1}, \end{aligned} \tag{2.4}$$

   where, CN and CT are the thrust and the torque forces perpendicular and parallel to the rotor plane, respectively, and σ is the local solidity defined as:

$$\sigma(r) = \frac{c(r)B}{2\pi r}, \tag{2.5}$$

   and F is a correction factor for tip losses.

7. If the difference between the new vales of $[a_{new},\ a'_{new}]$ and $[a,\ a']$ is more than a certain tolerance, go to step 2. Else, continue.

8. Compute ϕ using Equation 2.2, and there after the local AOA and the loads on the blades.

2.1.1 Limitations of the BEM theory

As a trade off to its simplicity and computational efficiency, the classical BEM method has some limitations. The input to the BEM algorithm outlined above are steady lift and drag polars which are often 2D data, which imposes limitations on modelling unsteady conditions or if flow over certain sections of the blade is significantly different from 2D.

The assumption of annular independence works well in the mid board parts of the blade, but it fails close to the tip and the root regions where the flow is predominantly 3D, and the 2D lift and drag polars cannot be used without being corrected. In the tip region, correction factors are used to accurately compute the forces in this region, for example the tip-loss factor F in Equation 2.4 above (see [11]). In the root region, it is commonly observed that the measured lift force on an operating turbine is significantly higher than its 2D value [17]. In addition, the BEM theory is designed for small induction ($a << 1$) and so a correction is applied for turbines operating at high induction (typically $a > 0.3$), see [12]. Finally, unsteady effects such as dynamic stall need to be corrected for as well [13]. All these aerodynamic effects that are not modelled by the BEM theory are accounted for using engineering correction models [6]. Even after several decades of research in this area, there is little consensus on not only the engineering models used to account for some of these phenomenon, but even the physics underlying them−particularly rotational augmentation and dynamic stall close to the root region of the blade.

This thesis is concerned with rotational augmentation and dynamic stall modelling. In the following sections, these two phenomenon are introduced, the understanding of the physical phenomenon based on existing literature is presented, and some of the existing engineering models aiming to correct for these effects in a BEM based codes are briefly described.

2.2 Rotational augmentation

Rotational augmentation, also referred to as the stall-delay effect, is a phenomenon in which airfoils at the inboard parts of rotors experience lift which is higher than that seen in 2D flow conditions at the same angle of attack. In literature, it has been documented a number of times that the observed thrust experienced by the inboard parts of a rotating blade is higher than that predicted by the classical BEM models, starting with the widely-known experiments of Himmelskamp in 1945 on propellers (as highlighted by [18], for example). Its importance within wind turbine aerodynamics has been realized over time. Even though modern wind turbines are pitch regulated and do not use stall as a control mechanism, stall is unavoidable in the inner part of the blades when rated power is obtained.

Figure 2.3 shows an example of the $C_L - \alpha$ curve extracted from the $r/R = 0.30$ section of the NREL Phase VI rotor (described in Chapter 3) and wind tunnel data from a static airfoil section. The disagreement between the two curves can be attributed to two different physical phenomenon. The trailing root vortex influences the aerodynamics of

the sections that are close to the root. This effect is most conspicuous at small angles of attack; for example the difference in slope between the 2D and 3D lift polars in Figure 2.3 in the region $\alpha < 10°$. The second and more prominent deviation occurs between the two lift curves occurs in the separated region, $10° < \alpha < 35°$. This is the so-called rotational augmentation effect.

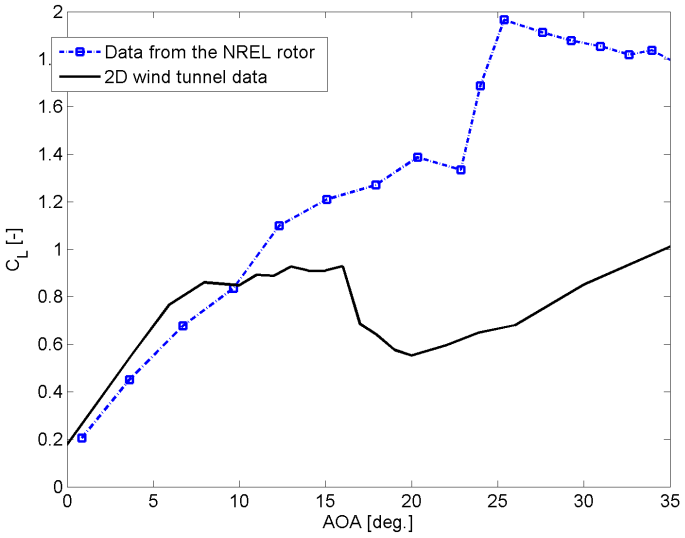

FIGURE 2.3: An example illustrating rotational augmentation of lift in wind turbines: the $C_L - \alpha$ curve for an $s809$ airfoil obtained from a 2D wind tunnel test and at the radial location $r/R = 0.30$ on the operating NREL Phase VI rotor.

2.2.1 Previous research

Banks and Gadd [18] were perhaps some of the first to investigate this problem analytically by writing down simplified laminar boundary layer equations and solving for the separation point for rotating and non-rotating cases. Their analysis suggested that the separation line moves towards the trailing edge in rotation, and they claimed that this is the cause of the observed augmentation in lift. Several experimental and numerical studies have been performed since then to get a better insight into the flow physics. Although there has been consensus that rotational augmentation indeed causes higher loads on the blades, the dominant physical phenomena responsible for this effect have not been clarified. For example, the effect of rotation on separation point location on the airfoil suction side, its effect on the pressure distribution around the airfoil, and the influence of turbulence on separation in rotation, are some issues that are still open and receive a lot of attention. As a result, the capabilities of the derived engineering models are limited.

McCroskey [19] carried out an experimental analysis and concluded that separation in rotating and non-rotating cases occurs more or less at the same chordwise location. Wood [20] performed a 3D panel analysis and suggested that the separation point moves downstream in rotation. Narramore and Vermeland [21] carried out a CFD analysis on a helicopter blade and concluded that separation in the inboard region is suppressed in rotation, i.e., the angle at which the airfoil begins to separate is much higher in rotation compared to a stationary case. Snel et al. [22], and later Lindenburg [23] through a similar analysis, proposed correction models for lift for airfoils in rotation. It was highlighted that the dominant cause of rotational augmentation is the reduction in the adverse pressure due to centrifugal pumping, without invoking its effect on the separation point location. Du and Selig [24, 25] carried out an analysis similar to [18] and also concluded that the separation point moves downstream in rotation. Shen and Sørensen [26] used CFD computations of rotating and non-rotating blades to show that the effect of rotation is a change in the pressure in the separated region and not the separation point location. Corten [27], through an order of magnitude analysis of the Navier-Stokes equations for non-inertial boundary layers, predicted that in the case of rotation the separation point moves downstream. By means of a quasi-3D Navier-Stokes model, Chaviaropoulos and Hansen [28] concluded that the dominant effect in rotational augmentation is the reduction in pressure in the separated region of the airfoil due to centrifugal pumping, and not a downstream shift in the separation point. Bak et al. [29] also based their 3D correction model on a change in the pressure distribution around the airfoil. Sicot et al. [30] conducted an experimental study on the effects of rotational and turbulence effects on stall mechanisms and concluded that although turbulence influences the location of the separation point, rotation has no significant effects on the separation point location. Dumitreschu et al. [31] called the effect "stall-delay", suggesting that Coriolis forces cause a downstream shift in the location of the separation point in rotation.

On the other hand there have been studies, some elements of which contradict the majority of published research. Savino and Nyland [32], for example, performed flow visualization experiments on a turbine and concluded that separation point moves toward the leading edge in rotation, in other words, stall is advanced and not delayed. It is worth highlighting here that this conclusion was mis-interpreted by some of the works cited herein, [24, 25] and [33]. In their literature review, these two works write that the results of [32] support stall delay.

In a more recent paper, Gross et al. propose a different explanation to rotational augmentation. The authors suggest that process of laminar to turbulent transition is expedited as a result of rotation, and this is the cause of an augmentation in lift. This

particular work was criticized by the current author and the supervisor in [34], and the main conclusions in that paper are presented in Section 4.3.2.

In sum, the variety of explanations to rotational augmentation that have been seen in literature presented above are as follows:

- A stall delay effect, where the separation point on a rotating blade compared to the same airfoil in 2D flow at the same AOA is shifted towards the trailing edge,
- a change in the pressure distribution due to the phenomenon called centrifugal pumping, whereby strong radial flow occurs in the separated region of the blade (explained in detail in Chapter 4),
- a combination of both, a stall delay effect as well as change in pressure due to centrifugal pumping, and
- laminar-turbulence transition.

The fact that such a wide spectrum of explanations still exists today in the scientific community highlights the complexity of the rotational augmentation problem. Hence, the current study is warranted.

2.3 Correction models for rotational augmentation

One of the first attempts to study and model this phenomenon was carried out in the EU project "Dynamic Stall and Three-dimensional Effects" [35]. Through an order of magnitude analysis on the incompressible boundary layer equations for rotating blades, it was found that the change in lift is primarily a function of the ratio (c/r), where c and r are the local chord and the local radius, respectively. Owing to the complexity of the rotational augmentation phenomenon, analysis using different validation methods lead to different models for correction in lift and drag forces.

Most of the models defined the factors f_l and f_d that represent the augmentation in lift and drag, respectively, and are defined as:

$$C_{L,3D}(\alpha) = C_{L,2D}(\alpha) + f_l \cdot (2\pi \sin(\alpha - \alpha_0) - C_{L,2D}(\alpha)), \tag{2.6}$$

where α_0 is the angle of attack at zero lift, and similarly for the drag as:

Model	Expression for f_l, f_d	Empirical constants
Snel et al. [22]	$f_l = a_s \cdot \left(\frac{c}{r}\right)^h$ $f_d = 0$	$a_s = 3$, $h = 2$
Du & Selig [24, 25]	$f_l = \frac{1}{2\pi}\left[\frac{1.6(c/r)}{0.1267}\frac{a_d-(c/r)^{\frac{d_d R}{\Lambda r}}}{b_d+(c/r)^{\frac{d_d R}{\Lambda r}}} - 1\right]$, $f_d = -\frac{1}{2\pi}\left[\frac{1.6(c/r)}{0.1267}\frac{a_d-(c/r)^{\frac{d_d R}{2\Lambda r}}}{b_d+(c/r)^{\frac{d_d R}{2\Lambda r}}} - 1\right]$	$\Lambda = \Omega R/\sqrt{V_\infty^2 - (\Omega R)^2}$ $a_d = d_d = b_d = 1$
Chaviaropoulos and Hansen [28]	$f_l = a_h \left(\frac{c}{r}\right)^h \cos^n\theta$ $f_d = a_h \left(\frac{c}{r}\right)^h \cos^n\theta$	$a_h = 2.2$, $h = 1$ and $n = 4$
Lindenburg [23]	$f_l = a_l \left(\frac{\Omega R}{V_{rel}}\right)^2 \left(\frac{c}{r}\right)^h$ $f_d = 0$	$a_l = 3.1$ and $h = 2$
Dumitrescu and Cardos [31, 36, 37]	$f_l = \left[1 - \exp\left(-\frac{\gamma_d}{r/c-1}\right)\right]$ $f_d = 0$	$\gamma_d = 1.25$

TABLE 2.1: The expression for the 3D corrected lift and drag coefficients as modelled by some of the existing 3D correction models.

$$C_{D,3D}(\alpha) = C_{D,2D}(\alpha) + f_d \cdot C_{D,2D}(\alpha), \tag{2.7}$$

Some models corrected for lift only, whereas others corrected for lift and drag. The different expressions for f_l and f_d from different models are shown in Table 2.1.

Bak et al. [29]

The model by Bak et al. is different than the other models, in that correction is made to the pressure distribution around the airfoil in rotation, which then has to be integrated to obtain the normal and tangential forces (and thereby the lift and drag). The correction to pressure is modelled as:

$$
\begin{aligned}
c_{p,3D} &= c_{p,2D} + \Delta c_p, \\
\Delta c_p &= amplification \times shape,
\end{aligned} \tag{2.8}
$$

where, the amplification factor and the shape factor are defined as:

$$
\begin{aligned}
amplification &= \sqrt{1 + \left(\frac{R}{r}\right)^2} \frac{2}{1 + \tan^2(\alpha + \theta)} \left(\frac{c}{r}\right), \\
shape &= \frac{5}{2} \left(1 - \frac{x}{c}\right)^2 \cdot \left(\frac{\alpha - \alpha_{f=1}}{\alpha_{f=0} - \alpha_{f=1}}\right)^2,
\end{aligned} \tag{2.9}
$$

where the *shape* factor is defined such that max(*shape*)= 2.5, α is the effective angle of attack, $\alpha_{f=0}$ is the 2D angle of attack at which the flow over the airfoil is fully separated, and $\alpha_{f=1}$ is the angle of attack for which the flow over the airfoil at the onset of separation. The correction to pressure thus becomes:

$$
\Delta c_p = 5 \left(1 - \frac{x}{c}\right)^2 \cdot \left(\frac{\alpha - \alpha_{f=1}}{\alpha_{f=0} - \alpha_{f=1}}\right)^2 \sqrt{1 + \left(\frac{R}{r}\right)^2} \frac{1}{1 + \tan^2(\alpha + \theta)} \left(\frac{c}{r}\right). \tag{2.10}
$$

Based on this correction to the c_p distribution, the 3D normal and tangential force coefficients as well as the moment coefficient (which refers to the 1/4-chord position) can be calculated as:

$$
\begin{aligned}
C_{N,3D} &= C_{N,2D} + \int_{\frac{x}{c}=LE}^{\frac{x}{c}=TE} \Delta c_p d\left(\frac{x}{c}\right), \\
C_{T,3D} &= C_{T,2D} + \int_{\frac{y}{c}=LE}^{\frac{y}{c}=TE} \Delta c_p d\left(\frac{y}{c}\right), \\
C_{M,3D} &= C_{M,2D} - \int_{\frac{x}{c}=LE}^{\frac{x}{c}=TE} \Delta c_p \left(\frac{x}{c} - 0.25\right) \cdot d\left(\frac{x}{c}\right) - \int_{\frac{y}{c}=LE}^{\frac{y}{c}=TE} \Delta c_p \left(\frac{y}{c}\right) \cdot d\left(\frac{y}{c}\right).
\end{aligned} \tag{2.11}
$$

The 3D lift and drag coefficients can be derived using the normal and tangential force coefficients and the local angle of attack. Note that in the original work [29], the numerical coefficient in the right hand side of Equation 2.10 is misprinted as $\frac{5}{2}$, but it should be 5.

More on the behaviour of the engineering models mentioned here will be discussed in Chapter 4.

2.4 Dynamic stall

Dynamic stall is the term used to refer to the complex unsteady stalling mechanism that occurs on an airfoil during a rapid change in its AOA. This stalling mechanism results in aerodynamic loads on the airfoil that are different from those in static conditions. For convenience, dynamic stall is often studied under periodic pitching conditions. Figure 2.4 shows an example case where an airfoil undergoes a sinusoidal pitching motion with a mean AOA of $\alpha_M \simeq 10^\circ$ and a pitching amplitude of $\alpha_\Omega \simeq 6^\circ$. The physical mechanism that underlies dynamic stall is complicated and has been described in various texts in detail, e.g., [13, 38–40].

According to Kelvin's circulation theorem, circulation is a conserved quantity ($\frac{D\Gamma}{Dt} = 0$, Γ being the circulation) [41]. When the AOA on an airfoil is rapidly changed, vorticity is shed due to the change in the bound circulation on the airfoil. In thin airfoils, such as those used in helicopters, vortex shedding typically occurs at the airfoil leading edge [38]. As the shed vortex convects along the chord of the airfoil, high lift is sustained on the airfoil approximately along the inviscid $C_L - \alpha$ curve. At around the highest AOA, the airfoil undergoes complete stall. The time period from stall to when the C_L returns to its steady state value is the reattachment phase, during which the airfoil experiences lift that is lower in magnitude than its steady value. At the end of the reattachment phase the lift on the airfoil returns to its corresponding value along the steady $C_L - \alpha$ curve. This difference in lift between the ascending and descending AOA phases is seen as a hysteresis loop. The extent of the hysteresis is a function of the pitching frequency, the mean AOA and the pitching amplitude, and has important aeroelastic implications.

Wind turbines use airfoils that are typically thicker than those used on helicopters. As a result, Hansen et al. [4] claim that leading edge separation is less common in wind turbines. On the other hand, some studies such as [42, 43] have shown evidence of leading edge vortex shedding on wind turbine blades. Some dynamic stall models for wind turbines such as [4, 44], neglect leading edge separation completely, whereas some others such as [45] do not. It is difficult to say whether or not neglecting leading edge separation is a more accurate representation of the physical process that occurs generally on wind turbine blades. In either case, since the models are semi-empirical, the values of the empirical constants can always be adjusted so as to match experimental observations, as done in the respective papers.

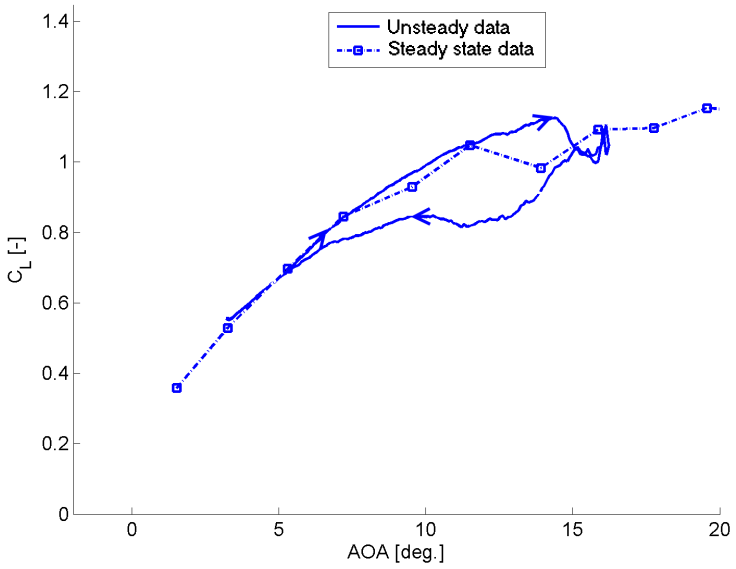

FIGURE 2.4: An example case of lift from an oscillating airfoil with a mean AOA of approximately 10°, and a pitching amplitude of approximately 6°, and a reduced pitching frequency of $K = 0.035$.

Dynamic stall was initially investigated in the 1960s during the design of some of the first high-speed helicopters. Over the half of a century since then, a large effort has been dedicated to understanding and modelling dynamic stall for various engineering applications. Accurate prediction of such periodic aerodynamic loads on helicopters has been identified as vital in assessing its lifetime. Carr [38], for example, highlighted that in many cases dynamic stall is the primary limiting factor in the performance of these structures. With increased demand for robust wind turbine design codes, dynamic stall has also gained much attention. Conditions in which real wind turbines operate include turbulent inflow, yaw misalignment, and wind shear, etc., which may give rise to dynamic stall on the blades. Several engineering methods to model this phenomenon exist, see for example [13] for a review on some existing models for helicopter rotors and [4, 44, 46] for wind turbines.

Furthermore, this phenomenon may occur in the separated regions on the inner parts of the blades giving rise to dynamic stall in rotationally augmented flows. Schreck et al. [43, 47] highlighted that dynamic stall and rotational augmentation are most pronounced in the inboard sections. Both dynamic stall and rotational augmentation received significant attention over the last few decades, but independently. The experimental studies that did look at dynamic stall on wind turbines have mostly been on wind turbines operating in yawed flow, for example [43, 48]. Most 3D augmentation models have been characterised for axial operating conditions, however dynamic stall together with rotational augmentation in axial operating condition has not been studied in detail.

The N-sequence data from the NREL Phase VI experiment [2] contains pressure data measured on the wind turbine blades. In this experiment, the rotor operated under axial conditions with the blades rotating and pitching simultaneously, and it thereby facilitates the study of dynamic stall together with rotational augmentation under axial operating conditions. Furthermore, unsteady Delayed Detached Eddy Simulations (DDES) of the same have been carried out using the in-house flow solver EllipSys3D [94–96]. These data are used for analysis in the current work, and more details on the available data campaigns will be given in the next chapter. Modelling dynamic stall has been done using the Beddoes-Leishman type dynamic stall model by Hansen et al. [4].

Dynamic stall together with rotational augmentation in yawed flow was studied in the past [48]. The challenges yawed conditions add to analysing dynamic stall together with rotational augmentation were highlighted by Schepers in [6]. Schepers highlights that in yawed flow the induction over the rotor disc is dependent upon the wake geometry, which the classical BEM does not account for. This introduces an additional complexity in a BEM-based analysis on dynamic stall, due to the lack of understanding of the yaw effects which are physically different from dynamic stall. This further warrants the study in this thesis, in which data from an experiment under axial operation and pitching conditions are analysed, thus circumventing the challenges associated with yawed flow.

2.4.1 Dynamic stall model

The scope of this part of the thesis is to investigate whether dynamic stall as it occurs on a rotating wind turbine blade is qualitatively any different from a 2D case. Ideally, a comparison between different existing dynamic stall models could make the study more comprehensive, but it is outside the scope of this thesis and is recommended for future work. In this work, one dynamic stall model by Hansen et al. [4] has been chosen and is applied to selected N sequence cases, and the results are compared with experimental data. The dynamic stall model by Hansen et al is a modification of the Beddoes-Leishman dynamic stall model [49], to suit wind turbine blades. The idea behind the original Beddoes-Leishman dynamic stall model is that the different physical effects influencing the aerodynamics of an oscillating airfoil can be grouped into four modules: the attached flow module, the leading edge separation module, the trailing edge separation module, and the vortex lift module. The original model was designed for helicopter rotors, which typically use thin blades and operate at high Mach numbers. In the implementation of Hansen et al., the following two modifications are made to the original model to suit wind turbine applications:

1. Most wind turbines use airfoils that are thicker than those typically used on helicopters, and leading edge separation is less common on thick airfoils. Hence, leading edge separation is not accounted for in this model.

2. The highest Mach numbers seen on wind turbines is only of the order 0.3 (the speed of the tip of a blade operating at a tip speed ratio of 7 at $U_\infty = 15$ m/s is 105 m/s), and so compressibility effects are ignored.

This results in a simplified dynamic stall model that outputs time series data of dynamic lift, drag and moment coefficients, for a given input of the frequency of pitching, the mean angle of attack, the amplitude of oscillation and the steady polars. The algorithm can be outlined as follows (for details, see [4, 50]):

1. The input to the dynamic stall model are the steady, aerodynamic polars. Traditionally these are 2D polars, but in the present work 3D-corrected polars obtained from H, J and N sequence datasets are used.

2. Calculate the instantaneous angle of attack at the 3/4 chord using:

$$\alpha_{3/4}(t) = \alpha_{st}(t) - \frac{2\dot{y}(t) + \dot{\alpha}(t) \cdot c}{2U_\infty} \tag{2.12}$$

   where α_{st} is geometric angle between the chord and the free stream, $\dot{y}$ is the plunge velocity, $\dot{\alpha}$ is the pitch rate about the quarter chord point, c is the airfoil chord and U_∞ is the free stream velocity.

3. Calculate the effective angle of attack at the 3/4 chord, which includes the down wash due to the shed vortices,

$$\alpha_{eff}(t) = \alpha_{3/4}(t) \cdot \phi(0) + \sum_{i=1}^{2} x_i(t) \tag{2.13}$$

   where x_i are time dependent state variables and ϕ is an indicial function, defined as

$$x_i(t) = x_i(t - \Delta t) \cdot \exp\left(\frac{2U_\infty b_i}{c}\Delta t\right) + A_i \alpha_{3/4}(t) \cdot \left(1 - \exp\left(\frac{2U_\infty b_i}{c}\Delta t\right)\right) \tag{2.14}$$

   and,

$$\phi(0) = 1 - \sum_{i=1}^{2} A_i. \tag{2.15}$$

   Here, A_i and b_i are application-specific constants.

4. Calculate the dynamic lift coefficient for potential flow as,

$$C_L^{dyn,pot}(t) = 2\pi(\alpha_{eff}(t) - \alpha_0(t)) + \frac{\pi c \cdot \dot{\alpha}(t)}{2U_\infty}. \tag{2.16}$$

5. The dynamic lift under potential flow conditions from (2.16) is lagged through a first order low-pass filter to obtain

$$C_L^{lag}(t) = C_L^{lag}(t - \Delta t) \cdot \exp\left(-\frac{2U_\infty}{c}\frac{1}{\tau_P}\Delta t\right) + C_L^{dyn,pot}(t) \cdot \left(1 - \exp\left(-\frac{2U_\infty}{c}\frac{1}{\tau_P}\Delta t\right)\right) \tag{2.17}$$

6. The separation factor f defines the fraction of airfoil chord that is separated. An intermediate separation factor is defined as

$$\begin{aligned} f^{lag}(t) &= f^{st}(\alpha^*, t), \\ \alpha^*(t) &= \frac{C_L^{lag}(t)}{\left(\frac{\partial C_{L,pot}}{\partial \alpha}\right)} + \alpha_0. \end{aligned} \tag{2.18}$$

7. A dynamic separation factor is calculated by passing the lagged separation factor through another time lag filter,

$$f^{dyn}(t) = f^{dyn}(t - \Delta t) \cdot \exp\left(-\frac{2U_\infty}{c}\frac{1}{\tau_B}\Delta t\right) + f^{lag}(t) \cdot \left(1 - \frac{2U_\infty}{c}\frac{1}{\tau_B}\Delta t\right). \tag{2.19}$$

8. The aerodynamic forces are divided into circulatory and non-circulatory forces. The circulatory effects describe the memory effect of previously shed vortices, while the non-circulatory effects are instantaneous effects that describe the acceleration of mass due to the airfoil movement. The dynamic circulatory lift coefficient is calculated as,

$$C_L^{dyn,circ}(t) = C_L^{pot}(t) \cdot f^{dyn}(t) + C_L^{fs}(t)(1 - f^{dyn}(t)). \tag{2.20}$$

9. The total dynamic lift is obtained by simply adding the lift due to non-circulatory effects to (2.20),

$$C_L^{dyn}(t) = C_L^{dyn,circ}(t) + \frac{\pi c \cdot \dot{\alpha}(t)}{2U_\infty} \tag{2.21}$$

10. Drag is defined as,

$$C_D^{dyn}(t) = C_D^{eff}(t) + C_D^{ind}(t) + C_D^{dyn}(t), \tag{2.22}$$

A_1	A_2	b_1	b_2	τ_P	τ_B
0.294	0.331	0.0664	0.3266	1.5	6

TABLE 2.2: The values of the empirical constants used in the Dynamic stall model [4].

where,

$$C_D^{eff}(t) = C^{st}_{D,\alpha_{eff}(t)},$$
$$C_D^{ind}(t) = C_L^{dyn,circ}(t) \cdot (\alpha(t) - \alpha_{eff}(t)), \tag{2.23}$$

and,

$$C_D^{dyn}(t) = (C_D^{eff}(t) - C_D^{st}(\alpha_0)) \left[\left(\frac{1 - \sqrt{f^{dyn}(t)}}{2} \right)^2 - \left(\frac{1 - \sqrt{f^{lag}(t)}}{2} \right)^2 \right]. \tag{2.24}$$

11. Finally, the coefficient of moment is defined as,

$$C_M^{dyn}(t) = C_M^{eff}(t) + C_M^{non-circ}(t), \tag{2.25}$$

where,

$$C_M^{eff}(t) = C^{st}_{M,\alpha_{eff}(t)},$$
$$C_M^{non-circ} = -\frac{\pi c \cdot \dot{\alpha}(t)}{4U_\infty}. \tag{2.26}$$

This is a time marching algorithm where the values of the parameters in Equations 2.14, 2.17 and 2.19 at the time step t depend on their values at the previous time step $(t - \Delta t)$. In the first iteration, it is assumed that values of all the unsteady parameters are their corresponding 2D values. The values of the empirical constants in the current simulations were those given in [4], shown in Table 2.2

Chapter 3

Available data campaigns and data processing methods

A large amount of data was available that was useful for carrying out the current analysis. It includes data from experiments as well as those from full rotor CFD computations. Data processing was performed where necessary to facilitate comparison, analysis and interpretation. In the following section, the available data campaigns are introduced, and in the later sections the data processing methods are described.

3.1 Experimental data

Several large scale experiments have been performed in the past to study different aspects of the aerodynamics of wind turbines. In this work, two experimental wind tunnel tests that focussed on detailed pressure measurements at different radial locations on the blades are used, namely the MEXICO experiment and the NREL Phase VI experiment, see [1, 14] and [2], respectively. These two experiments contained detailed measurements collected on experimental wind turbine rotors operating under controlled conditions in a wind tunnel. Thus, these data facilitate detailed aerodynamic analysis.

3.1.1 The MEXICO experiment

The large scale experiment called MEXICO (Model Rotor Experiments In Controlled Conditions) was conducted in the German-Dutch wind (DNW) tunnel in the Netherlands in 2006, which generated a wide variety of data on a 4.5 m diameter three bladed wind turbine (shown in Figure 3.1) under various operating conditions [1, 14].

FIGURE 3.1: A photo of the 3-bladed 4.5 m diameter MEXICO turbine in the DNW wind tunnel. Image source [1].

The MEXICO rotor blades were designed using three different airfoil series. The layout of the blade is shown in Figure 3.2, and the chord and twist distributions of the same are shown in Table 3.1. These design parameters were used in the CFD and BEM based simulations on the MEXICO rotor carried out in this thesis.

The original experiment consisted of the turbine operating at various wind speeds, two different rotational speeds of 325 and 425 rpm, various yaw angles and pitch settings. The data acquired were the pressure distribution around five different sections along the span of the blades at $r/R = \{0.25, 0.35, 0.60, 0.82, 0.92\}$, measurements of the tower bending moments from the force balance, forces at the blade root from strain gauges, and stereo PIV measurements of the flow field at different radial and axial locations. See [1, 14, 51] for further details.

In this work, only the following data were used: blade pressure data at the five radial locations at a rotational speed of 425 rpm, a fixed pitch of $-2.3°$, while the free stream velocity U_∞ varied between 7 and 30 m/s in steps of approximately 1 m/s, giving rise to a total of 24 operating cases. The Reynolds numbers varied between $\mathrm{Re} \simeq 3.9 \times 10^5$ and 5.5×10^5 at the in-board sections in these operating conditions.

Span location (r/R) [-]	Chord [m]	Twist [°]	Airfoil
0.093	0.195	0	Cylinder
0.102	0.195	0	Cylinder
0.104	0.09	0	Cylinder
0.133	0.09	0	Cylinder
0.166	0.165	8.2	Transition
0.200	0.24	16.4	DU91-W2-250
0.300	0.207	12.1	DU91-W2-250
0.400	0.178	8.3	DU91-W2-250
0.455	0.166	7.1	DU91-W2-250
0.500	0.158	6.1	Transition
0.544	0.15	5.5	RISØ
0.600	0.142	4.8	RISØ
0.655	0.134	4	RISØ
0.700	0.129	3.7	Transition
0.744	0.123	3.2	NACA64-418
0.800	0.116	2.6	NACA64-418
0.900	0.102	1.5	NACA64-418
0.962	0.092	0.7	NACA64-418
0.974	0.082	0.469	NACA64-418
0.987	0.056	0.231	NACA64-418
1.000	0.011	0	NACA64-418

TABLE 3.1: The chord and twist distribution on the MEXICO blade used in the BEM simulations of the MEXICO rotor.

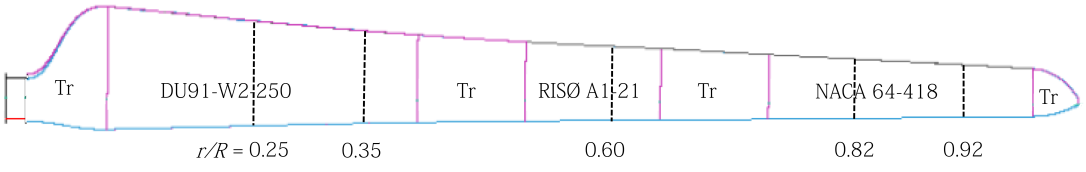

FIGURE 3.2: The blade layout on the MEXICO rotor. As shown, the blade consists of three airfoils with transitions regions in between them, labelled Tr. The vertical dotted lines denote the five locations along the blade at which pressure taps were instrumented. Image source: [1].

FIGURE 3.3: A photo of the NREL Phase VI wind turbine in the NASA Ames wind tunnel [2]. In this photo, the rotor is in its upwind configuration.

3.1.2 NREL Unsteady Aerodynamics Experiment (UAE) Phase VI

The NREL UAE Phase VI experiment was conducted in the NASA-Ames wind tunnel in 2000 [2]. This experiment consisted of a 10 m diameter 2-bladed rotor shown in Figure 3.3. This rotor was instrumented with pressure taps along the chord at five radial locations, $r/R = \{0.30, 0.47, 0.63, 0.80, 0.95\}$. A notable difference between the MEXICO rotor and the UAE Phase VI rotor is that the latter is 2-bladed and its blades are based on one airfoil geometry (the S809, as shown in Figure 3.4), while the former was a 3-bladed rotor and its blades consist of three different airfoil families.

The UAE Phase VI rotor operated at various configurations, like upwind and downwind orientations, rotating and parked conditions, at different yaw angles, different free stream wind speeds, pitching and fixed pitch while rotating, and pitching and fixed pitch at parked conditions. Data acquired at the various resulting operating conditions were arranged into data sequences, see [2] for details. In this work, data from the following sequences has been studied:

1. Rotating and fixed pitch condition (H and J sequences). Axial operation, varying U_∞, 72 rpm, and fixed tip pitch angles of 6° (H sequence) and 6° (J sequence). Here, positive pitch is towards a decreasing angle of attack. The angle of attack on the blade was derived using the inverse BEM method [52].

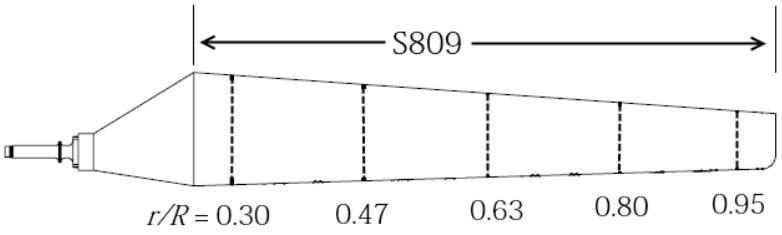

FIGURE 3.4: The layout of the blades on the NREL Phase VI rotor [2]. The dotted lines represent the span wise locations of the instrumented pressure taps.

2. Rotating and pitching condition (N sequence). Axial operation at $U_\infty = 15$ m/s and 72 rpm, while the blade pitches continuously at various values of the reduced frequency (K), mean pitch angle (β_M) and the pitch amplitude (β_Ω). Here, the reduced frequency is defined as

$$K = \frac{\Omega c}{2U_{local}}, \tag{3.1}$$

where, Ω is the pitching frequency, U_{local} is the local relative velocity, and c is the length of the local chord. The specific N sequence cases investigated in this work are shown in Table 5.1. The angle of attack on the blade was derived using the inverse BEM method described in the next section.

3. Parked condition (L sequence). The rotor is parked and the instrumented blade was incremented slowly in pitch. Pressure distribution at various radial locations was collected for various pitch angles, resulting in a C_L and C_D vs. AOA. This data is different from a typically used wind tunnel data in that it includes the induction due to the trailing vortices on the blade. The angle of attack is the angle between the local chord and the free stream wind direction.

4. Parked pitching condition (O sequence). The rotor is parked, but the blade pitches at various values of K, β_Ω and β_M values. The angle of attack is the instantaneous angle between the local chord and the free stream wind direction.

The local Reynolds number at the locations $r/R = 0.30$ and 0.47, at $U_\infty = 15$ m/s and $\omega = 7.53$ rad/s (72 rpm) are Re $\simeq 8.9 \times 10^5$ and 9.6×10^5, respectively. The 2D lift and drag polars used in the BEM simulations are the CSU wind tunnel data obtained at Re $= 7.5 \times 10^5$, from [2]. Table 3.2 shows shows the chord and twist distribution of the same rotor, also used in the BEM simulations.

Span location (r/R) [-]	Chord [m]	Twist [°]
0.131	0.218	0
0.176	0.183	0
0.2	0.349	6.7
0.212	0.441	9.9
0.225	0.544	13.4
0.25	0.737	20.04
0.267	0.728	18.074
0.3	0.711	14.292
0.328	0.697	11.909
0.388	0.666	7.979
0.449	0.636	5.308
0.466	0.627	4.715
0.509	0.605	3.425
0.57	0.574	2.083
0.631	0.543	1.15
0.633	0.542	1.115
0.691	0.512	0.494
0.752	0.482	-0.015
0.8	0.457	-0.381
0.812	0.451	-0.475
0.873	0.42	-0.92
0.934	0.389	-1.352
0.95	0.381	-1.469
0.994	0.358	-1.775

TABLE 3.2: The chord and twist distribution on the NREL Phase VI blade used in the BEM simulations.

3.2 CFD simulations

Several computations were carried out on the models of both experimental rotors described above, to match some of the available experimental configurations. The simulations carried out on the MEXICO turbine model were primarily steady-state Reynolds-Averaged Navier-Stokes (RANS) computations, while those on the NREL Phase VI rotor were unsteady Delayed Detached Eddy Simulations (DDES).

The in-house flow solver EllipSys3D was used in all computations in this thesis. The code was developed in co-operation between the Department of Mechanical Engineering at the Technical University of Denmark and the former Department of Wind Energy at Risø National Laboratory, Risø-DTU, see [94, 95] and [96]. It is a multiblock finite-volume discretization of the incompressible Navier-Stokes equations, where the pressure/velocity coupling is ensured using the SIMPLE algorithm. The convective terms are discretized using the third-order QUICK upwind scheme, and turbulence is modelled by the $k-\omega$ Sheer Stress Transport (SST) eddy viscosity model. The EllipSys3D code is second order accurate in time, using a second order backward differencing time discretization and sub-iteration within each time step.

The rotational motion was simulated by a moving mesh method, where the grid points in the computational mesh are all moved together as a solid body using a deforming mesh (DM) formulation in a fixed frame of reference. To assure that no artificial mass sources are generated by the mesh deformation, the mesh velocities needed for the convective terms were computed enforcing the space conservation law, as described by [102].

In the unsteady simulations, turbulence was modelled by the k-ω SST eddy viscosity model [97] in the form of the Delayed Detached Eddy Simulation (DDES) technique of Menter and Kuntz [98], which is an extension of the DES model as proposed by Strelets [99]. The DDES methodology is combined with laminar/turbulent transition in the boundary layer on the blade which is modelled with the $\gamma - \widetilde{\mathrm{Re}}_\theta$ correlation based transition model of Menter [100]−for the present implementation see [53]. As the DDES methodology treats every thing except the separated region using the RANS methodology, the transition model can be applied in the standard way within the boundary layer.

The diffusive terms are discretized with a second order central differencing scheme. The convective fluxes were computed using the QUICK scheme in the RANS regions while a fourth order central scheme was used for the regions where the DDES model has switched to Large Eddy Simulation (LES) technique. The simulations were computed as transient runs with approximately 1700 time-steps per revolution, and using 12 sub-iterations in each time-step. The turbulence intensity at the rotor location was controlled by the

specified inflow values of the turbulent kinetic energy 'k' and the specific turbulence dissipation rate ω, along with the decay of the turbulence from the inlet to the rotor location. The decay of the turbulence from the inlet to the rotor location can be computed from the free stream velocity and the distance from the inflow boundary to the rotor location, see Langtry et al. [103].

3.2.1 Computations of the MEXICO rotor

Previously, steady state RANS computations were carried out on the MEXICO rotor for a limited number of cases at axial operating conditions which are described in [54]. In the present work, the data from [54] as well as new computations carried out at several additional free stream velocities at the same pitch and rpm values are presented. The new computations were carried out in order to generate a wider range of angles of attack seen by the blades. All in all, full rotor computations were performed at $U_\infty = \{10, 12, 15, 17, 21, 24, 28\}$ m/s.

In addition, a new set of computations of a re-twisted MEXICO rotor have also been carried out. The only difference between the rotor configuration in the previous set of computations and the new ones is the new blade twist distribution, which is shown in Figure 3.5 as $T1$ and $T2$. These new computations were carried out at $U_\infty = \{10, 12, 15, 17, 20, 25\}$ m/s. The purpose of these new computations was to investigate the effect of twist on the 3D airfoil coefficients, which will be further discussed in detail in Chapter 4.

3.2.2 2D CFD computations

A set of 2D CFD computations were also carried out on the three airfoil geometries used in the MEXICO blades for a range of angles of attack, starting from $\alpha = 0°$ to $30°$ in steps of $1°$. The Reynolds numbers at $r/R = 0.25$ and 0.35 on the MEXICO turbine operating at $U_\infty = 15$ m/s and at $\omega = 44.5$ rad/s (425 rpm) computed as $\mathrm{Re} = \frac{c \cdot \sqrt{U_\infty^2 + (r\omega)^2}}{\nu}$ are approximately $\mathrm{Re} = 4.15 \times 10^5$ and $\mathrm{Re} = 4.95 \times 10^5$, respectively. The 2D CFD computations were carried out at $\mathrm{Re} = 4 \times 10^5$, so that they could be compared with 3D cases at fairly similar Reynolds numbers.

3.2.3 Computations of the NREL Phase VI rotor

A unique feature of the NREL Phase VI experiment relative to the current study is its N-sequence data, in which the rotor undergoes simultaneous pitching and rotating

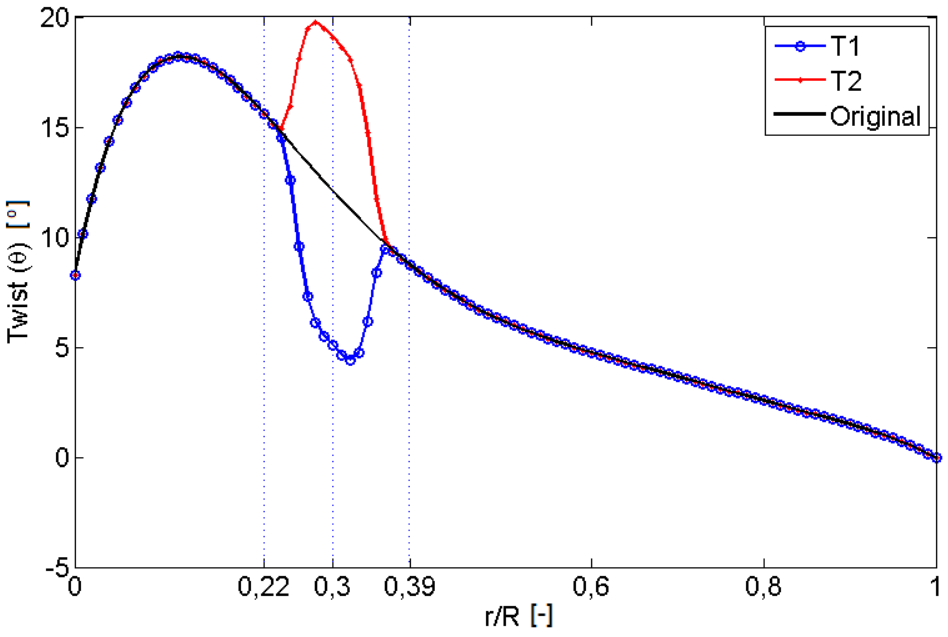

FIGURE 3.5: Modified twist distributions of the rotor, $T1$ and $T2$.

Case Nr.	K	α_M	α_Ω
N47020	0.063	1.96	2.37
N47090	0.100	8.18	2.37
N47350	0.100	13.50	6.33

TABLE 3.3: The N sequence cases that were selected for carrying out CFD simulations. The reduced frequencies are computed as defined in Equation 3.1. The K values and the mean AOA correspond to the radial location at $r/R = 0.47$.

operation. Unsteady full rotor DDES CFD computations were performed for select N sequence cases, shown in Table 3.3.

3.3 Data processing

In this thesis, the aim is to compare the lift, drag and moment coefficients at various effective angles of attack among the experimental data, between the experimental and CFD data, and finally between the experimental data and the estimated values from the engineering models described in Chapter 2. The coefficients of lift, drag and moment, for experimental data were obtained by simply integrating the pressure distributions at various sections. Computing the effective angle of attack is a challenge and different

methods of doing this were presented previously in [52]. The main conclusions from this work are outlined in the next section.

3.3.1 Inverse BEM method

Several techniques exist by which the effective AOA can be estimated for a given rotor. The following methods were considered in determining the effective AOA in the current analysis.

1. The inverse BEM method [55, 56], which uses the pre-determined local forces to calculate the local induction.
2. Using CFD data to obtain the annular average of the axial velocity (and thereby the induction $\overline{a}$) at a given radial position in the rotor plane [9, 57, 58].
3. Using CFD data to obtain the the axial velocity at a given radial position in the rotor plane at the location of the blade (a_B). This method is similar to method (2.).
4. Determination of AOA by comparison of high-pressure-side c_p distributions of a 3D case with a 2D case with a known AOA [59].

The analysis presented in this thesis involves a comparison between the CFD, engineering models, and experimental data. Method (4.) was found to be unsuitable for the current analysis in [52], and the methods (2.) and (3.) require detailed knowledge of the flow field which were not available for the experimental data. Eliminating methods (2.) through (4.), left method (1.). In order to maintain consistency in the determination the effective AOA between the CFD data, the experimental data, and the engineering models, a method involving the BEM is seemingly the most suitable for the current analysis. Further, the rotational augmentation models are designed to be used in BEM-based codes. Hence, the inverse BEM method was chosen for the analysis throughout this thesis.

The inverse BEM method is described previously in several works, for example [55, 56, 60]. It utilizes the pre-determined normal (F_N) and tangential (F_T) forces on the blades, obtained from either experiments or CFD computations, to calculate the local induction. Once the local induction is known, the local effective AOAs and the 3D lift and drag polars can be determined. As an algorithm, it can be summarized as follows:

1. Initialize the axial (a) and the tangential (a') induction factors, typically $a = a' = 0$.

2. Compute the effective inflow angle ϕ as

$$\phi = \tan^{-1}\left[\frac{(1-a)V_o}{(1+a')r\omega}\right] \tag{3.2}$$

3. Obtain sectional CN and CT values−in this work, data from full rotor CFD computations of the MEXICO rotor are used.

4. Calculate new values of a and a',

$$a_{new} = \frac{1}{\frac{8\pi r F \sin^2\phi}{cBCN} + 1}, \tag{3.3}$$

and,

$$a'_{new} = \frac{1}{\frac{8\pi r F \sin\phi\cos\phi}{cBCT} - 1}. \tag{3.4}$$

5. If the difference between the new vales of [a, a'] and [a_{new}, a'_{new}] is more than a certain tolerance, go to step 2. Else, continue.

6. Compute C_L and C_D as,

$$\begin{aligned} C_{L,3D} &= CN\cos\phi + CT\sin\phi, \\ C_{D,3D} &= CN\sin\phi - CT\cos\phi. \end{aligned} \tag{3.5}$$

These values are the new, 3D, lift and drag coefficients.

3.3.2 Inverse BEM on unsteady data

Estimating the effective angle of attack in unsteady conditions is a challenge. Gardner and Richter [61] highlight that measuring the aerodynamic angle of attack is sometimes the largest hurdle in analysing experimental data. In this work, the following methodology is adopted for estimating the effective angle of attack for the UAE Phase VI N sequence experimental data. The first step is to make the following assumption (say *hypothesis 1*): Since induction at the rotor is a far field effect determined by the wake generated from several rotor rotations, the influence of one blade pitching cycle is negligible compared to the aggregate influence of the wake produced by several blade pitch cycles during multiple rotor rotations. In other words, the mean thrust on the flow field by rotor blades pitching as $\beta(t) = \beta_M + \beta_\Omega \cos\Omega t$ over a time period of $\left(\frac{2\pi}{\Omega}\right)$ is approximately the same as a rotor operating in steady state at a constant blade pitch angle β_M under similar conditions. By this hypothesis, the normal force coefficients from the N sequence are averaged over one pitch cycle and these mean forces are used as the input

to the inverse BEM code. Upon obtaining a static effective AOA (α_{eff}) by this method, the dynamic effective AOA ($\alpha_{dyn}(t)$) is assumed to be simply,

$$\alpha_{dyn}(t) = \alpha_{eff} + \beta(t). \tag{3.6}$$

The reliability of the inverse BEM method for steady conditions has already been validated to some extent in [52]. *Hypothesis 1*, concerning unsteady conditions, was validated using the H sequence (zero yaw only) experimental series of the UAE Phase VI following the methodology documented below in connection with Tables 3.4 and 3.5. If *hypothesis 1* is valid, then the force coefficients at different radial locations in the N sequence whose mean tip pitch is also 3° must be the same as those from the H sequence, as shown below.

Table 3.4 shows the experimental configuration of the four sets of data that are used in the comparison presented in Table 3.5. In Table 3.4, the H sequence condition in columns one through four consist of mean blade tip pitch angles (β_Ω) of 2.95°, 2.95° and 3.13°. The local K is computed as defined in Equation 3.1.

In Table 3.5, the C_N values at the five span wise locations for three experimental cases from the N sequence are compared to those from the H sequence. All in all, there are 15 comparisons that can be made in this table. For each C_N value, the percentage differences between N sequence C_N values and the corresponding H sequence C_N value are shown in the parentheses. As can be seen, the percentage difference between the H sequence and the N sequence data is less than 6% in 11 out of the 15 cases. There are four cases where the percentage difference is higher, up to 26%, which occur at the 47% and the 80% sections on the series N80220 and N80250.

It has been shown in [53] that stall cells occur in the vicinity of the 47% section in some cases on the UAE phase VI blade. It is a possibility that similar structures are created near the 47% and the 80% sections in the cases examined here, and these structures are responsible for the deviation seen in the four later cases. Also, note that the first two experimental cases (N80220 and N80250) have a higher pitching amplitude β_Ω compared to the third case (N95090) where there is the best agreement between the averaged N sequence forces and those from the H sequence. This indicates that *hypothesis 1* works best for low values of β_Ω. Therefore, a second possibility could be that *hypothesis 1* starts to introduce errors at high values of β_Ω. Further, a third possibility could also be that the lift overshoot beyond static $C_{L,max}$ that is characteristic of classical dynamic stall is most prominent in these four cases being discussed.

	H-seq.	*N80220*	*N80250*	*N95090*
Tip pitch	3°	2.95°	2.95°	3.13°
β_Ω	-	10.26°	5.79°	2°
Local K	-	0.025	0.05	0.025

TABLE 3.4: The parameters β_Ω, K and the tip pitch for each of the cases considered in table (3.5). Here, the K value corresponds to the section $r/R = 0.80$ for the cases N80220 and N80250, and $r/R = 0.95$ for the case N95090.

	H-seq.	*N80220*	*N80250*	*N95090*
r/R	C_N	C_N (ϵ)	C_N (ϵ)	C_N (ϵ)
0.30	2.33	2.19 *(4.1)*	2.21 *(5.2)*	2.28 *(4.1)*
0.47	1.16	1.36 *(-17)*	1.27 *(-9.1)*	1.14 *(2)*
0.63	1.30	1.27 *(2.4)*	1.25 *(4.2)*	1.28 *(1.8)*
0.80	0.84	1.06 *(-25.7)*	1.07 *(-26.4)*	0.89 *(-5.7)*
0.95	0.84	0.79 *(6.1)*	0.81 *(3.5)*	0.85 *(-1.2)*

TABLE 3.5: Table showing the mean normal force coefficient C_N (measured perpendicular to the airfoil chord) for selected cases of the N and H sequences. The values in the parenthesis are the percentage differences between the N sequence value and the corresponding H sequence value, defined as $\epsilon = \frac{C_{N,Hseq} - C_{N,Nseq}}{C_{N,Hseq}} \times 100$.

In either case, since a good agreement is seen in the majority of the cases shown in table (3.5), *hypothesis 1* is deemed reasonable for carrying out the current analysis.

Chapter 4

Results and Discussion: Rotational Augmentation

This chapter presents the results from investigations on the steady state behaviour of aerodynamic forces on the inboard parts of the blade. This chapter is divided into two parts: a study of the existing engineering models, and a study of the underlying physics. As the first part of the study, the 2D polars of the airfoils used on the MEXICO rotor and the NREL Phase VI rotor are 3D-corrected using the rotational augmentation models described in the Chapter 2. The corrected lift and drag polars were plotted along with the polars extracted from the experimental and CFD data to be able to compare and analyse behavioural trends in the models, on the inner half of the rotor. In the second part, the surface flow patterns, the pressure, and skin friction data at the inboard sections of the MEXICO rotor from the full rotor CFD computations were analysed and compared with the same parameters obtained from 2D computations.

4.1 Engineering models

Figures 4.1 to 4.3 show the lift and drag polars obtained by 3D correction, the experimental data and the CFD data for the MEXICO rotor in axial operation, a fixed rotational speed of 425 rpm, and varying wind speeds of $U_\infty = \{10, 12, 15, 17, 21, 24, 28\}$ m/s. Figures 4.4 to 4.6 show the lift and drag polars obtained by 3D correction as well as the experimental data from the J sequence of the NREL Phase VI rotor in axial operation, a fixed rotational speed of 72 rpm and various wind speeds between 5 m/s and 30 m/s. The AOAs for all experimental and CFD data shown here were estimated using an inverse-BEM method described in Section 3.3.1.

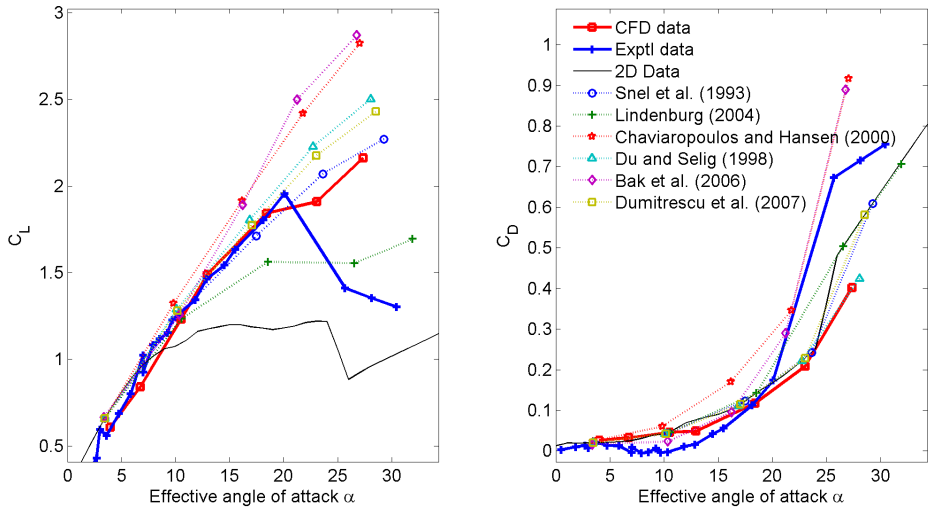

FIGURE 4.1: Lift and drag polars obtained using experimental data, CFD data and predicted polars from various rotational augmentation models on the MEXICO rotor at $r/R = 0.25$. The 2D polars shown are wind tunnel measurements at Reynolds number Re$= 5 \times 10^5$ from [3].

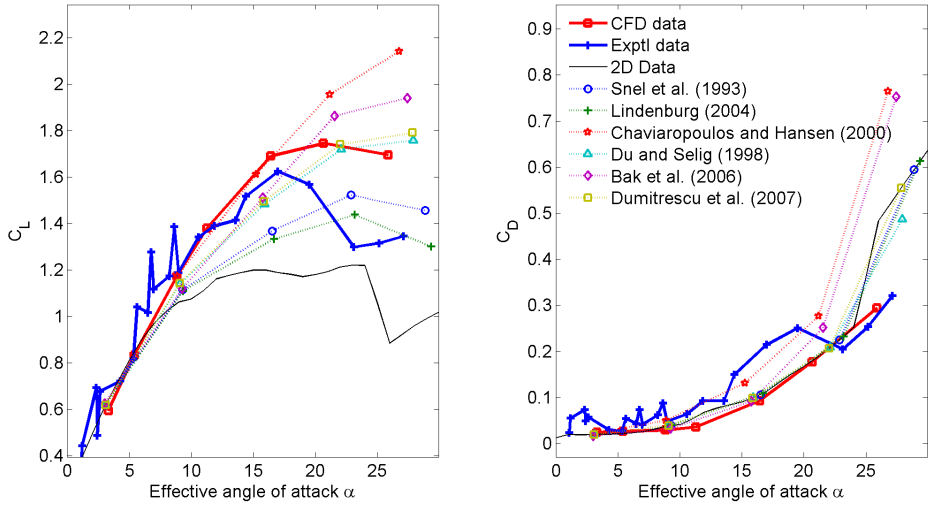

FIGURE 4.2: Lift and drag polars obtained using experimental data, CFD data and predicted polars from various rotational augmentation models on the MEXICO rotor at $r/R = 0.35$. The 2D polars shown are wind tunnel measurements at Reynolds number Re$= 5 \times 10^5$ from [3].

4.1.1 Comments on the MEXICO data

It is worthwhile to note here the following two issues with the MEXICO database relative to the pressure data obtained at the inboard sections. It has been documented previously in [51] and [14] that some of the pressure sensors at the $r/R = 0.25$ and 0.35 sections have been found to "malfunction intermittently". In [51], it was shown in an example case that for three different experimental runs under the exact same operating conditions,

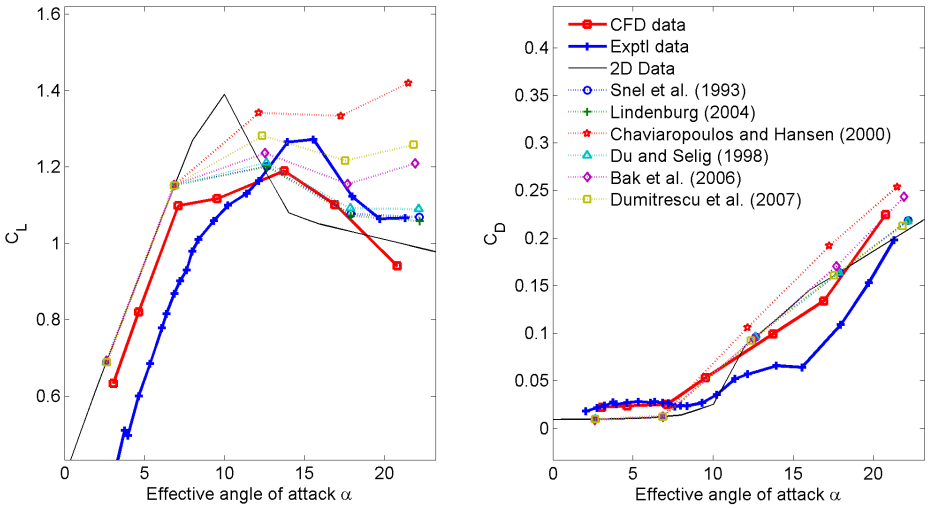

FIGURE 4.3: Lift and drag polars obtained using experimental data, CFD data and predicted polars from various rotational augmentation models on the MEXICO rotor at $r/R = 0.60$. The 2D polars shown are wind tunnel measurements at Reynolds number Re$= 1.6 \times 10^6$ from [3].

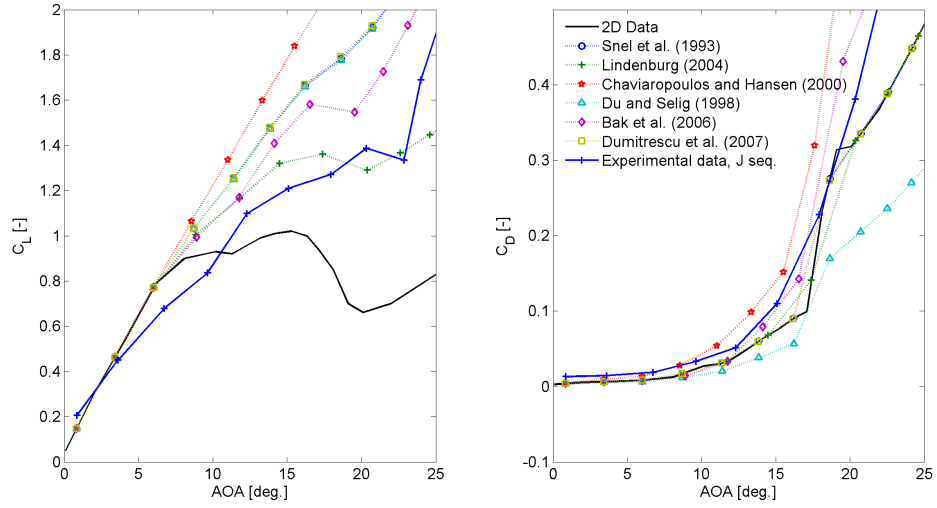

FIGURE 4.4: Lift and drag polars obtained using experimental data, CFD data and predicted polars from various rotational augmentation models on the NREL Phase VI rotor at $r/R = 0.30$. The 2D data shown is the CSU wind tunnel data at Re=7.5E5 from [2].

some of the pressure sensors at the section $r/R = 0.35$ did not reproduce the same values. This could be the explanation for the unusual peaks seen in the $C_L - \alpha$ curve in region $\alpha < 10°$ in Figure 4.2. As the reliability of the MEXICO data relative to the current analysis is hence challenged, data from the full rotor CFD computations (that are not subject to experimental uncertainty) are also included in the graphs with the MEXICO data.

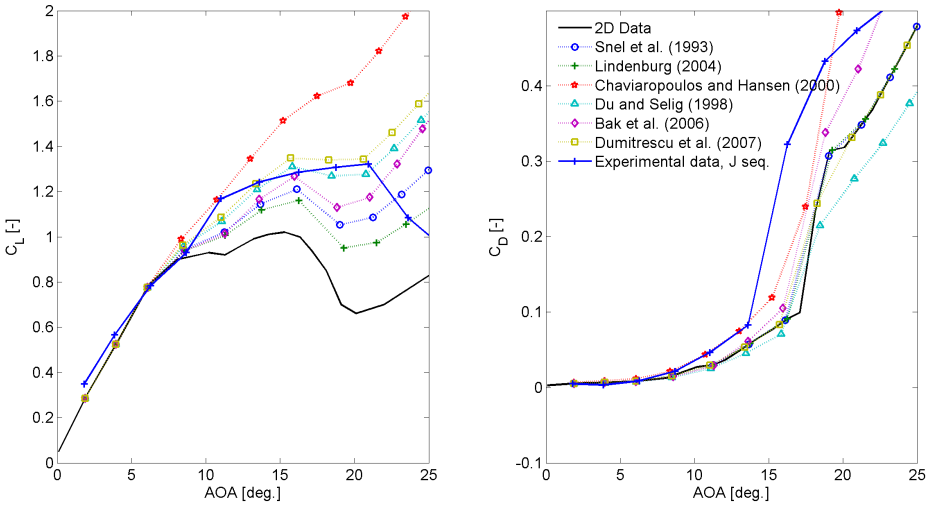

FIGURE 4.5: Lift and drag polars obtained using experimental data, CFD data and predicted polars from various rotational augmentation models on the NREL Phase VI rotor at $r/R = 0.47$. The 2D data shown is the CSU wind tunnel data at Re=7.5E5 from [2].

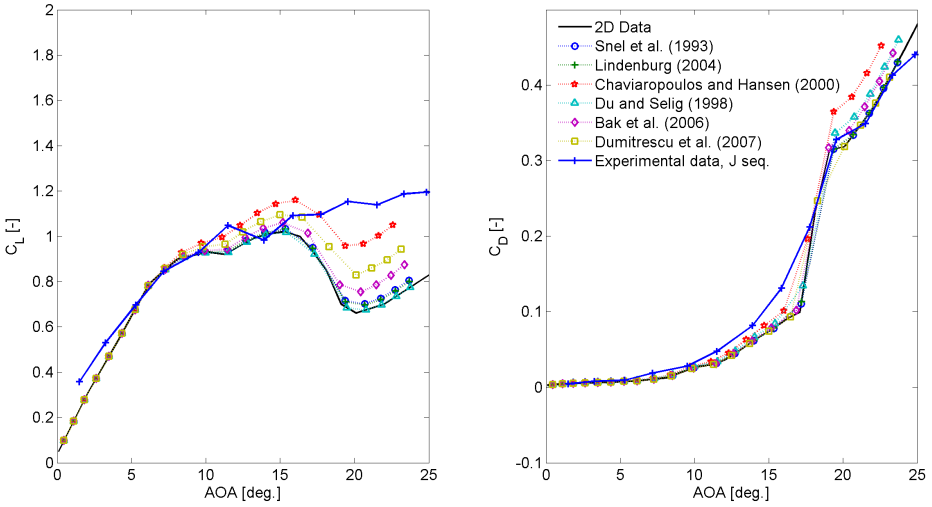

FIGURE 4.6: Lift and drag polars obtained using experimental data, CFD data and predicted polars from various rotational augmentation models on the NREL Phase VI rotor at $r/R = 0.63$. The 2D data shown is the CSU wind tunnel data at Re=7.5E5 from [2].

Secondly, consider Figure 4.7 which shows the span-wise variation of the local lift coefficient at different free stream wind speeds. As visible, there is significant variation in the local C_L along the span, especially in the region $0.6 < r/R < 0.76$. As explained later in Section 4.2, a span-wise variation in the loading has an effect on the lift polars estimated from experimental/CFD data, such that the estimated lift is different from its 2D value. This effect can be observed in Figure 4.3, where the 3D lift at the section

$r/R = 0.60$ for a given AOA is lower than its 2D value in the region $\alpha < 10°$. It must be kept in mind that this effect is present when analysing the section $r/R = 0.60$.

4.1.2 Behaviour of existing models

For the different radial sections and rotors analysed here, the relative differences between the data from the 3D correction models are generally consistent. That is, they fall in the same order when sorted according to the amount of 3D correction on lift that they model on the two rotors at the different radial locations. The following are some observations on the different models studied, sorted in the order of increasing 3D lift correction.

Lindenburg [23]. It can clearly be seen that this model consistently models lift that is lower than the rest of the models. The C_L estimated by this model is lower than the experimental/CFD data in mosst cases. Further, no correction to drag is made in this model.

Snel et al. [22]. This was one of the first engineering models for 3D correction. It is a good first approximation to 3D lift, as it compares better with the experimental or CFD data than the Lindenburg model, especially at the most inboard sections shown in Figures 4.1 and 4.4. However, at higher r/R values this model also under predicts lift (see Figures 4.2, 4.5 and 4.6), and moreover does not correct for drag.

Du and Selig [24, 25]. The lift coefficients corrected using this model agree well with the CFD/experimental data in most cases, relative to the other models. On the other hand, this model assumes that drag decreases in rotation whereas Figures 4.1 to 4.6 show either no significant change in drag (CFD data from Figures 4.1, 4.2), or an increase in drag (experimental data from Figures 4.1, 4.4, 4.5) in rotation. Note that Figure 4.3 shows that the drag from the experimental data is in fact lower compared to the 2D data at $\alpha > 10°$, however as explained in Section 4.2, this is probably not a rotational augmentation effect but rather an effect of trailed vorticity.

Dumitrescu et al. [31, 36, 37]. The behaviour of this model is quite similar to the previous Du and Selig model, in that the corrected lift coefficients compare relatively well with the CFD data for the MEXICO rotor and very well with NREL experimental data. This model also does not correct for drag.

Bak et al. [29]. It seems as though this model over-predicts lift in the most inboard of the sections shown here, $r/R = 0.25$ in case of the MEXICO rotor (Figure 4.1) and $r/R = 0.30$ in case of the NREL rotor (Figure 4.4). The observations from Section 4.2 on the lift coefficients close to the root regions suggest that corrections to the data due to the root vortex may bring the $C_L - \alpha$ curve given by this model (as well as the other models that also over-predict lift at this section) closer to the experimental/CFD data. At the sections further outboard, below $\alpha \simeq 17°$ the model also agrees well with the CFD/experimental data. Further, this is the only model studied here apart from Chaviaropoulos and Hansen [28] that models an increase in drag. The 3D corrected drag from models by Bak et al. as well as Chaviaropoulos and Hansen show similar behaviour at the very inboard sections in Figures 4.1 and 4.4. The model by Bak et al. however has slightly better agreement with the CFD MEXICO data and experimental NREL data at higher r/R regions as seen in Figures 4.3 and 4.6.

Chaviaropoulos and Hansen [28]. This model corrects for both lift and drag in rotation, but consistently over-predicts both lift and drag in the cases studied here in.

In summary, the models by Du and Selig [24, 25], Dumitrescu et al. [31, 36, 37], and Bak et al. [29], give the most reliable results for the lift, and the model by Bak et al. is the only model that effectively considers drag. Furthermore, Bak's model 3D-corrects the coefficient of moment C_M, rendering it usable with dynamic stall models (discussed in Chapter 6).

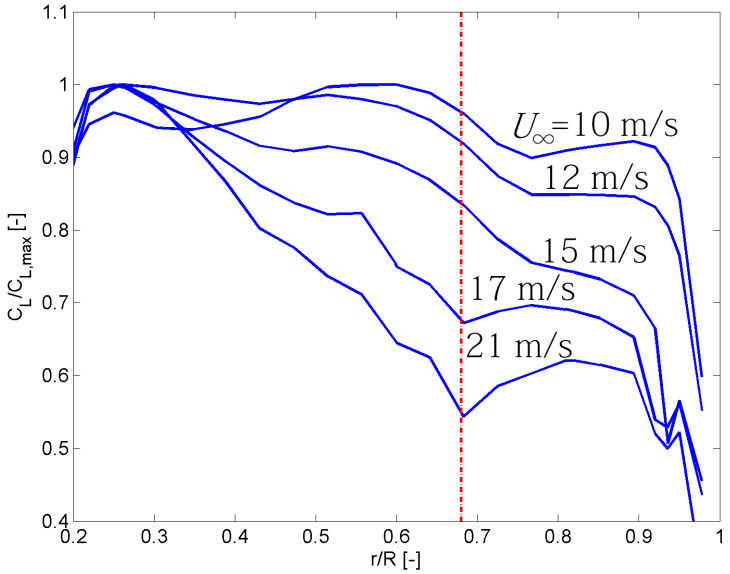

FIGURE 4.7: The variation of C_L along the MEXICO blade is shown at several free stream velocities. Here, the lift coefficient shown on the y-axis is normalized with respect to the maximum lift on the blade at a given wind speed as $\frac{C_L}{C_{L,max}}$ for convenience.

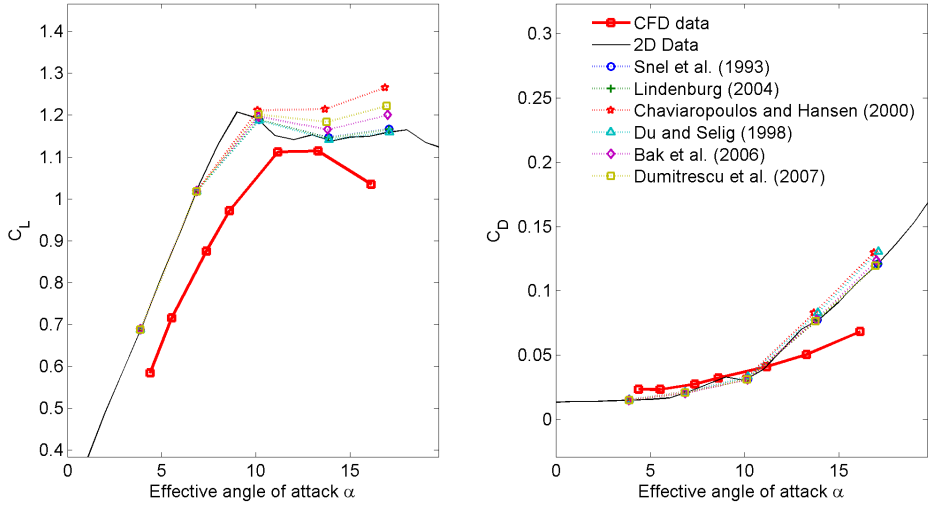

FIGURE 4.8: Lift and drag polars obtained using CFD data and predicted polars from various rotational augmentation models on the MEXICO rotor at $r/R = 0.90$.

4.2 Effect of trailed vorticity

According to Kelvin's circulation theorem, circulation is a conserved quantity ($\frac{D\Gamma}{Dt} = 0$, Γ being the circulation) [41]. That is, whenever there is a change in the bound circulation (or lift) along the blade span some vorticity is trailed, the magnitude of which is equal to the change in the bound circulation. A tip vortex is therefore nothing but the total bound vorticity on the blade that is trailed where the blade terminates.

Figure 4.8 shows $C_L - \alpha$ curve from CFD data as well as 2D data in the tip region, at $r/R = 0.90$. Note that lift computed from the 3D CFD data is lower than that from the 2D curve for a given angle of attack. This is an effect of the tip vortex, and is commonly observed to be stronger closer to the blade tip. Computing and correcting for tip losses is a very complicated problem and has been investigated over several decades, see for example [10, 11]. In this section, the lift from the 2D data is compared with the lift obtained using inverse BEM on CFD/experimental force data. The difference between the 2D and the 3D lift coefficients is what is being referred to as the effect of the trailed vorticity.

As most rotors are designed such that there are no abrupt changes in the loading along the blade in rated operating conditions, one does not expect to see any trailed vorticity at a mid board section. Interestingly in case of the MEXICO rotor, this effect can be observed at $r/R = 0.60$ by comparing the 2D data and the 3D data (from experiment as well as CFD) in Figure 4.3. By examining the lift distribution along the blade shown in Figure 4.7, it is can be seen that there is a steep change in lift between $0.6 < r/R < 0.76$, which seems more prominent at higher wind speeds. In accordance with the Kelvin's

circulation theorem, vorticity must be trailed in that region $0.6 < r/R < 0.76$, causing the experimental/CFD lift data to be lower than 2D lift in the region $\alpha < 7°$, as shown in Figure 4.7.

From Figure 4.3 it can also be observed that in the region $\alpha < 7°$ the lift computed using CFD data is greater than the lift from the experimental data for a given angle of attack. Since the rotor geometry in both the experiment as well as the CFD model are the same, this observation raises the question whether this difference is an uncertainty associated with the experiment, or a grid related issue that limits the CFD solver's ability to accurately model the trailed vorticity in the mid-board region. In either case, both the CFD and experimental data show that in this region the computed 3D lift for a given AOA is lower than the 2D data for $\alpha < 7°$.

Consider the drag polars in Figures 4.8 and 4.12 (see case $T1$ in Figure 4.12). At high AOAs (approximately $\alpha > 12°$) the drag computed from experiments/CFD data is lower compared to the 2D data, and at lower AOAs (approximately $\alpha < 12°$), the experiments/CFD drag data is higher than the 2D data. Trailed vorticity seems to have only a minor effect on drag coefficient, but this effect seems to be small.

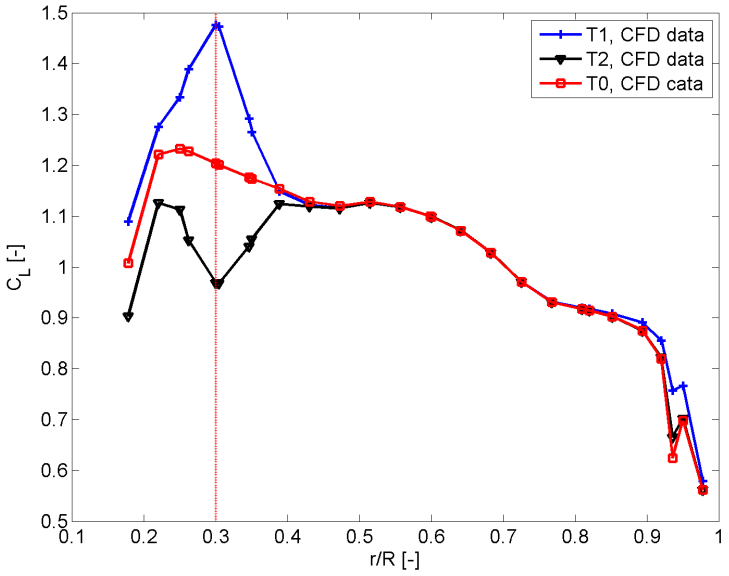

FIGURE 4.9: An example of the lift distribution along the blade from the CFD computations on the original as well as the re-twisted MEXICO blade at $U_\infty = 15$ m/s. The vertical line at $r/R = 0.30$ highlights the location at which the lift and drag polars were computed and presented in Figure 4.10.

As described in Chapter 3, abrupt changes in the twist distribution along the MEXICO blade shown in Figure 3.5 were intentionally introduced for analysis. Full rotor computations of the re-twisted MEXICO rotors $T1$ and $T2$ were carried out, and the section $r/R = 0.30$, which is approximately in the middle of the re-twisted region, was

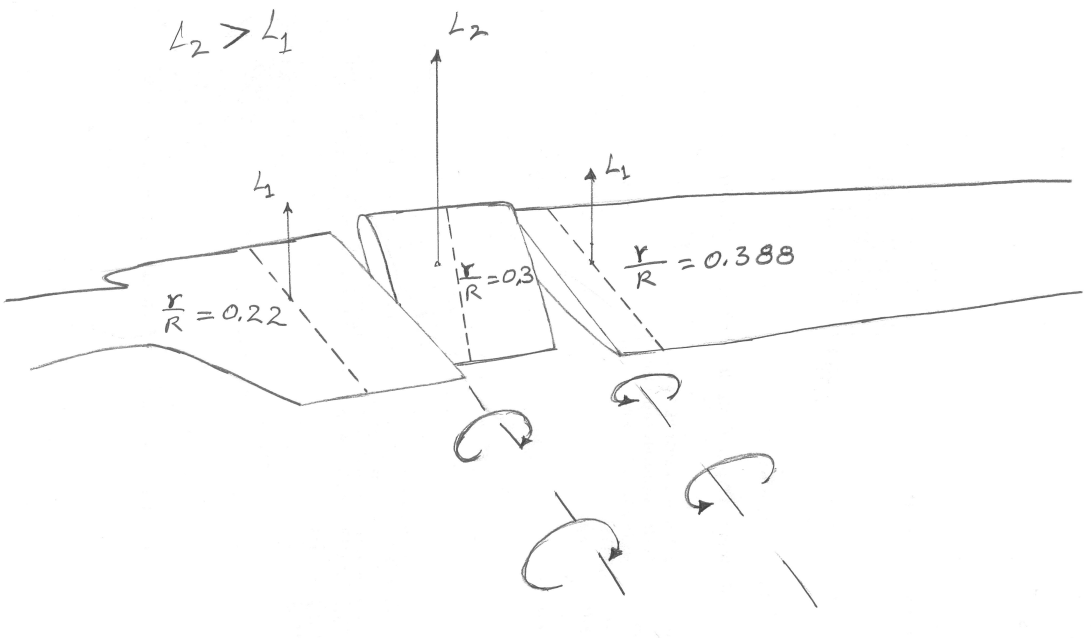

FIGURE 4.10: Schematic showing the vortices trailed on a wind turbine blade with a twist distribution $T1$ from Figure 3.5.

considered for analysis. Figure 4.9 shows the lift distributions along the blade in the cases $T1$ and $T2$ along with the original blade. In the case $T1$, the section at $r/R = 0.30$ experiences a higher lift compared its neighbouring sections. Similarly, in the case $T2$, the section at $r/R = 0.30$ experiences a lower lift compared its neighbouring sections. As a result, vorticity is trailed on either sides of the location $r/R = 0.30$ as schematically shown in the Figures 4.10 and 4.11. Note that the vortices trailed from these two radial locations have an opposite orientation. The effect of these vortices was analysed by carrying out a similar analysis on the $C_L - \alpha$ behaviour as done previously on the original rotor. By considering the orientation of the trailing vortex in the case $T1$ (Figure 4.10), one would expect that the induction due to the trailing vortices at $r/R = 0.3$ in this case would be similar to that experienced by the section $r/R = 0.9$ from Figure 4.8 due to the tip vortex, i.e., an offset to lower lift. As shown by the curve $T1$ in Figure 4.12, it is evident that this is indeed the case. Furthermore, the case $T2$ has (almost exactly) the opposite effect on lift, i.e., for a given AOA the 3D lift is higher than the 2D lift.

One possibility is that the trailing vortex causes induction in such a way that the local relative velocity seen by the two cases $T1$ and $T2$ are different, and this is somehow not captured properly by the methods were used to estimate the local angle of attack. Figure 4.13 shows the pressure distribution from cases $T1$ and $T2$ at a given value of $C_L \simeq 0.8$. As can be seen, the same value of lift is generated by two pressure distributions that are significantly different. This suggests that a given value of C_L can be generated

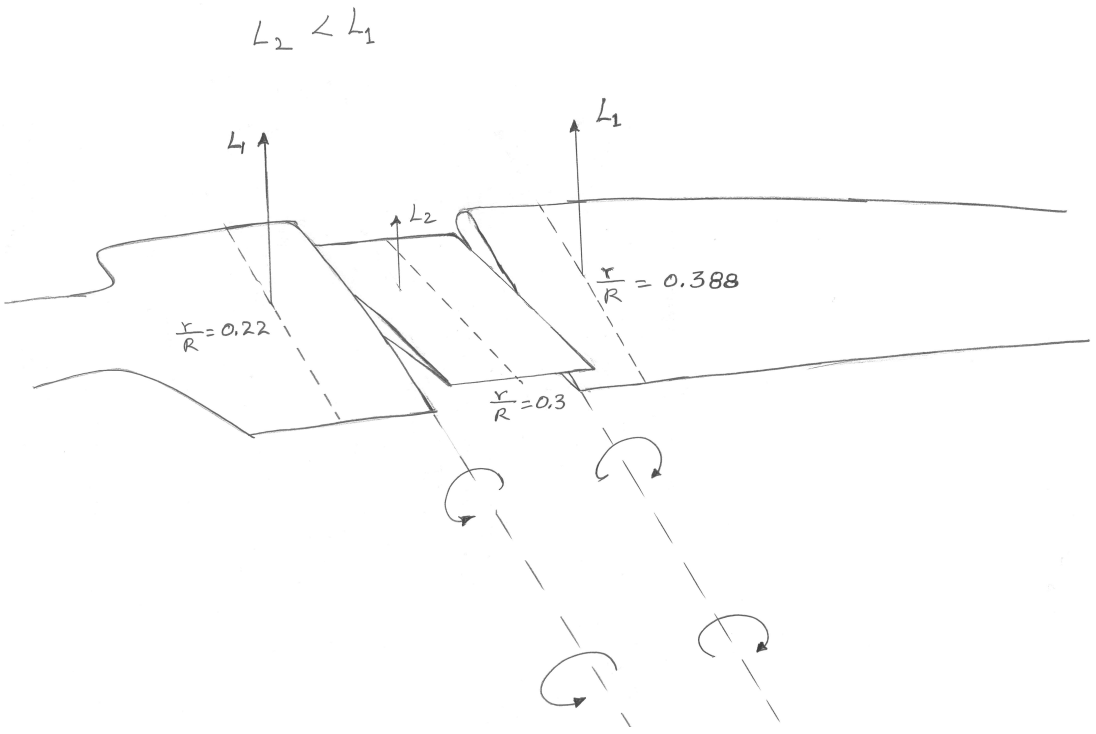

FIGURE 4.11: Schematic showing the vortices trailed on a wind turbine blade with a twist distribution $T2$ from Figure 3.5.

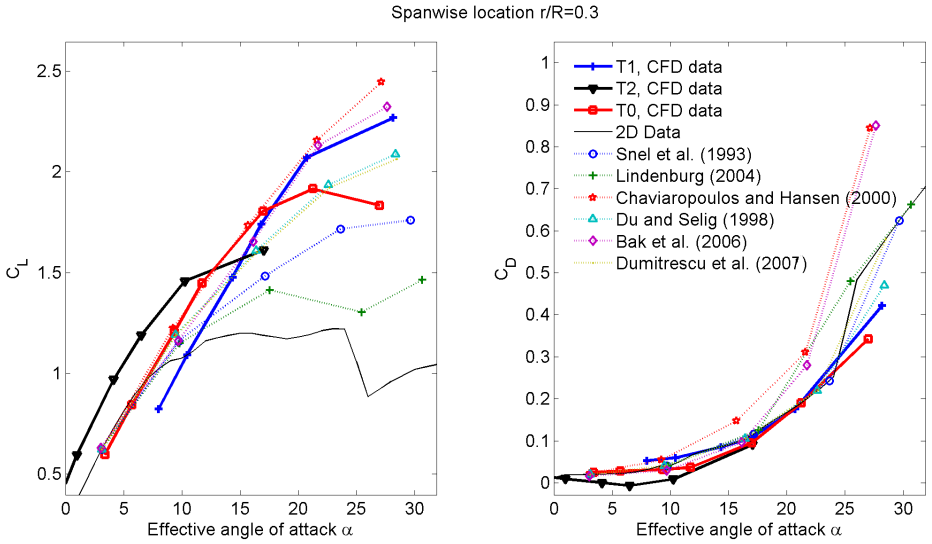

FIGURE 4.12: Lift and drag polars at the $r/R = 0.30$ section obtained from CFD simulations on the original and the re-twisted MEXICO rotor.

at different angles of attack. Therefore a correction in the induction (or the effective AOA) alone will probably not capture this phenomenon accurately, but rather the value of $C_{L,2D}$ itself might have to be corrected.

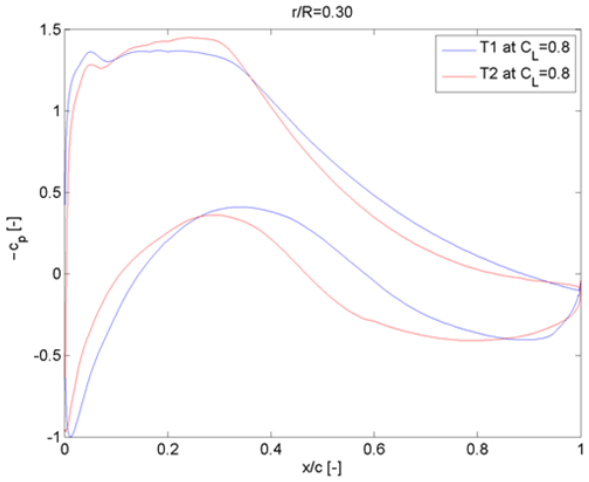

FIGURE 4.13: Pressure distributions at similar C_L values from the computations on the re-twisted MEXICO rotor models. The *T1* curve shows data from the computation at 10 m/s, resulting in a $C_L \simeq 0.8$. A *T2* curve at the same radial location was obtained by interpolating the data at 12 m/s and 15 m/s, so that it represents $C_L \simeq 0.8$ (see Figure 4.9).

4.3 Physical phenomena driving lift augmentation

The flow on the blade surface at different AOA was analysed in a recent paper in [62], and the conclusions from this paper are highlighted here.

Two important issues relating to the flow field in the rotor inboard sections that remain uncertain are: (1.) whether or not there is a downstream postponement of the separation point in rotation at a given AOA, and (2.) whether there is any difference in the AOA at which separation is initiated. Some insight into these issues has been gained by analysing the data from the full rotor CFD computations on the MEXICO rotor. Two inboard sections at the radial locations $r/R = 0.25$ and 0.35 were considered for the current analysis. At these two sections, the velocities, skin friction coefficients and the pressure distributions around the airfoil were extracted from the CFD computations. 2D CFD computations on the airfoils present on the MEXICO blade were also carried out at AOAs between $\alpha = 0°$ to $\alpha = 30°$ in steps of 1°. The 2D c_p distribution at a desired AOA was obtained by interpolation between the AOAs, which were then compared with the 3D data.

Figures 4.14 and 4.15 show comparisons between the pressure and the chord-wise skin friction coefficients between 2D and 3D full rotor computations, respectively. Flow separation in a 3D context is often challenging to define due to the complexity of the rotationally augmented flow fields. Consider the cases $U_\infty = 12$ and 15 m/s cases in Figure 4.17. Close to the root section (near $r/R < 0.25$), the streamlines closer to the trailing edge show a strong radial component and those close to the leading edge do

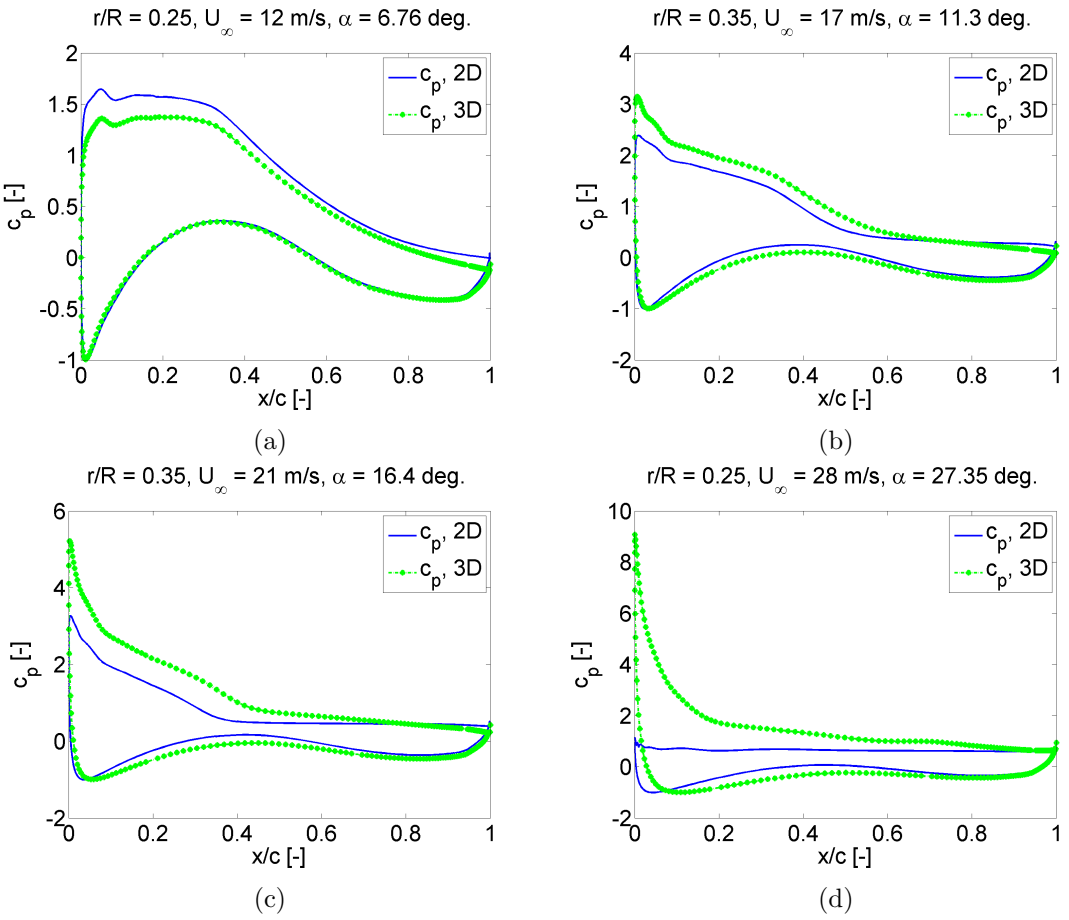

FIGURE 4.14: Plots (a) to (d) show the c_p distributions for some example cases of U_∞ and r/R shown therein, from the full rotor 3D CFD and 2D CFD computations of the DU91-W2-250 airfoil used in the inboard parts of the MEXICO blade.

not, and there is a distinct region where the flow transforms from being dominantly chord-wise flow to dominantly radial flow. By looking at the case $U_\infty = 12$ m/s and $r/R = 0.25$ in Figure 4.15a it can be seen that the chord-wise skin friction coefficient stays positive in this region, which means that even though radial flow is present the chord-wise component of the flow remains always positive. The proximity of the $r/R = 0.25$ section to the point of maximum chord $r/R \simeq 0.2$ means that the local flow is influenced significantly by the trailing root vortex, which may be the reason why radial flow is possible even in the absence of separation. For example, it was highlighted in [63] that the effect of the root vortex on the flow in the inboard part of the blade is radially outward. Separation in this work was determined as the location at which the chord-wise skin friction coefficient C_{fx} becomes zero, regardless of the visibility of flow patterns resembling separation lines on the blade surface. Tables 4.1 and 4.2 contain the separation location $C_{fx} = 0$ ordered by ascending AOAs, for the radial locations $r/R = 0.25$ and 0.35, respectively, at different free stream wind velocities.

Figure 4.17 shows the surface streamline patterns on the suction side of the MEXICO

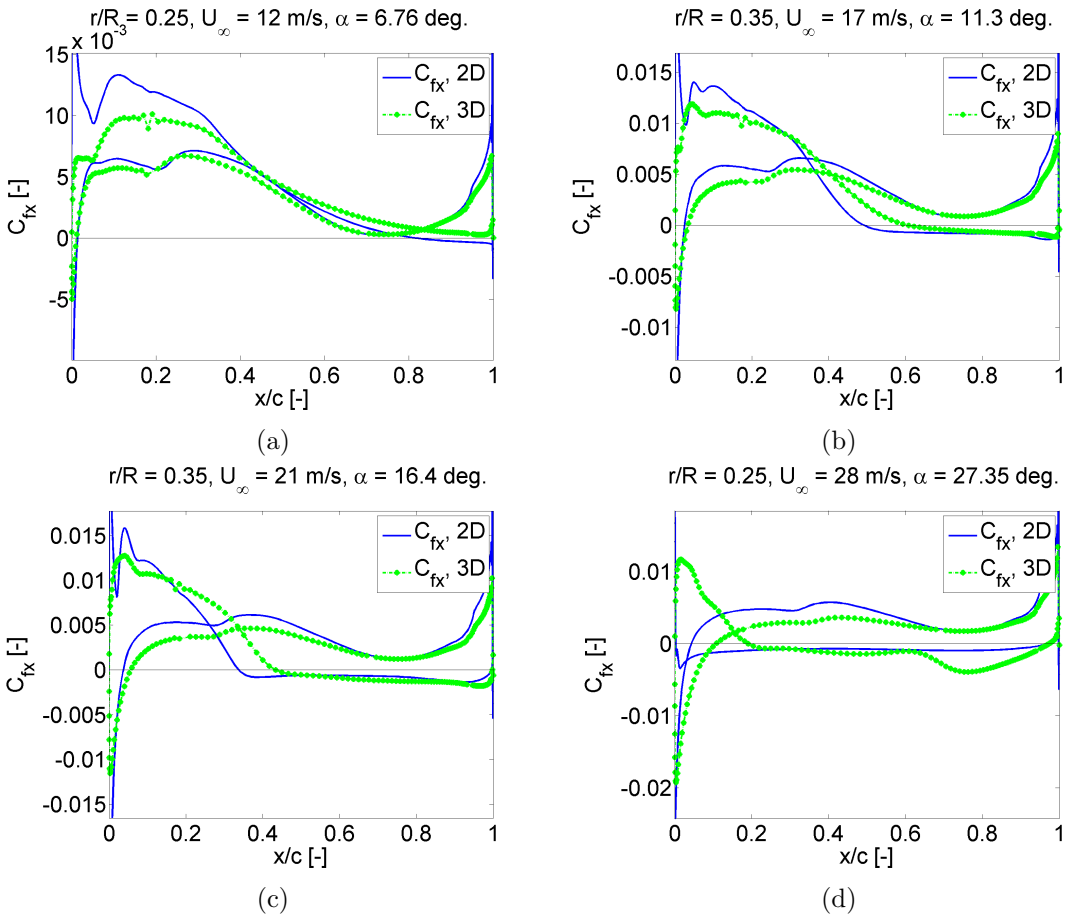

FIGURE 4.15: Plots (*a*) to (*d*) show the chord-wise skin friction coefficient C_{fx} from the full rotor 3D CFD and 2D CFD computations of the DU91-W2-250 airfoil used in the inboard parts of the MEXICO blade.

blade at different free stream velocities. The shaded parts of the blade represent the regions of separated flow ($C_{fx} \leq 0$). Consider cases $U_\infty = 15, 17$, and 21 m/s in the Figure 4.17. These images show that close to the leading edge of the airfoil the flow is dominantly in chord-wise direction, and close to the trailing edge the flow is dominantly radial. The flow transitions from being strongly chord-wise to strongly radial at a certain location on the blade surface, as highlighted in an example shown in Figure 4.18. What is interesting to note here is that the streamlines start to curve in the radial direction *before* the separation line, as highlighted in the example in Figure 4.18. This means radial suction (or the radial pumping) effect due to the centrifugal forces becomes dominant (in other words, the effect of rotational augmentation begins) even before the boundary layer separates. A separation point is a point where the chord-wise component of the relative velocity becomes zero, which in turn means that the fluid particle there moves along with the blade in the rotational reference frame. Just upstream of the separation line the fluid velocity is not zero, but is still small enough for centrifugal effects to start to dominate. This finding suggests that radial pumping, and thereby rotational

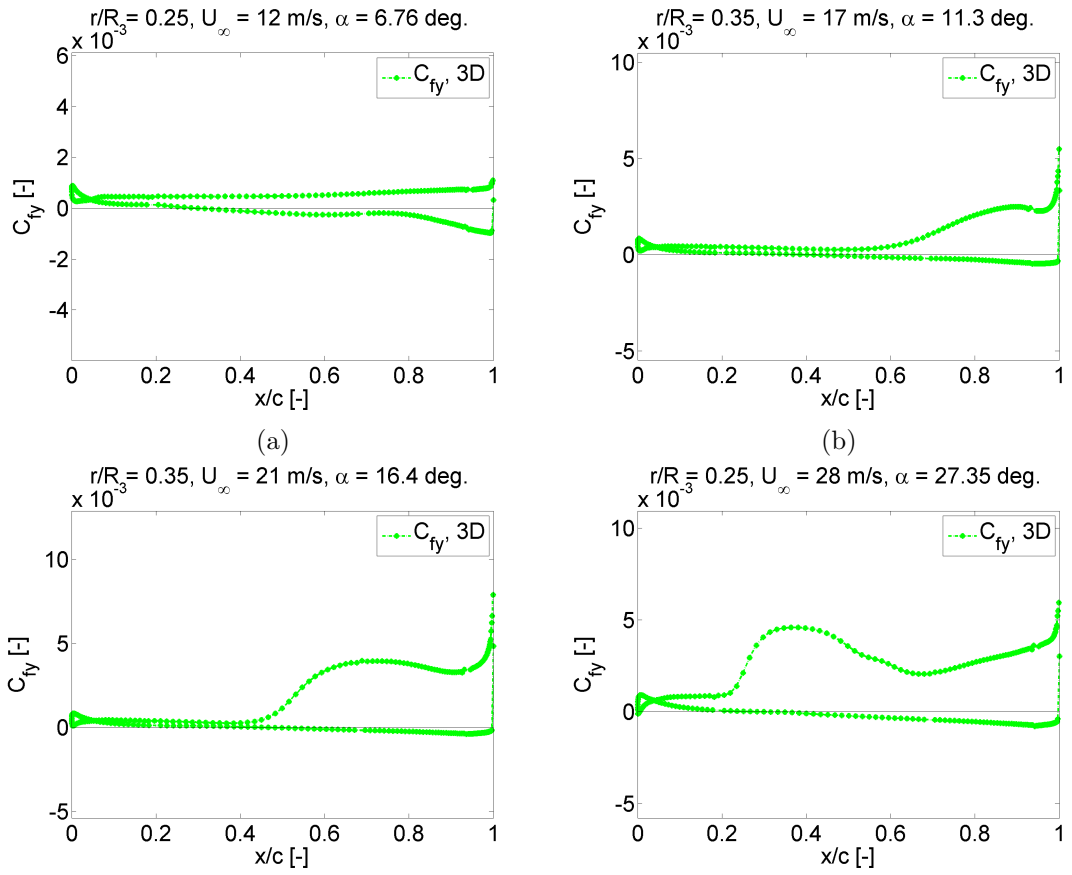

FIGURE 4.16: Plots (a) to (d) show the span-wise skin friction coefficient C_{fy} from the full rotor 3D CFD computations of the MEXICO turbine at the shown free stream velocity and span-wise locations. Here the y coordinate is in the radial direction, i.e., positive into the paper.

augmentation, may be present even on a rotating airfoil with no flow separation.

Images in Figure 4.19 show the separation bubble on the suction side of the airfoils for some of the 3D (images on the left hand side) and the 2D (images on the right hand side) cases at similar AOAs, obtained from CFD computations. Figures 4.19a, 4.19c and 4.19e show results from the 3D computations and Figures 4.19b, 4.19d and 4.19f show those from the full rotor 2D computations. In the 3D cases, the streamlines shown are relative velocity streamlines whose radial velocity component (the component towards/away from the reader) was forced to zero so as to be able to obtain these figures. By comparing the corresponding 3D cases Figures 4.19a, 4.19c, and 4.19e with the 2D Figures 4.19b, 4.19d, and 4.19f, it can be seen that the thickness of the separation bubble in rotation compared with the 2D case is reduced.

In order to represent the separation bubble quantitatively, a variable l is defined here as the maximum perpendicular distance between the airfoil surface and the limiting streamline, see Figure 4.20. The thickness of the separation bubble (l/c) is plotted

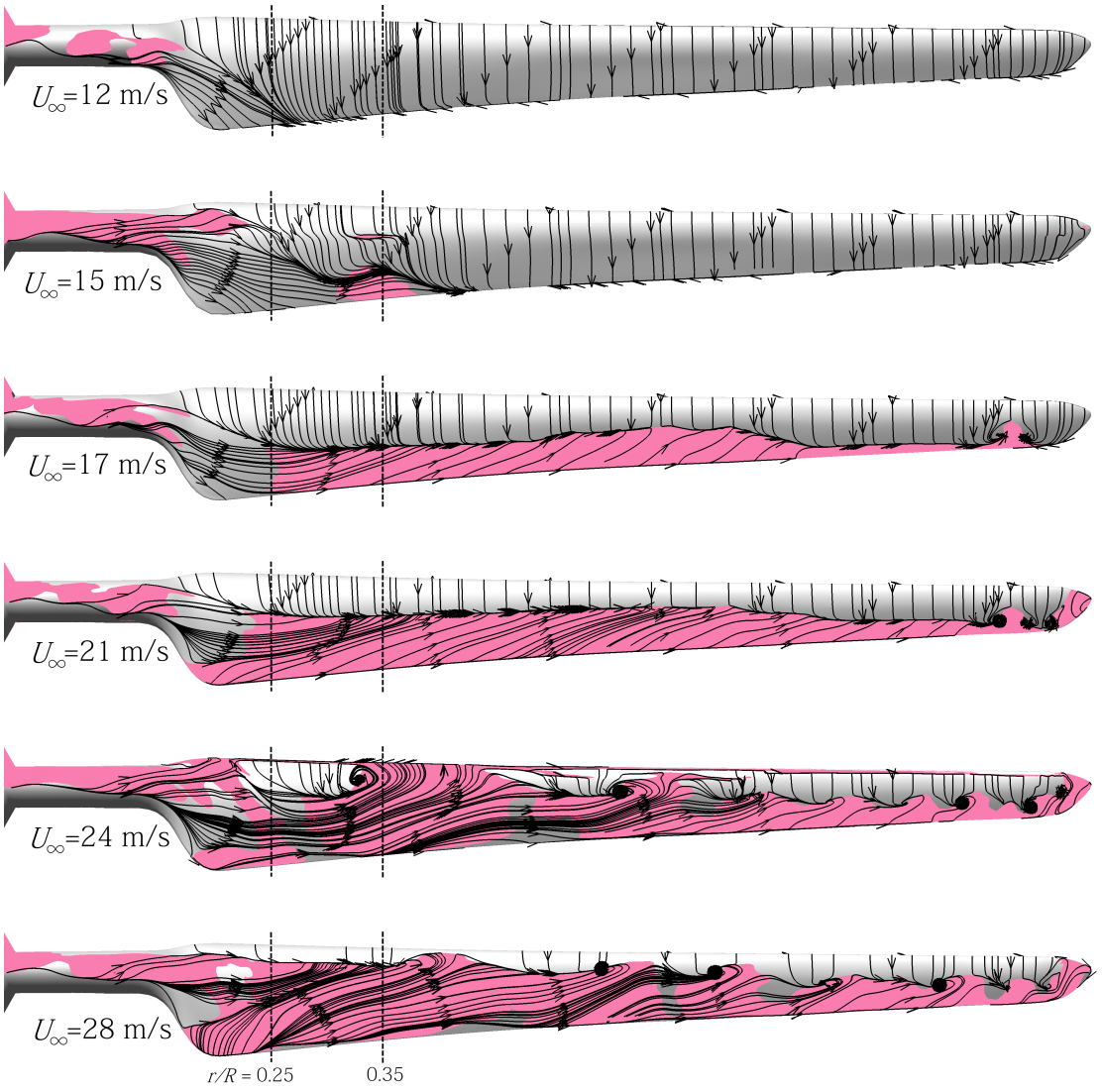

FIGURE 4.17: The suction-side streamlines on the MEXICO blade from full rotor computations at velocities $U_\infty = \{12, 15, 17, 21, 24, 28\}$ m/s. The shaded region represents separated flow, defined as $C_{fx} \leq 0$.

against the AOA in Figure 4.21a, where it can be seen that that the separation bubble gets thinner with decreasing r/R. That is, stall on airfoils rotating in the inboard regions of a blade is suppressed.

Consider the case $U_\infty = 24$ m/s in Figure 4.17. The surface streamlines show a vortex at the location $r/R \simeq 0.32$ close to the leading edge ($x/c \simeq 0.2$). Due to the presence of this vortex it seems that the the flow in its vicinity is distorted such that the streamlines form in a counter-clockwise direction around the vortex. This seems to shift the separation point at $r/R = 0.25$ to a higher x/c value (towards the trailing edge), and that at $r/R = 0.35$ to a lower x/c value (towards the leading edge). This effect is reflected in the data points corresponding to the $U_\infty = 24$ m/s shown in Figure 4.21b (the data points $\alpha = 23.5°$ on the $r/R = 0.25$ curve and $\alpha = 20.7°$ on the $r/R = 0.35$ curve).

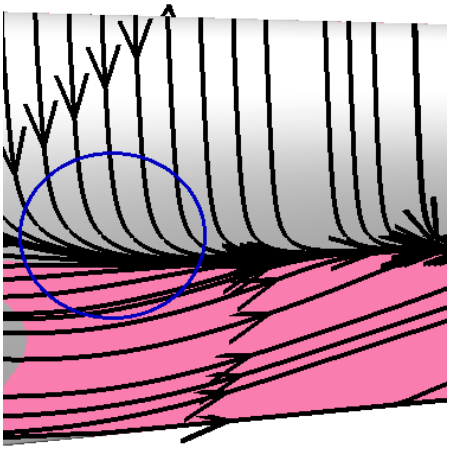

FIGURE 4.18: A closer look at the region $0.25 \leq r/R \leq 0.35$ from the case $U_\infty = 17$ m/s shown in Figure 4.17. It can be observed that the streamlines begin to curve radially outwards before separating from the surface.

U_∞ [m/s]	Re [-]	α [°]	$(x/c)_{C_{fx}=0}$, 3D [-]	$(x/c)_{C_{fx}=0}$, 2D [-]
12	3.95×10^5	6.76	1	0.815
15	4.15×10^5	10.52	1	0.538
17	4.31×10^5	12.93	0.595	0.41
21	4.65×10^5	18.41	0.413	0.30
24	4.94×10^5	23.05	0.556	0.173
28	5.35×10^5	27.35	0.19	0

TABLE 4.1: Estimated separation point locations from 2D and 3D full rotor computations on the MEXICO rotor for similar AOAs, at $r/R = 0.25$.

This peculiar flow behaviour is specific to the case $U_\infty = 24$ m/s, and it is not seen to be prominent in the other cases.

Considering the rest of the cases $U_\infty = 12, 15, 17, 21, 28$ m/s in Figure 4.21b, some interesting observations can be made. It can be seen that the AOA at which separation is initiated increases as r/R decreases, which means that the initiation of separated flow (or stall) in 3D is delayed to a higher AOA compared to the same airfoil in 2D flow. Further, it can be seen that for a given AOA the location of separation point in 3D is also postponed to a more downstream chord-wise location, compared to the corresponding 2D case. This postponement is highest at the most inboard section $r/R = 0.25$, and the $r/R = 0.35$ curve lies in between the $r/R = 0.25$ and the 2D curves. This is consistent with the idea that as r/R increases the 3D curve approaches the 2D curve. Sicot et

U_∞ [m/s]	Re [-]	α [°]	$(x/c)_{C_{fx}=0}$, 3D [-]	$(x/c)_{C_{fx}=0}$, 2D [-]
12	4.54×10^5	5.39	1	0.905
15	4.67×10^5	8.84	0.73	0.655
17	4.78×10^5	11.28	0.60	0.484
21	5.01×10^5	16.42	0.433	0.33
24	5.21×10^5	20.66	0.006	0.245
28	5.50×10^5	25.89	0.216	0.054

TABLE 4.2: Estimated separation point locations from 2D and 3D full rotor computations on the MEXICO rotor for similar AOAs, at $r/R = 0.35$.

al. performed a similar analysis in [30], where the authors conclude that rotational augmentation has little to no effect on the location of the separation point. However, the current results contradict their conclusion.

In sum, according to the current analysis, it seems that there is indeed a delay in stall, in terms of (1.) a delay in the AOA at which separation is initiated, (2.) a postponement of the separation point at a given AOA, as well as (3.) a suppression of the separated region of the boundary layer.

4.3.1 Behaviour of c_p distributions in rotating flow

A common practice for identifying trailing edge separation on airfoils is by identifying a region of zero pressure gradient on the suction side c_p curve. This method is commonly used in analysing experimental data, where the c_p distribution is often the only data available that is suited for this purpose. For example, by this method separation can be identified to occur at approximately $x/c = 0.5$ in the 2D curve shown in Figure 4.14b. This method was used previously in determining trailing edge separation in 3D rotating flows by several researchers, for example see [64]. Figures 4.14, 4.15 and 4.16 show the c_p, C_{fx} and C_{fy} data for four of the cases discussed in Tables 4.1 and 4.2. Consider Figures 4.14b and 4.14c that show pressure distributions at $\alpha = 11.3°$ and $\alpha = 16.4°$, respectively. The suction side c_p curve from 2D computations in these figures has a zero gradient beyond the corresponding separation point, but the 3D c_p curve in this region has a (approximately constant) non-zero slope. The corresponding chord-wise skin friction data in Figures 4.15b and 4.15c shows that the change in chord-wise skin friction (chord-wise velocity gradient) is very small in this region. By looking at the span-wise skin friction coefficient shown in Figures 4.16b and 4.16c, an increase in C_{fy}

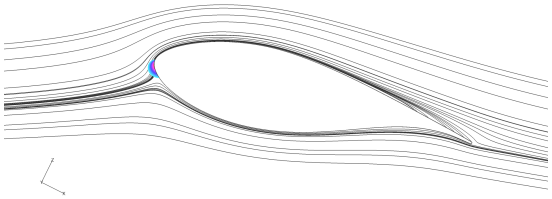

(a) Relative velocity streamlines from a full rotor computation at $U_\infty = 15$ m/s. The section shown is $r/R = 0.25$, with $\alpha \simeq 10.5°$.

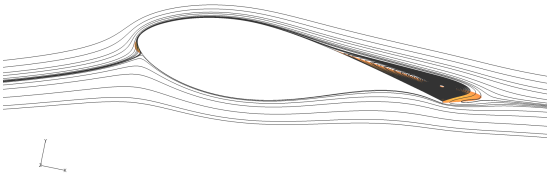

(b) Streamlines from a 2D CD computation on the DU91-W2-250 airfoil at $\alpha = 10°$ and a Reynolds number Re$= 4 \times 10^5$.

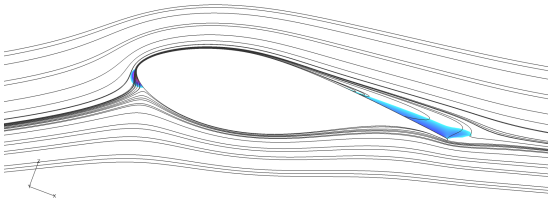

(c) Relative velocity streamlines from a full rotor computation at $U_\infty = 17$ m/s. The section shown is $r/R = 0.35$, with $\alpha \simeq 11.3°$.

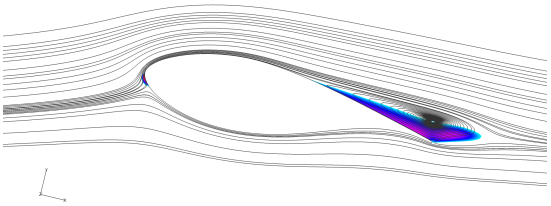

(d) Streamlines from a 2D CD computation on the DU91-W2-250 airfoil at $\alpha = 11°$ and a Reynolds number Re$= 4 \times 10^5$.

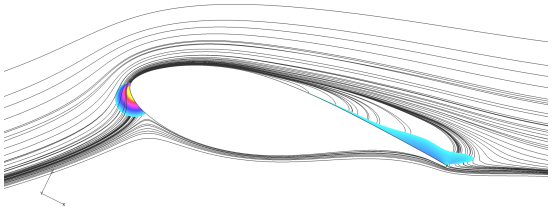

(e) Relative velocity streamlines from a full rotor computation at $U_\infty = 21$ m/s. The section shown is $r/R = 0.25$, with $\alpha \simeq 18.4°$.

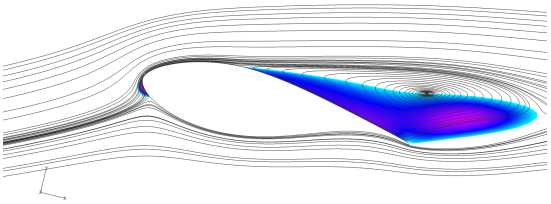

(f) Streamlines from a 2D CD computation on the DU91-W2-250 airfoil at $\alpha = 18°$ and a Reynolds number Re$= 4 \times 10^5$.

FIGURE 4.19: Streamlines around the DU91-W2-250 airfoil obtained from the full rotor 3D (left) and 2D (right) CFD computations for a few example cases. The streamlines from the 3D computations shown are relative velocity streamlines whose radial velocity component (the component into the paper) was forced to zero. The coloured region on the suction side of the airfoil represents the chord-wise (x) component of the relative velocity $u_{x,rel} \leq 0$.

can be seen in the separated region. This indicates that the constant non-zero pressure gradient observed in the separated region in rotating airfoils is due to radial pumping.

Figures 4.14d, 4.15d and 4.16d show the c_p, C_{fx} and C_{fy} data for another case at a higher AOA, respectively. In this case, there is heavy separation, C_{fx} becomes 0 at $x/c \simeq 0.19$. The behaviours of C_{fx} and C_{fy} in this case are different from the two cases studied in the previous paragraph, where C_{fx} in the separated region had a small negative value throughout the separated region. It this case, C_{fx} has a small negative value in the region $0.2 < x/c < 0.6$, whereas in the region $x/c > 0.6$ suddenly there is an increase in the negative skin friction, as shown in Figure 4.15d. In the c_p distribution

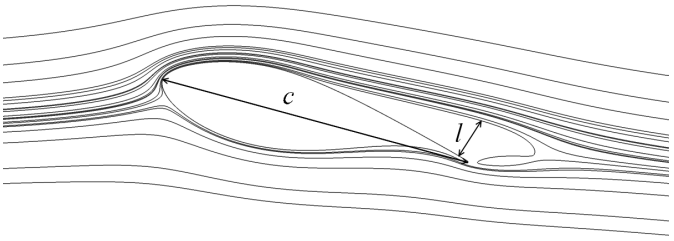

FIGURE 4.20: Definition of the variable l used in estimating the thickness of the separation bubble.

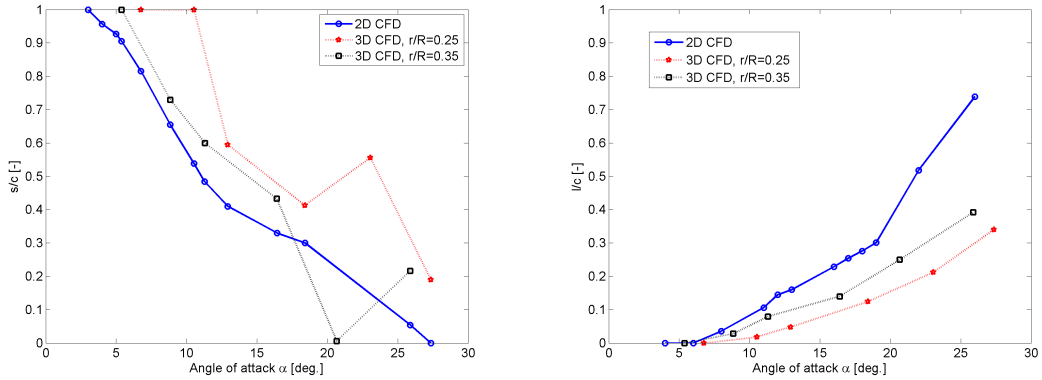

(a) (b)

FIGURE 4.21: Estimates of the separation point location (a) and the thickness of the separation bubble (b) as a function of the angle of attack. In (a), $s/c = 0$ corresponds to the leading edge and $s/c = 1$ corresponds to the trailing edge of the airfoil. The quantity l/c in plot (b) is as defined in Figure 4.20.

shown in Figure 4.14d it can bee seen that the suction side pressure curve too does not have a constant slope as in the previous two cases studied, but has a small variation in its slope visible near $x/c = 0.60$.

The finding that the 3D c_p distributions may have neither a zero nor a constant slope beyond the separation point means that the estimation of the separation point location using c_p distributions can be unreliable.

4.3.2 Influence of turbulence on rotational augmentation

In recent paper from 2012, Gross et al. [33] performed a DNS computation of an airfoil section using the Navier-Stokes equations with added forcing terms to account for rotational forces. They identify two effects in their analysis and suggest that these are responsible for rotational augmentation:

1. Separation is delayed in a turbulent boundary layer compared to a laminar boundary layer.

2. Transition from laminar to turbulent flow in rotation is initiated/expedited by crossflow structures in the boundary layer that arise due to centrifugal and Coriolis forces.

That is, [33] suggests that rotational augmentation is caused primarily due to the delay in separation caused by the transition of the blade boundary layer from laminar to turbulent flow. Although the two independent effects are known to be true, it is believed by the current author and the supervisor that the conclusions derived from these two effects may be questionable. This was highlighted in a Letter to the Editor, journal of wind energy, in [34]. In this letter, the following comments were made.

Laminar boundary layer analyses by [18] and [25] suggested a delay in separation even when turbulence was neglected completely. It is therefore questionable whether it is necessary to invoke the argument of laminar to turbulent transition to explain rotational augmentation.

Rotational augmentation is observed even in the case of experiments with blades with a leading edge tripping tape, for example in case of the MEXICO experiment [14]. Therefore, rotational augmentation exists even in the case where the boundary layer is fully turbulent far upstream of the separation point, which suggests that rotational augmentation is likely not driven by transition.

Since it is evident from the two points above that rotational augmentation exists in both fully laminar and turbulent cases, it can be said that the role of transition on the same is not first order significant. For example, McCroskey from his experimental analysis [19] also highlighted that the transition from laminar to turbulent flow is dominated by the chordwise adverse pressure gradient and a conventional laminar separation bubble, rather than by rotational or cross-flow effects.

The analysis was carried out at a Reynolds number $Re = 100000$, and at only one angle of attack $\alpha = 5°$. A similar analysis with either higher Re or varying free stream turbulence could have given a better insight into the problem. Sicot et al. [30], for example, highlighted that free stream turbulence level indeed influences the separation point location, but this is not responsible for rotational augmentation.

If the aim of the work was to investigate the dominant mechanism behind rotational augmentation, then it is also wondered why only one angle of attack was chosen for analysis. It can be hard to identify and quantify rotational augmentation in lift at low

angles of attack as the separated region on airfoils is generally small. Similar computations at higher angles of attack could give a better insight into separation, as done by [26] for example.

4.4 Summary

In this chapter, first an analysis on the rotational augmentation models were presented where the models by Du and Selig [24, 25], Dumitrescu et al. [31, 36, 37], and Bak et al. [29], were identified to give the most reliable results for the lift, and the model by Bak et al. for the drag and the moment. Later, the influence of a change in the span-wise loading on the local aerodynamics were investigated. It was identified that trailing vorticity, which is caused due to a change in the span-wise loading, results in an effect similar to that typically observed near the blade tip. The pressure and the skin friction distributions on the airfoils at the inboard parts of the MEXICO rotor were compared with those from 2D computations on the same airfoil geometry. It was identified that there is indeed a delay in stall, in terms of (1.) a delay in the AOA at which separation is initiated, (2.) a postponement of the separation point at a given AOA, as well as (3.) a suppression of the separated region of the boundary layer. Finally, comments were made on the effect of turbulence on rotational augmentation.

In the following chapter, an investigation of the effect of unsteadiness on the aerodynamics of the inboard parts of wind turbine blades is presented.

Chapter 5

Results and Discussion: Dynamic stall

This chapter presents the results from investigations on the unsteady behaviour of aerodynamic forces on the inboard parts of the blade. Much of this work has been documented in the articles [65] and [66]. The documented results as well as some new results are presented in the current chapter in detail.

The N sequence data of the NREL UAE Phase VI experiment described in Chapter 3 was used in this study as a benchmark dataset. Unsteady DDES CFD computations were also carried out for select cases of the N sequence experiment. As a first part of the study, comparisons were made between the forces obtained from the experiment and the CFD computations. Then, the comparisons were made between polars estimated form the experimental data and those estimated using a reduced order dynamic stall model described in Section 2.4.1.

5.1 Rotating vs. non-rotating experimental data

From the literature review presented in Section 2.2.1 as well as the current research presented in Chapter 4, it has been fairly well established that the inboard sections the flow field on the blade is rotationally augmented. Therefore, the first step in studying dynamic stall in the inboard parts of a wind turbine would be to examine how lift during dynamic stall behaves in the inboard regions. Figure 5.1a shows the lift polars in stationary and rotating, steady and unsteady conditions, obtained from the experimental data at $r/R = 0.47$ and a reduced frequency of pitching $K = 0.1$. The lift curve from the steady rotating case (blue dotted line, J-sequence) shows higher lift than the steady

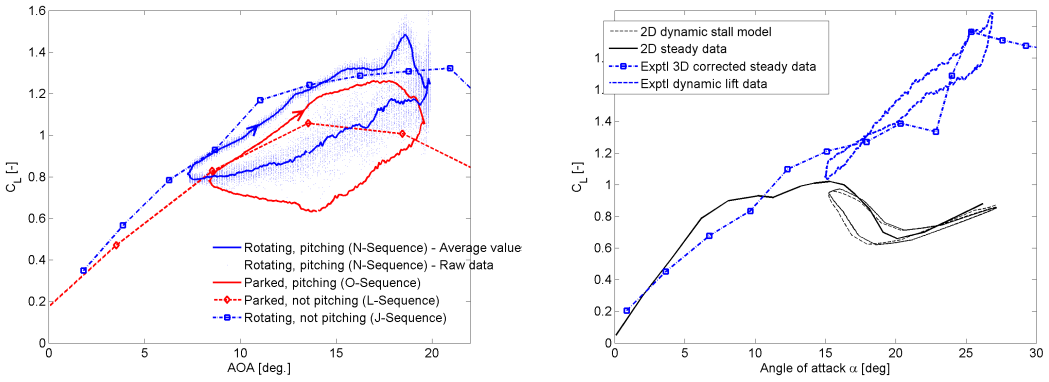

(a) (b)

FIGURE 5.1: Dynamic stall on the UAE Phase VI rotor blades: (*a*) The experimental $C_L - \alpha$ curves from different operating conditions is shown for an example case, at the radial location $r/R = 0.47$ and a reduced pitching frequency of $K = 0.1$. This figure shows the same dynamic stall case for the rotating and non-rotating UAE Phase VI rotor. (*b*) In this example, experimental data from the N sequence shows the hysteresis in lift. The same dynamic stall case is also simulated with the model of Hansen et al. [4], using polars obtained from steady 2D wind tunnel tests at Re$= 7.5 \times 10^5$ from [2].

stationary (red dotted line, L-sequence), which is due to rotational augmentation. The hysteresis loop formed by the rotating and pitching case (solid blue line, N-sequence) shows higher lift compared to the stationary pitching case (solid red line, O-sequence), indicating that lift in dynamic stall is also augmented in rotation. Note that the area enclosed in the hysteresis loop of the N-sequence is smaller than that of the O-sequence. If the area within the $C_L - \alpha$ hysteresis loop is an indication of the severity of stall on the blade, this observation is consistent with the idea that stall is suppressed in rotation, and that this has an effect on dynamic stall. Figure 5.1b shows an example where experimental data at $K = 0.1$ is compared with that from a dynamic stall model using 2D data, highlighting the importance of accounting for rotational augmentation while modelling dynamic stall.

5.2 CFD vs. Experimental data

Three cases N47090, N47350 and N47020 were simulated by unsteady DDES CFD computations. Forces from the CFD data were extracted at those span wise locations where the pressure data was available from the original experiment. Figures 5.2, 5.3 and 5.4 show data from the cases N47090, N47350 and N47020, respectively. The normal and tangential (measured parallel and perpendicular to the chord) force coefficients shown here are at the $r/R = 0.47$ location, obtained from CFD simulations and the experiment. The details regarding the operating effective angles of attack, reduced frequency of pitching and pitching amplitude of all of the N-sequence experimental cases studied in

Case Nr.	K $(r/R = 0.30)$	α_M $(r/R = 0.30)$	K $(r/R = 0.47)$	α_M $(r/R = 0.47)$	α_Ω
N47020	0.090	4.5	0.063	2.0	2.37
N47030	0.090	13.9	0.063	11.6	4.79
N47050	0.108	10.8	0.075	8.3	2.50
N47090	0.143	10.7	0.100	8.1	2.37
N47140	0.179	6.5	0.125	3.9	1.19
N47150	0.179	14.6	0.125	12.2	1.27
N47170	0.036	15.7	0.025	13.4	6.28
N47180	0.036	21.2	0.025	19.7	5.84
N47230	0.072	15.7	0.050	13.4	6.50
N47240	0.072	21.1	0.050	19.8	5.98
N47290	0.108	15.9	0.075	13.6	6.46
N47300	0.108	21.3	0.075	20.0	5.98
N47350	0.143	15.8	0.100	13.5	6.33
N47360	0.143	21.2	0.100	20.0	5.98

TABLE 5.1: Table showing the values of the parameters reduced frequency (K), mean AOA (α_M) and the amplitude of oscillation (α_Ω) for all the N sequence cases that are discussed in this thesis.

this thesis are tabulated in Table 5.1. In the NREL experiments, the pitch was defined positive towards a decreasing angle of attack.

Consider the two cases N47090 and N47350, shown in Figures 5.2 and 5.3, respectively. The case N47090 operates at a pitching amplitude of $\alpha_\Omega = 2.37°$ and mean angle of attack of $\alpha_M = 8.2°$. The case N47350 operates at a pitching amplitude of $\alpha_\Omega = 6.33°$ and mean angle of attack of $\alpha_M = 13.5°$. Both cases operate at the same pitching frequency $K = 0.1$, and show good agreement between experimental and CFD data. The case N47090 shown in Figure 5.2 shows a very good agreement between the CFD and the experimental data in C_N as well as C_T. The case N47350, which operates at a higher mean AOA of $\alpha_M = 13.5°$, shows that there is good qualitative agreement between the two data sets but during the reattachment phase of the dynamic stall process the CFD data predicts a more severe stall than that seen in the experiments. It has been highlighted before in [67] that the stochastic nature of flow in this region makes it a challenge to model, and it is believed that this is the reason for the observed difference between the experimental and CFD results. The third case N47020 operates at a lower

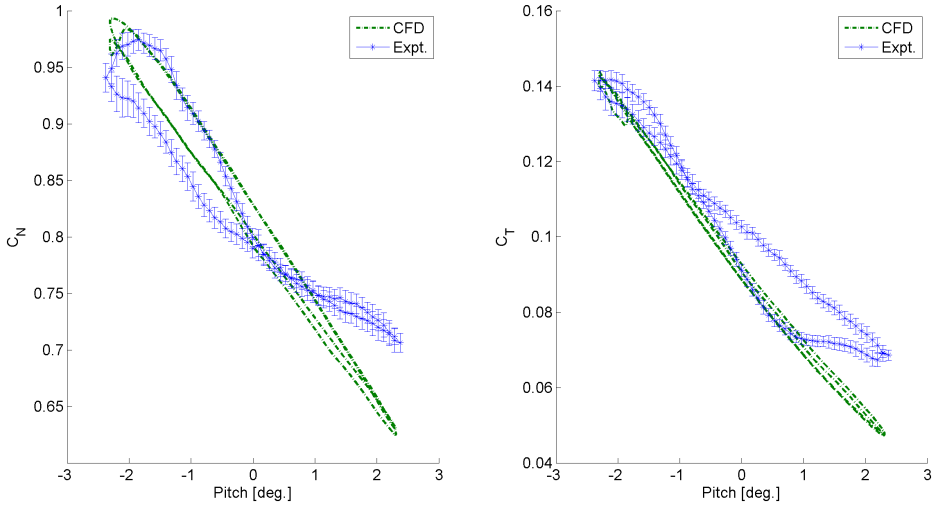

FIGURE 5.2: Case N47090: The C_N and C_T as functions of the pitch angle for the case at $r/R = 0.47$, $K = 0.1$ and a mean AOA of $\alpha_M \simeq 8.2°$. The error bars on the experimental data denote one standard deviation.

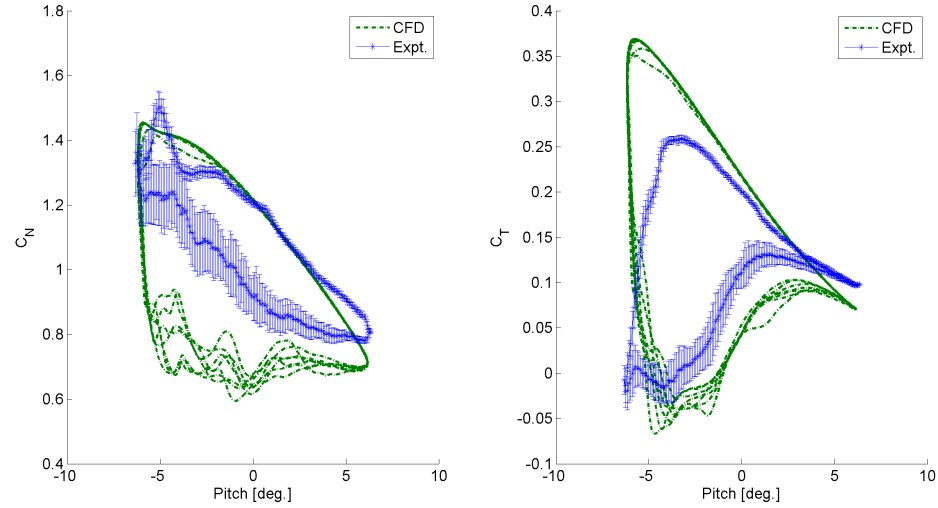

FIGURE 5.3: Case N47350: The C_N and C_T as functions of the pitch angle for the case at $r/R = 0.47$, $K = 0.1$ and a mean AOA of $\alpha_M = 13.5°$. The error bars on the experimental data denote one standard deviation.

pitching frequency of $K = 0.0625$ and a lower mean AOA compared to the previous two cases, of $\alpha_M = 2.0°$. In Figure 5.4, the comparison between the C_N and C_T shows that the CFD data predicts a lower force than that obtained from the experiment.

The pressure distribution around the airfoil section at $r/R = 0.47$ for the three N sequence cases being studied were extracted at eight instances within a pitch cycle. The time instances within the pitch cycle are labelled (a) to (h) in Figure 5.6. Figures 5.7, 5.8 and 5.9 show the c_p distributions at these time instances corresponding to cases N47090, N47350 and N47020, respectively. Figures 5.7 and 5.8 show a very good agreement

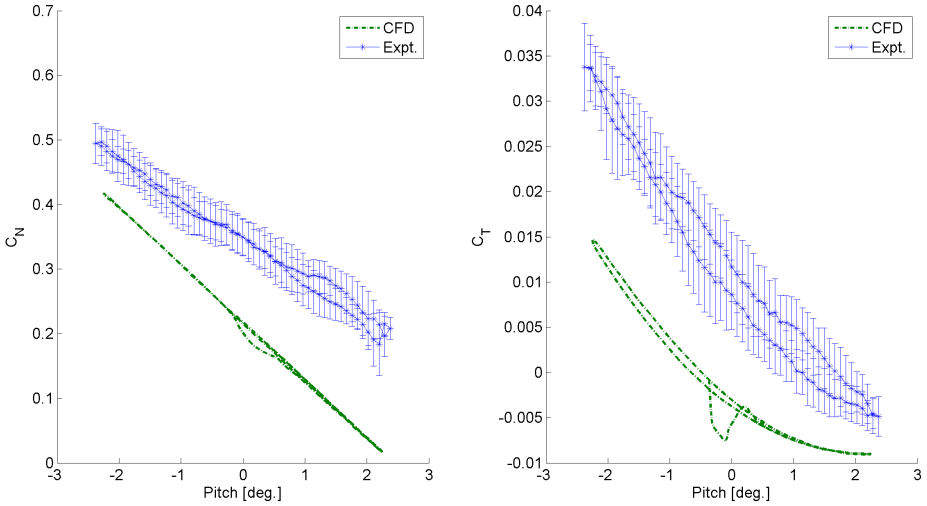

FIGURE 5.4: Case N47020: The C_N and C_T as functions of the pitch angle for the case at $r/R = 0.47$, $K = 0.0625$ and a mean AOA of $\alpha_M = 2.0°$. The error bars on the experimental data denote one standard deviation.

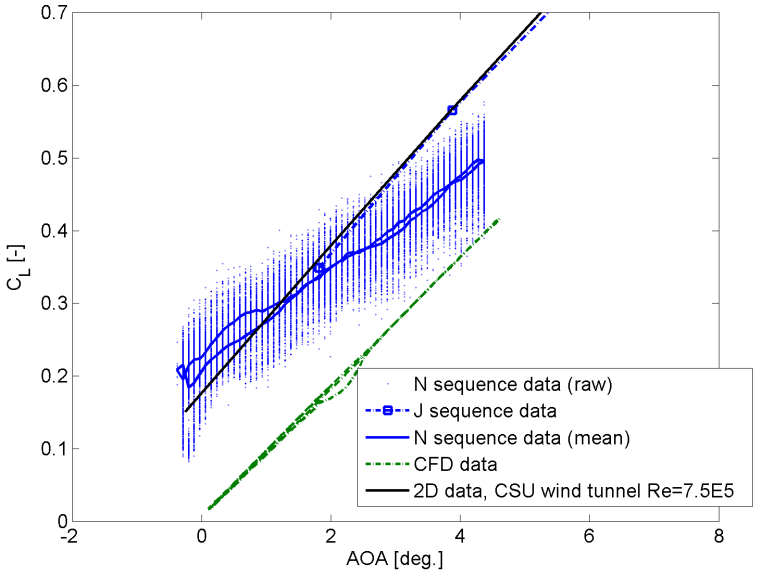

FIGURE 5.5: The $C_L - \alpha$ curves for the case N47020 at $r/R = 0.47$, obtained from CFD computations and the experiments shown in the legend.

between the experimental and the CFD pressure distributions. In these two cases, the only significant deviation between the experimental and CFD pressure data occurs in Figures 5.8g and 5.8h, which is in the reattachment phase at a high AOA. Figure 5.9 shows the same c_p distribution comparison between the experiments and CFD for the case N47020. The same disagreement with the experimental data seen in the forces highlighted in the previous paragraph can be seen in the pressures as well. Note that the resolution of the experimental pressure data is lower than that of the CFD data. For

example, the region $0.3 < x/c < 0.6$ in Figures 5.7 clearly shows that although there is an agreement between the experimental and the CFD data at the pressure tap locations, in between the pressure tap locations the shape of the c_p is not linear. Forces on the blades are obtained by integrating these pressure distributions, and therefore the lack of detail in pressure measurements adds an uncertainty to the estimated force.

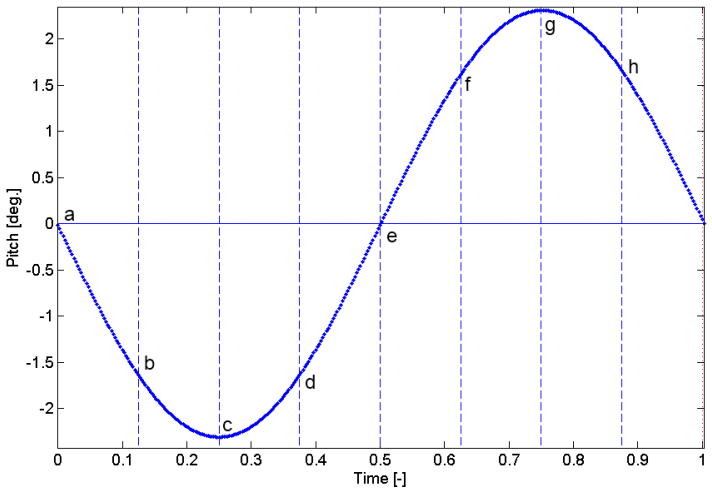

FIGURE 5.6: The blade pitch (y-axis) vs. time (x-axis, normalized by the pitching time period) is shown for an example case N47090. The vertical lines show the time instances at which the c_p were extracted to be shown in Figures 5.9, 5.7 and 5.8. In this CFD data, the pitch is defined positive towards stall.

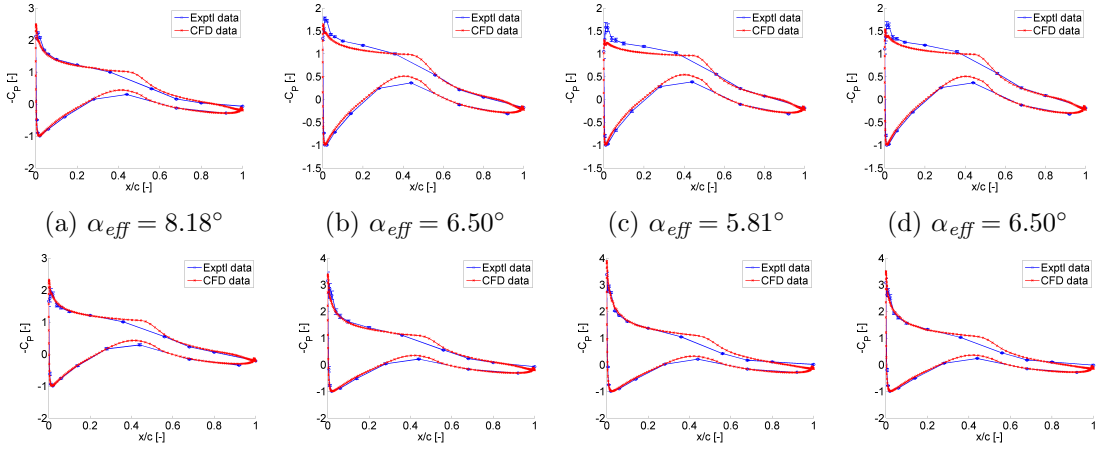

(a) $\alpha_{eff} = 8.18°$ (b) $\alpha_{eff} = 6.50°$ (c) $\alpha_{eff} = 5.81°$ (d) $\alpha_{eff} = 6.50°$

(e) $\alpha_{eff} = 8.18°$ (f) $\alpha_{eff} = 9.86°$ (g) $\alpha_{eff} = 10.55°$ (h) $\alpha_{eff} = 9.86°$

FIGURE 5.7: Plots (a) to (h) show the c_p distributions at the 8 time instances shown in Figure 5.6) ordered chronologically. Data shown is from the experiment as well as CFD computations for the case N47090 at $r/R = 0.47$ with local $K = 0.01$. The error bars on the experimental data points denote one standard deviation.

One possibility for the disagreement between CFD and experimental data seen in the case N47020 is that the absence of the nacelle and the tower in the CFD model gives rise to flow structures in the inboard region that are different from the experiment,

which contained a nacelle and a tower. Another possibility could be in connection with observations made in Section 4.2, that the lift in the regions close to the root or the tip is lower than its 2D value for a given AOA. If the root vortex was not modelled accurately in the CFD computation, the lower lift obtained by CFD could be an over-estimated effect of the trailing root-vortex. One final possibility could be that there is an error in the experimental measurements in this specific sequence, N47020. Figure 5.5 shows the $C_L - \alpha$ curves obtained from the J-sequence, 2D measurements, the N sequence experimental data for the case N47020, and the CFD data for the same N sequence case. Since there is qualitative agreement between the J-sequence data, N-sequence data and 2D data, and only the CFD data disagrees with the rest, it can be concluded that the CFD simulation in this case was not able to model the flow accurately.

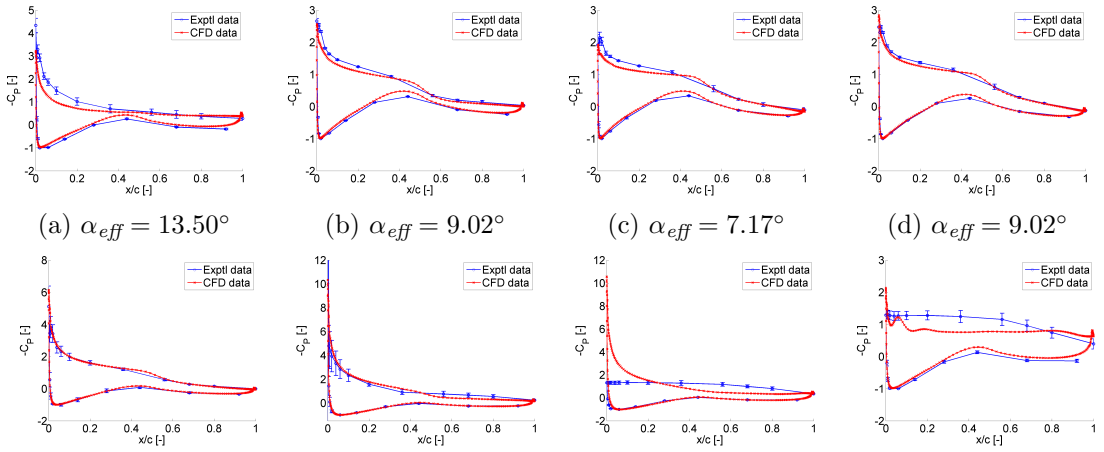

(a) $\alpha_{eff} = 13.50°$ (b) $\alpha_{eff} = 9.02°$ (c) $\alpha_{eff} = 7.17°$ (d) $\alpha_{eff} = 9.02°$

(e) $\alpha_{eff} = 13.50°$ (f) $\alpha_{eff} = 17.98°$ (g) $\alpha_{eff} = 19.83°$ (h) $\alpha_{eff} = 17.98°$

FIGURE 5.8: Plots (a) to (h) show the c_p distributions at the 8 time instances ordered chronologically, as shown in Figure 5.6). Data shown is from the experiment as well as CFD computations for the case N47350 at $r/R = 0.47$ with local $K = 0.01$. The error bars on the experimental data points denote one standard deviation.

Although the DDES CFD simulations were able to generate good results for two out of the three cases studied (cases N47090 and N47350), it apparently has some limitations which restrict its accuracy in modelling case N47020. Further investigation is needed to analyse this discrepancy in more detail, which is outside the scope of the current study. For carrying out rest of the analysis only the experimental data has been used as a benchmark for the reduced order dynamic stall model.

5.3 Dynamic stall model vs. experimental data

Most engineering models for dynamic stall that are used in BEM-based codes use 2D lift and drag polars as the input. A more realistic approach to modelling dynamic stall in the inboard parts would be to use polars that are corrected for rotational augmentation

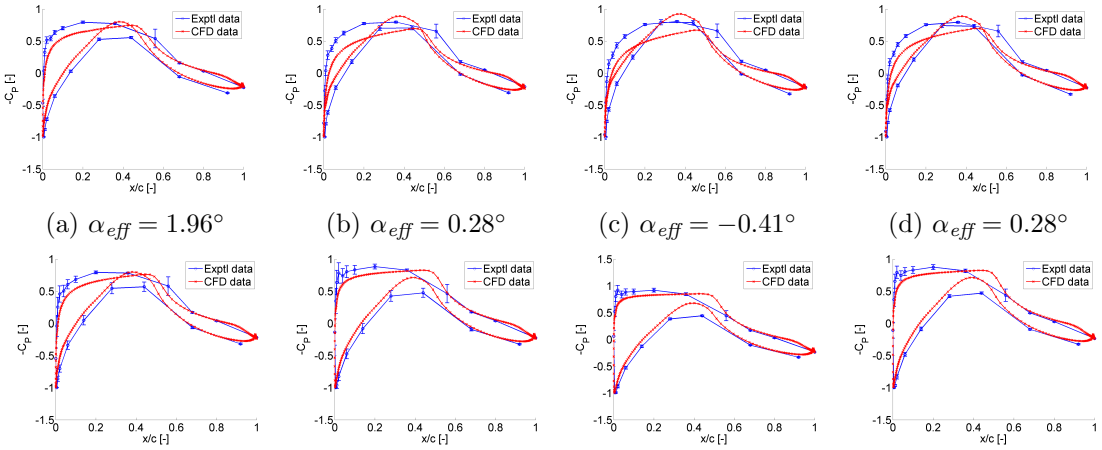

(a) $\alpha_{eff} = 1.96°$ (b) $\alpha_{eff} = 0.28°$ (c) $\alpha_{eff} = -0.41°$ (d) $\alpha_{eff} = 0.28°$

(e) $\alpha_{eff} = 1.96°$ (f) $\alpha_{eff} = 3.64°$ (g) $\alpha_{eff} = 4.33°$ (h) $\alpha_{eff} = 3.64°$

FIGURE 5.9: Plots (a) to (h) show the c_p distributions at the 8 time instances shown in Figure 5.6 ordered chronologically. Data shown is from the experiment as well as CFD computations for the case N47020 at $r/R = 0.47$ with local $K = 0.0625$. The error bars on the experimental data points denote one standard deviation.

as the input to the dynamic stall model, instead of the 2D data. It has been seen in Section 4.1 that some of the existing rotational augmentation models are capable of estimating 3D lift and drag polars qualitatively. However, it is questionable whether any of these rotational augmentation models are quantitatively reliable enough to correct the 2D polars, to be used as an input to the the dynamic stall model. The idea of using rotational augmentation model together with dynamic stall model in a BEM code is explored further in Chapter 6. In this section, the lift, drag and moment polars obtained from experimental data have been used. The effect AOAs in this section were estimated using an inverse BEM method, as described in Section 3.3.2.

The first two span wise locations, $r/R = 0.30$ and 0.47, were investigated in the current work using fourteen N sequence test cases. The test case numbers, and the values of the parameters K, α_M and α_Ω for these cases are shown in Table 5.1. In real life wind turbines, an exciting frequency of 1P (rotor rotation frequency), such as in yawed operation, results in a dynamic stall reduced frequency of approximately $K \simeq 0.1$. The test cases chosen here operate in the ranges $0.036 < K < 0.18$, $2° < \alpha_M < 21°$ and $1.2° < \alpha_\Omega < 6.5°$, which covers many possible cases that can occur on real wind turbines. The lift and moment polars for selected cases are shown in Figures 5.10 to 5.15.

Figures 5.10 and 5.11 show the lift and moment polars for the cases N47180 and N47360, respectively, at the section $r/R = 0.30$. The case N47180 operates at a low pitching frequency of $K = 0.036$ and the case N47360 operates at $K = 0.143$. Both of these cases operate at $\alpha_M = 21.2°$ and approximately $\alpha_\Omega \simeq 5.9°$. Similarly, Figures 5.12 and 5.13 a comparison between the cases N47170 and N47350, respectively. Here too, the two figures respectively show slow pitching $K = 0.036$ and fast pitching $K = 0.143$

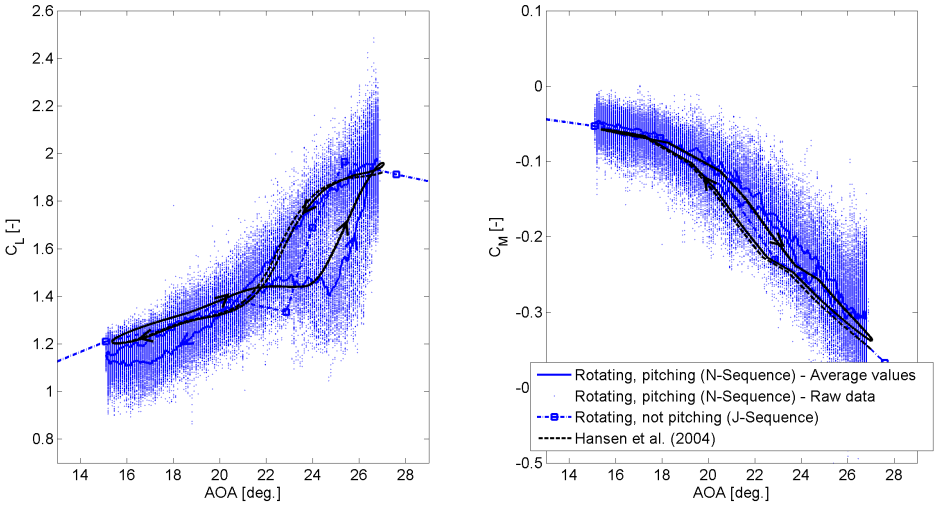

FIGURE 5.10: Case N47180: Lift and moment polars at $\alpha_M = 21.2°$, $\alpha_\Omega = 5.84°$, $r/R = 0.30$, $K = 0.036$.

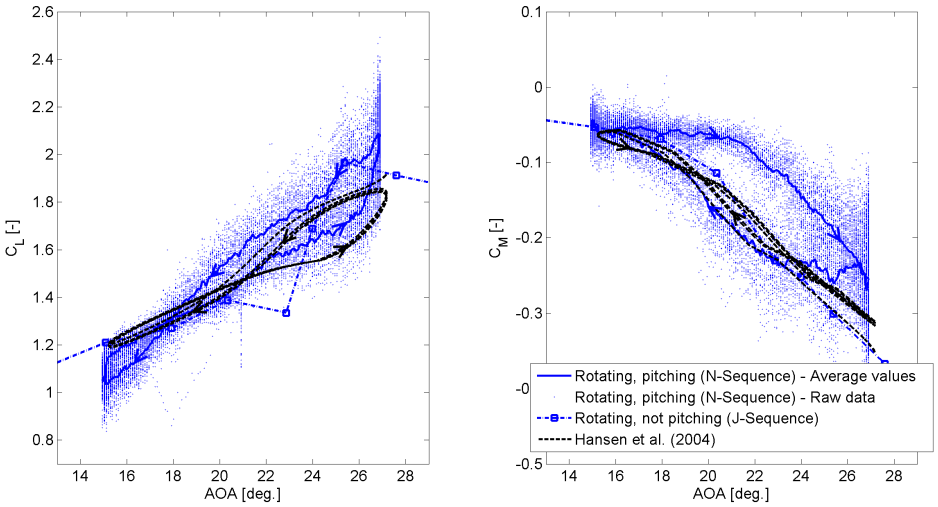

FIGURE 5.11: Case N47360: Lift and moment polars at $\alpha_M = 21.2°$, $\alpha_\Omega = 5.98°$, $r/R = 0.30$, $K = 0.143$.

conditions with approximately the same amplitude of $\alpha_\Omega = 6.3°$, but at a lower mean AOA of $\alpha_M \simeq 15.8°$. The latter two cases shown in Figures 5.12 and 5.13 show a small difference between the model and the experimental data, i.e., the magnitude of lift estimated by the model is slightly higher than that from the experimental data. This effect is slightly more pronounced in Figure 5.13, with the average difference between the experimental and model lift data being approximately 0.17. The lift estimated by the model is a dependant upon the steady $C_L - \alpha$ curve that is used as an input, which in this case is the J sequence experimental data shown in the same figure. Therefore, the difference between the C_L loops estimated using the model and the experimental data is

basically a difference between the J sequence and N sequence data sets, which could just be a minor uncertainty associated with the experimental data. The area enclosed within the C_L hysteresis loops in these figures, on the other hand, are very similar between the experimental data and the model. All in all, these four cases present a comparison across high and low pitching frequencies, and at high and low mean AOAs. In all the four cases, the $C_L - \alpha$ curves obtained from the model and the experimental data show very good agreement.

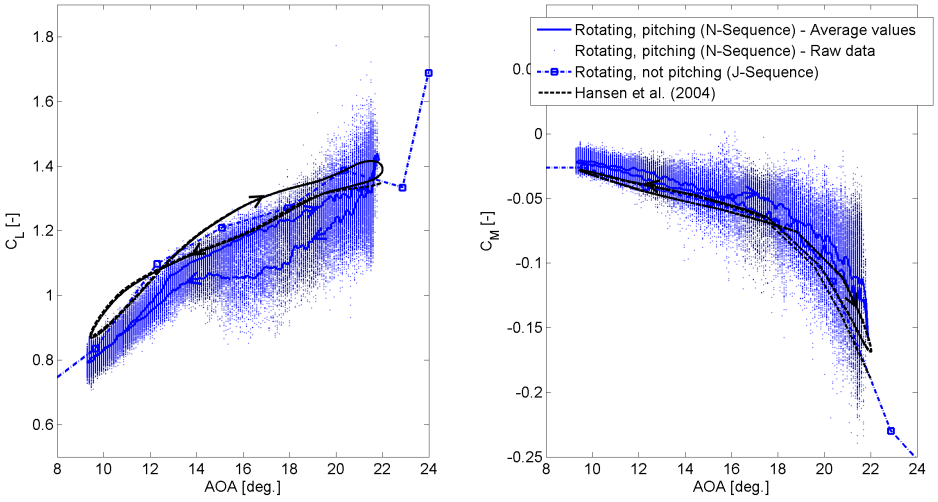

FIGURE 5.12: Case N47170: Lift and moment polars at $\alpha_M = 15.7°$, $r/R = 0.30$, $K = 0.036$.

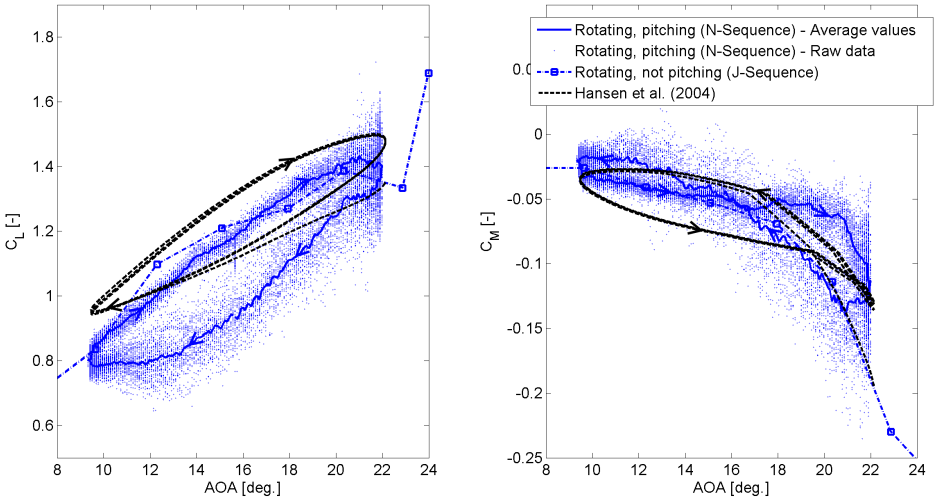

FIGURE 5.13: Case N47350: Lift and moment polars at $\alpha_M = 15.8°$, $r/R = 0.30$, $K = 0.143$.

The coefficient of moment is also an important parameter in modelling dynamic stall, as the hysteresis in C_M is an indication of aerodynamic damping for the pitching moment:

a counterclockwise loop in the $C_M - \alpha$ curve denotes positive damping, and vice versa. Figures 5.10 and 5.12, which show cases that operate at the same pitching frequency of $K = 0.036$ but different mean AOAs, show a good agreement between the model $C_M - \alpha$ data and experimental data. This shows that at this pitching frequency, the model and experiments agree well for varying mean AOA.

On the other hand, Figures 5.11 and 5.13 show cases that operate at a higher pitching frequency of 0.143 and different mean AOAs. It can be seen here that the agreement between the experimental and model data in this case is not as good as it was at previous lower K. In Figure 5.11, the experimental C_M curve shows a larger area within the C_M loop than the estimation by the model, whereas in Figure 5.13, which is at the same (high) pitching frequency at a lower mean AOA, the experimental C_M curve shows a smaller area enclosed within the C_M curve than that estimated by the model. This means that at higher frequencies the model consistently (between the two cases shown here) predicts a more positive torsional damping.

In the dynamic stall process at moderate to high AOAs (involving partial or full separation), boundary layer reattachment occurs as the blade pitches from its maximum AOA towards lower AOA [38]. During the reattachment phase, the lift coefficient for a given AOA is typically lower than that during ascending AOA. This is shown in Figure 5.1a for example, where the lift during increasing AOA is higher than the lift during decreasing AOA in the N sequence and O sequence curves. It is interesting to note that Figures 5.10 and 5.11 show loops in the C_L curve in the *opposite* direction, i.e., in the region approximately $21° < \alpha < 27°$ the lift is lower during ascending AOA and higher during its descent. This is seen to occur at the most inboard section $r/R = 0.30$, where the rotational augmentation effects are the strongest. It has been highlighted before in Chapter 4 that rotational augmentation suppresses separation, causing an increase in lift. On the other hand, reattachment process in dynamic stall cannot occur if there is no separation. Therefore, even though the AOA is very high in this region, separation probably does not occur in these cases. The C_L behaviour in these cases is also captured very accurately by the model.

Figure 5.15 shows a similar comparison at the radial location $r/R = 0.80$. At this outboard location, rotational augmentation effects are little to none. As is clearly visible, the dynamic stall model performs very well in predicting both the lift and moment polars in this region. The fact that the model works equally well in both inboard and outboard regions implies that the physics of dynamic stall are the qualitatively the same in the presence and absence of rotational augmentation effects. The only information the dynamic stall model requires in order to accurately model lift and moment coefficients in unsteady conditions is the 3D corrected polars. This observation is significant as it

implies that rotational augmentation and dynamic stall can be modelled separately and the models can be superimposed while coupling with a BEM based aeroelastic code.

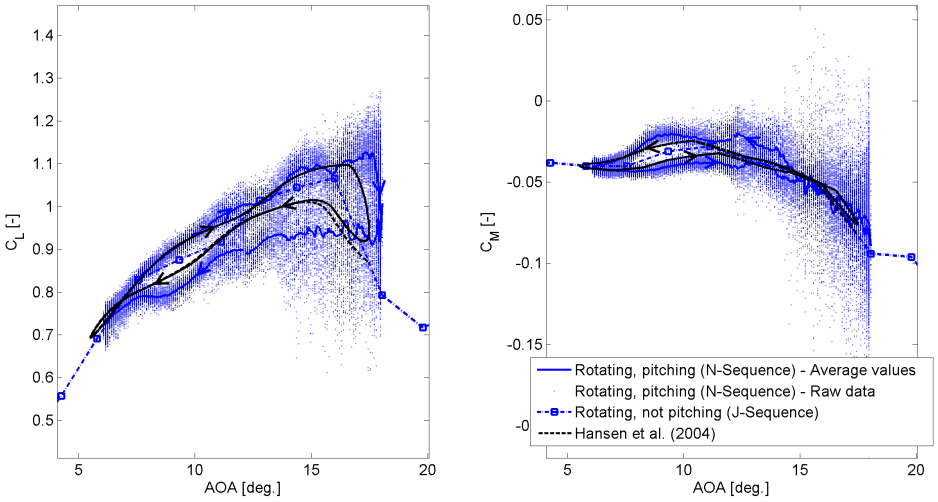

FIGURE 5.14: Case N47240: Lift and moment polars at $\alpha_M = 11.5°$, $r/R = 0.80$, $K = 0.024$.

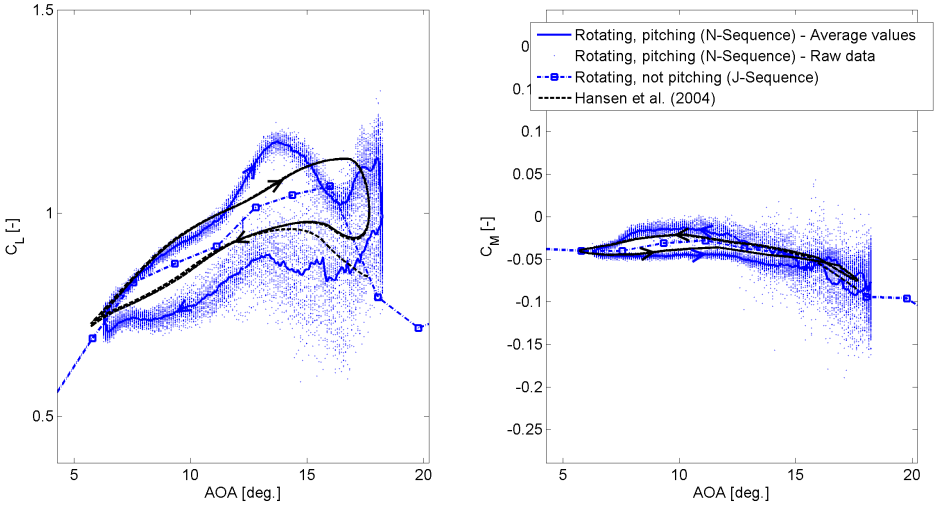

FIGURE 5.15: Case N47240: Lift and moment polars at $\alpha_M = 11.7°$, $r/R = 0.80$, $K = 0.048$.

5.4 Summary

In this chapter, an investigation of dynamic stall on the inboard parts of rotating airfoils was presented. The comparison between the experimental and the CFD data revealed good qualitative and quantitative agreement in one of the three cases, reasonable qualitative agreement in one another of the three cases, and moderate qualitative agreement

with some clear differences in the third, highlighting once again the challenge modelling the complex dynamic stall process. On the other hand, the comparison between the reduced order dynamic stall engineering model showed good agreement in many of the cases studied, although some quantitative difference was seen in some of the cases. Over all, the results showed that the phenomenon in rotating and non-rotating airfoils is similar, and the reduced order dynamic stall model is seen to perform well in modelling the lift and reasonable in modelling the moment.

Chapter 6

Case study

Based on the inferences made in the previous chapters, a case study was carried out where a set of N sequence cases from the NREL Phase VI experiment were simulated using a BEM code coupled with a the rotation augmentation model of Bak et al. [29] and the dynamic stall model of Hansen et al. [4]. The aim of this case study is to investigate whether the loads on an inboard part of a wind turbine blade operating in unsteady conditions can be accurately modelled by a simple BEM code equipped with the discussed aerodynamic correction models.

Several N sequence cases with different operating conditions were simulated using a BEM code. Figures 6.1 to 6.11 show the lift and moment polars from the following sources: the unsteady experimental data from the N sequence, the steady state experimental data from the J sequence, the 3D corrected polars, and the estimated loads from the model.

Figures 6.1, 6.2 and 6.3 show the estimated and measured loads on the blades for the case N47030 at the three inboard sections $r/R = \{0.30, 0.47, 0.63\}$, respectively. The estimated mean AOAs and pitching frequencies at the three locations are $\alpha = \{13.9°, 11.56°, 7.6°\}$, and $K = \{0.09, 0.0625, 0.044\}$, respectively. The loads at the radial locations $r/R = 0.47$ and 0.63 by the model compare well with the experimental data.

Figures 6.4 and 6.5 show two cases operating at the same mean AOA and, pitching amplitudes, but different pitching frequencies: $K = 0.036$ and 0.143, respectively, at $r/R = 0.30$. Similarly, Figures 6.6 and 6.7 show two cases operating at the same mean AOA and pitching amplitudes, but different pitching frequencies: $K = 0.036$ and 0.143, respectively, at $r/R = 0.30$. Based on the discussion on the effect of trailed vorticity in Section 4.2, it is expected that there is some disagreement at the most inboard section due to its proximity to the blade root. For this reason, the lift estimated by the model is higher than the measurements for a given AOA in Figure 6.1. The same can also be

seen in Figures 6.4 to 6.7, which also show the data from $r/R = 0.30$. On the other hand, even though there is a disagreement between the 3D corrected lift polars and the experimental data, the hysteresis in lift estimated by the model compares qualitatively well with the measurements.

Figures 6.8 to 6.11 show data from the radial location $r/R = 0.47$, at varying K, α_M and α_Ω values (the operating conditions highlighted in the figure captions). Figures 6.8 and 6.9 show data at a mean AOA of around 13.5°, and Figures 6.10 and 6.11 show data at a higher mean AOA of around 20°. As shown by the figures, there is good agreement between the modelled and measured forces in the cases operating at a lower mean AOA, $\alpha_M \simeq 13.5°$. However, the agreement is worse at the cases at a higher mean AOA $\alpha_M \simeq 20°$ shown in Figures 6.10 and 6.11. Since modelling aerodynamic phenomenon at higher AOAs (deep stall conditions) is difficult, the AOA range in which the BEM based models can accurately estimate the loads seems limited. Most wind turbines are not designed to operate in deep stall conditions, so the performance of models in deep stall is only a minor concern.

In some of the cases, for example in Figures 6.2, there is a disagreement in the steady state C_M data: 3D corrected C_M curve (dotted black line) and that from the J sequence experimental data (dotted blue curve). This deviation also reflects in a disagreement in unsteady data between the model and the measurements. To the author's knowledge, there have been no detailed studies on the effect of rotational effects on the moment coefficient C_M. Depending upon its practical relevance, investigation into rotational effects on pitching moment could be an interesting research problem. Judging by the hysteresis loops in C_M in the cases presented herein, the overall trend seems to be that there is good qualitative agreement between the estimated by the model and the measurements.

In conclusion, it has been seen from this case study that the results from the BEM model seem to be reasonable in the tested range of pitching frequencies, mean AOAs and pitching amplitudes. Based on the cases studied herein, the BEM model seems to deliver promising results qualitatively. However, higher quantitative accuracy of reduced order models maybe limited due to the fact that separated flow is a challenge to model even using the more rigorous methods such as CFD.

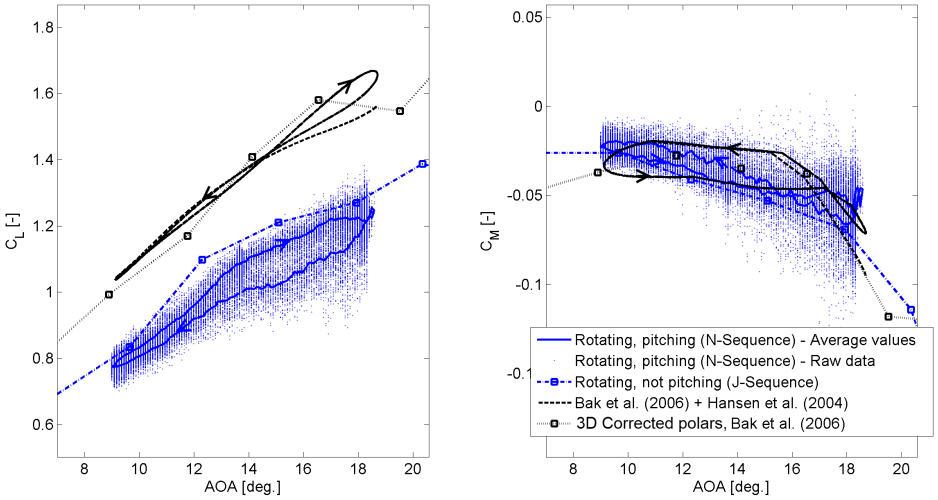

FIGURE 6.1: Case N47030: Lift and moment polars at $\alpha_M = 13.9°$, $\alpha_\Omega = 4.79°$, $r/R = 0.30$, $K = 0.090$.

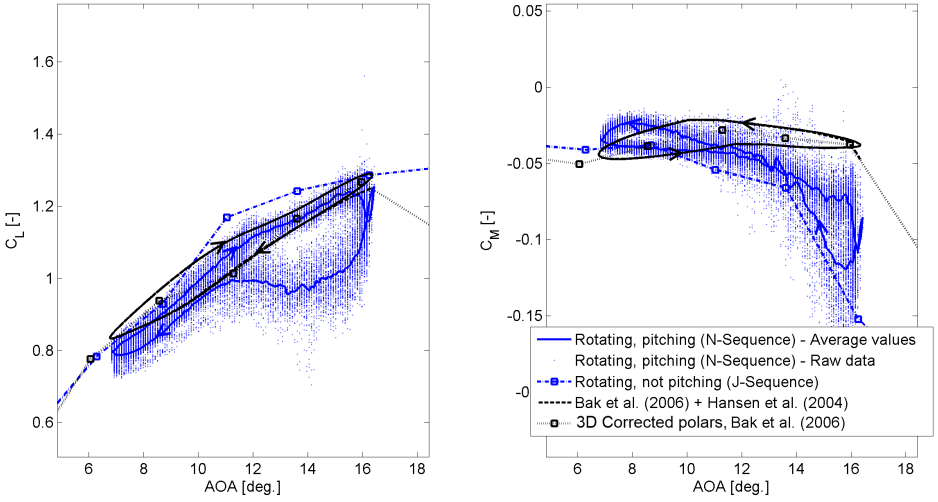

FIGURE 6.2: Case N47030: Lift and moment polars at $\alpha_M = 11.6°$, $\alpha_\Omega = 4.79°$, $r/R = 0.47$, $K = 0.0625$.

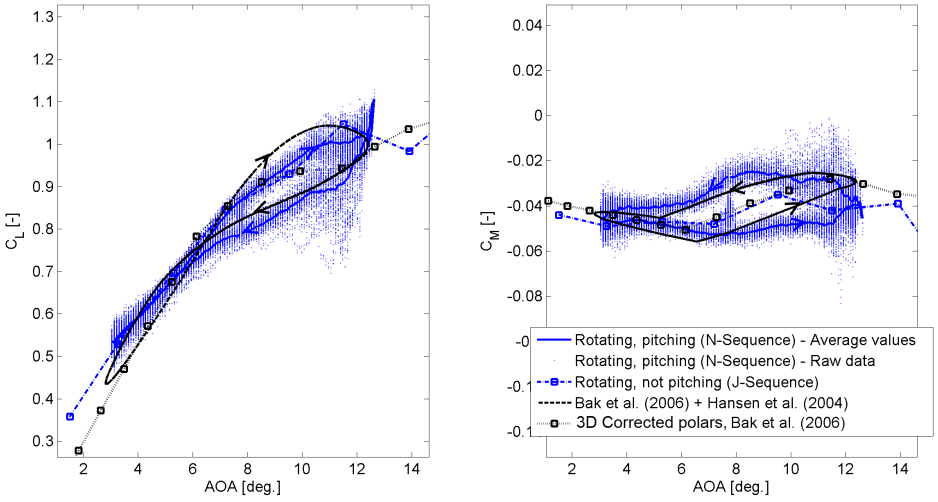

FIGURE 6.3: Case N47030: Lift and moment polars at $\alpha_M = 7.6°$, $\alpha_\Omega = 4.79°$, $r/R = 0.63$, $K = 0.044$.

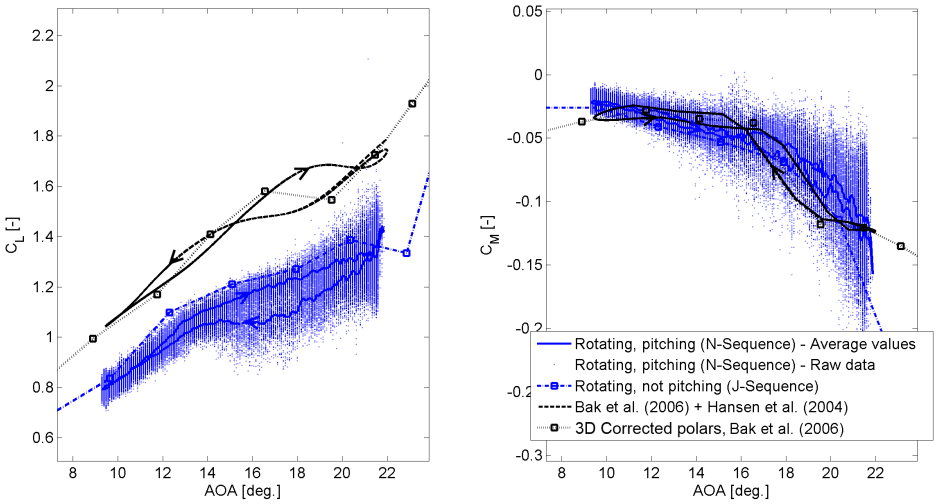

FIGURE 6.4: Case N47170: Lift and moment polars at $\alpha_M = 15.7°$, $\alpha_\Omega = 6.28°$, $r/R = 0.30$, $K = 0.036$.

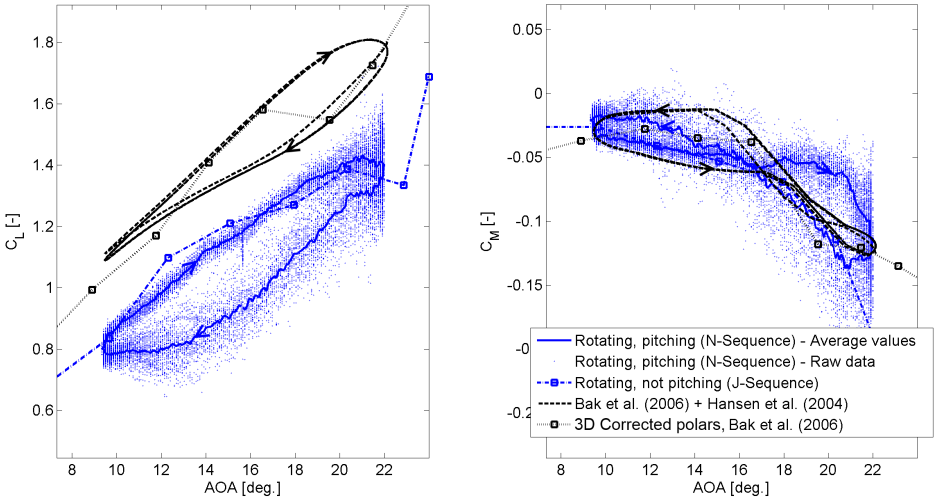

FIGURE 6.5: Case N47350: Lift and moment polars at $\alpha_M = 15.8°$, $\alpha_\Omega = 6.33°$, $r/R = 0.30$, $K = 0.143$.

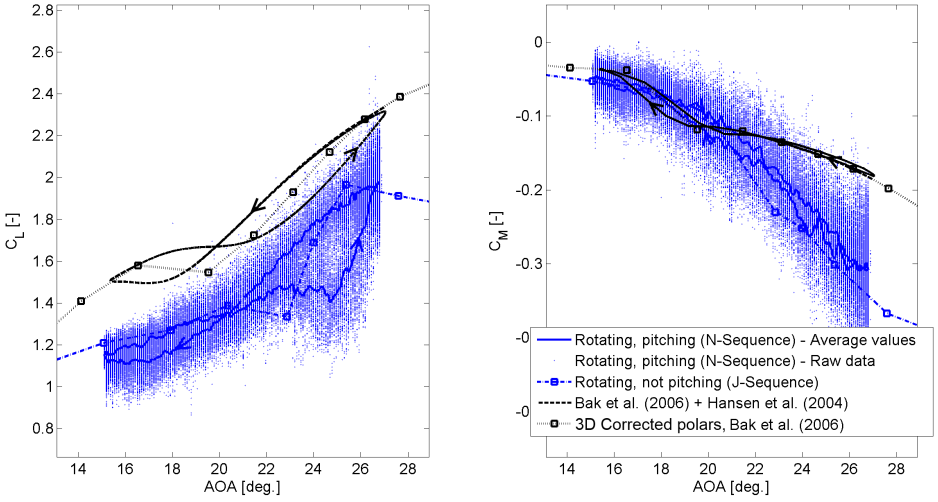

FIGURE 6.6: Case N47180: Lift and moment polars at $\alpha_M = 21.2°$, $\alpha_\Omega = 5.84°$, $r/R = 0.30$, $K = 0.036$.

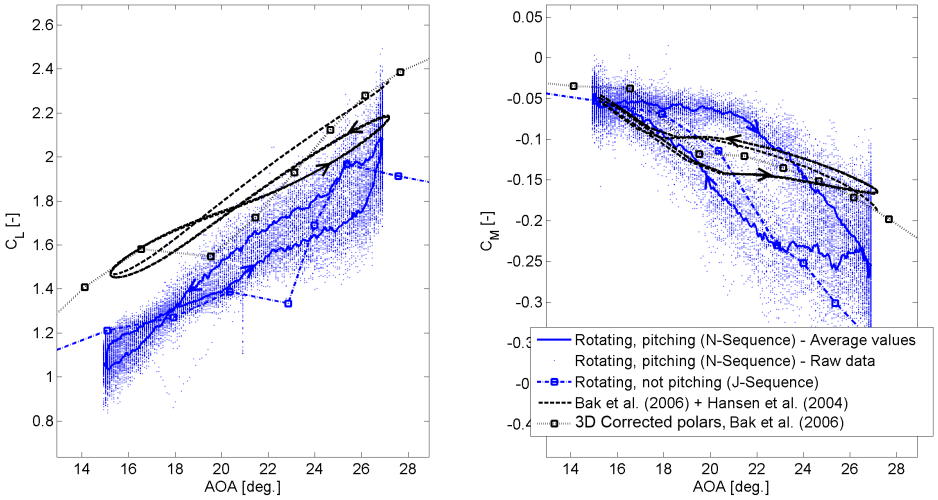

FIGURE 6.7: Case N47360: Lift and moment polars at $\alpha_M = 21.2°$, $\alpha_\Omega = 5.98°$, $r/R = 0.30$, $K = 0.143$.

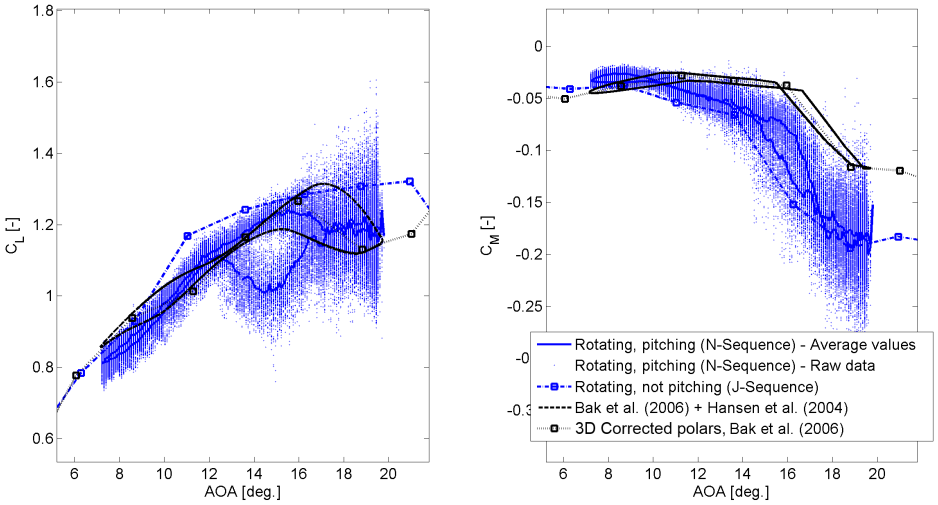

FIGURE 6.8: Case N47170: Lift and moment polars at $\alpha_M = 13.4°$, $\alpha_\Omega = 6.28°$, $r/R = 0.47$, $K = 0.025$.

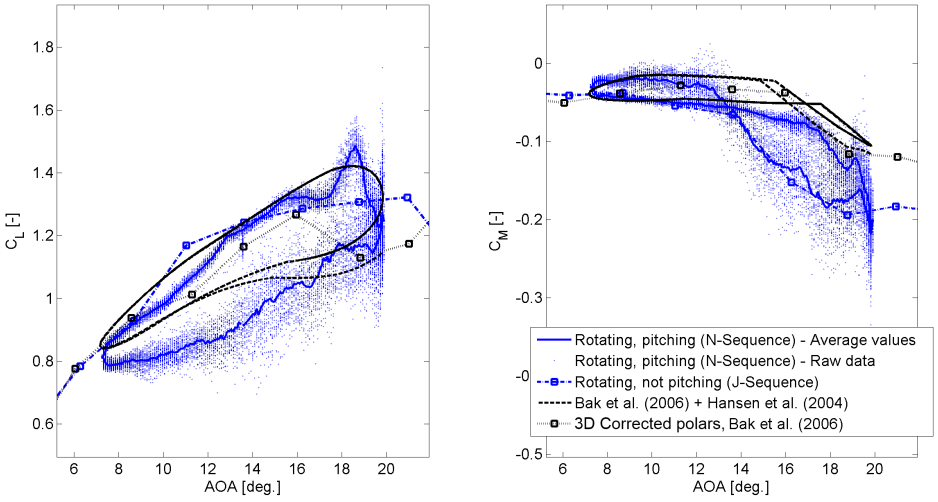

FIGURE 6.9: Case N47350: Lift and moment polars at $\alpha_M = 13.5°$, $\alpha_\Omega = 6.33°$, $r/R = 0.47$, $K = 0.1$.

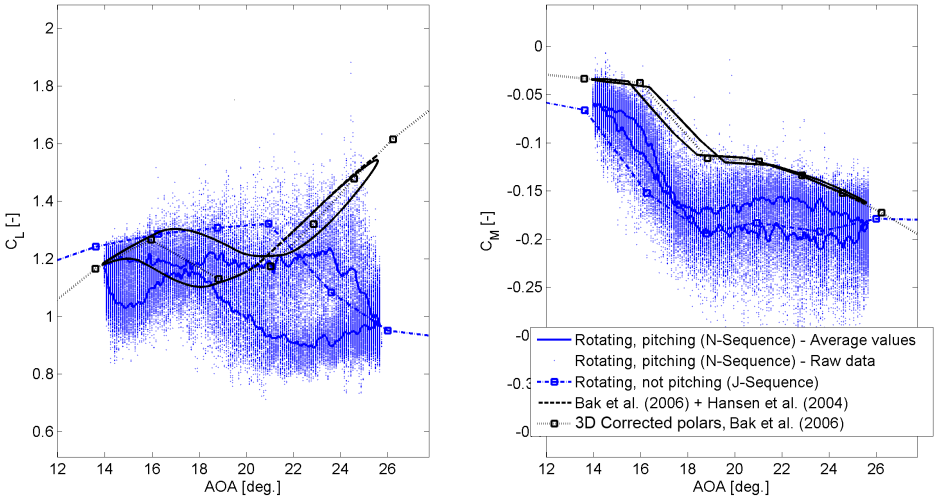

FIGURE 6.10: Case N47180: Lift and moment polars at $\alpha_M = 19.7°$, $\alpha_\Omega = 5.84°$, $r/R = 0.47$, $K = 0.025$.

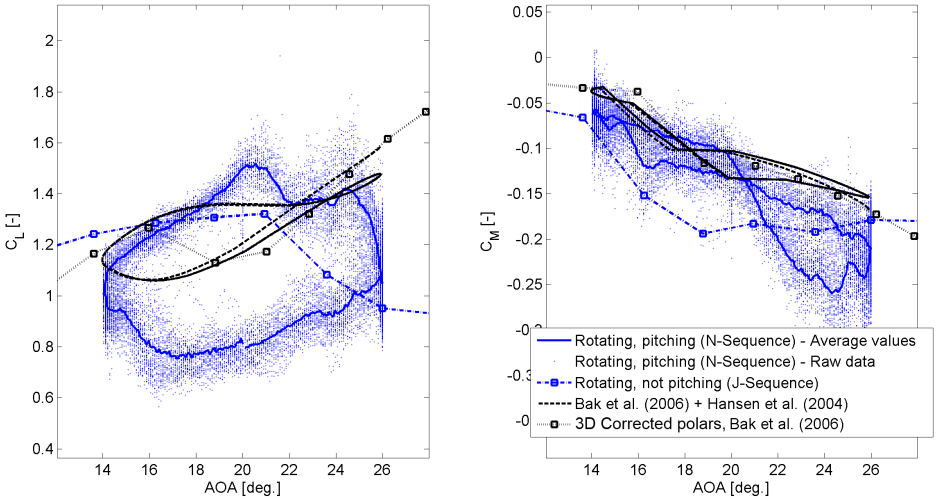

FIGURE 6.11: Case N47360: Lift and moment polars at $\alpha_M = 20.0°$, $\alpha_\Omega = 5.98°$, $r/R = 0.47$, $K = 0.1$.

Chapter 7

Conclusion

A study on rotational augmentation and dynamic stall has been carried out through a detailed analysis of a large database of experimental as well as computational data. The aim of this study has been to understand these two aerodynamic phenomenon from an engineering modelling perspective, for use with BEM-based aeroelastic codes.

Rotational augmentation was investigated with the help of a set of 3D full rotor CFD computations of the MEXICO rotor, 2D computations on the airfoil sections, and experimental data from the original experiment, and also the data from the NREL Phase VI experiment. The aim of this part of the study was to investigate the boundary layer development on the inboard part of the blade undergoing rotational augmentation in comparison with 2D flow conditions, and to identify features useful for modelling.

Several engineering models for rotational augmentation were analysed. Their behaviour relative to one another was consistent between MEXICO and NREL Phase VI rotor simulations. At high angles of attack there were large differences between some of the models and the experimental/CFD data. By comparing all the 3D corrected polars with the experimental/CFD data, the model by Bak et al. [29] was found to be the most reliable although not highly accurate.

It has been observed that in rotation there is a delay in the initiation of separation to a higher AOA, which means that for certain AOAs it is possible for separation to be suppressed completely. In addition, there is also a chord-wise postponement of the separation point location at a given AOA in rotating flow compared to a 2D case. In either case, it has been observed that the separated region of the boundary layer, measured in terms of its thickness above the surface of the airfoil, is suppressed in rotation. Furthermore, it has been observed that the effect of the centrifugal forces is present not only in the separated region, but everywhere along the chord. These forces

become dominant where the chord-wise velocities are small enough. That is, rotational augmentation (or stall-delay) can be present even when there is no separation visible on the rotating airfoil.

Effects of the tip and root vortices on the aerodynamics of those regions of the blades have been previously known. In the present study, it has been highlighted that similar effects can also arise in mid-board regions, wherever there is strong variation in the blade span-wise loading. Depending upon how strong the variation is, correction to these effects would have to be modelled in order to achieve accurate estimates of loads.

Finally, it is also observed that there are differences in the c_p distribution on a rotating airfoil undergoing separation compared to that on an airfoil in 2D flow at similar AOAs. It was found that beyond the separation point, the c_p distribution need not necessarily have a zero or a constant slope, suggesting that this procedure cannot be used to reliably locate the separation point on rotating airfoils.

Dynamic stall on rotating airfoils was investigated using the N sequence data set of the NREL Phase VI experiment. The dynamic stall was also modelled using unsteady DDES CFD simulations for some cases and also using an engineering model. The CFD simulations were carried out for 3 out of the 14 cases from the experimental database that were studied in this work. It was found that CFD data agreed well with the experimental data in two out of three cases simulated, and some differences were seen in the third.

All 14 cases for which experimental data was available were modelled with the computationally cheaper engineering model for dynamic stall. For investigating whether dynamic stall is qualitatively any different in 2D and 3D flows, the dynamic stall model by Hansen et al. [4] was implemented which used experimental (3D-corrected) polars instead of 2D data. The analysis showed that dynamic stall in rotating and non-rotating airfoils is similar, in the sense that the same model can be used to reliably capture dynamic stall in 2D as well as on rotation blades. This lead to conclude that in order to model a wind turbine effectively, dynamic stall must be modelled independently using a robust pre-processor for rotational augmentation, which becomes an add-on to the existing BEM based aeroelastic codes.

Motivated by the above conclusions, a brief case study was performed that simulated some of the unsteady N sequence cases from the NREL Phase VI experiment, using a simple BEM code coupled with the rotational augmentation model by Bak et al. and the dynamic stall model. The results showed that there are some limitations of the simple engineering model approach at higher angles of attack, and in the regions close to the blade root, but overall the results were promising.

7.1 Future work

It would be useful for the findings in this work regarding the rotational augmentation model by Bak et al. [29] and the dynamic stall model by Hansen et al. [4] to be applied to existing aeroelastic codes, simulate some test cases, and verify the results with either CFD or experimental data.

Since modelling the stochastic separated regions of rotating blades is still a challenge, rotational augmentation modelling relies heavily on empirical tuning based on observations from different experiments or CFD simulations. The analysis presented in this thesis could be extended to data from different rotors, for example see Zahle et al. [68] on the DTU 10MW reference turbine.

The Unsteady DDES CFD simulations presented in Chapter 5 showed good results in two out of the three N sequence cases simulated. It would be worthwhile to investigate its capabilities by simulating more cases, to assess whether this methodology can be used as benchmark data instead of expensive large scale experiments.

Hypothesis 1 described in Chapter 5 can be validated with the help of a combination of steady and unsteady computations simulating various unsteady conditions that are relevant for wind turbines. If this method of determining the effective AOA on wind turbine blades in unsteady conditions can be shown to work at several conditions, this method could become a useful tool for future analysis.

The effect of trailed vorticity discussed in Chapter 4 was shown to have a significant influence on the blade aerodynamics, which are not modelled in the classical BEM theory. Modelling this effect could improve the accuracy with which wind turbine aerodynamics are represented in BEM-based codes.

Appendix A

Complete N sequence dataset from the UAE Phase VI experiment

This appendix contains the complete set of data that was generated in the analysis presented in Chapter 5 on dynamic stall on wind turbine blades. Fourteen test N sequence cases from the NREL Phase VI experiment were analysed in total. Each of these cases contained the normal and tangential forces at five span-wise locations on the blade, resulting in a total of seventy dynamic stall cases. The experimental data from these cases are shown here, and Tables A.1 and A.2 contain information regarding the K values, mean AOAs and the pitching amplitude for each of these cases. Figures shown herein contain the raw and the averaged N sequence data, along with steady state data from the J sequence and 2D wind tunnel data at Re$= 7.5 \times 10^5$ from [2].

Case Nr.	$r/R = 0.30$	$r/R = 0.47$	$r/R = 0.63$	$r/R = 0.80$	$r/R = 0.95$
N47020	0.0897	0.0625	0.0439	0.0298	0.0207
N47030	0.0897	0.0625	0.0439	0.0298	0.0207
N47050	0.1076	0.0750	0.0526	0.0358	0.0248
N47090	0.1435	0.1000	0.0702	0.0477	0.0331
N47140	0.1793	0.1250	0.0877	0.0596	0.0413
N47150	0.1793	0.1250	0.0877	0.0596	0.0413
N47170	0.0359	0.0250	0.0175	0.0119	0.0083
N47180	0.0359	0.0250	0.0175	0.0119	0.0083
N47230	0.0717	0.0500	0.0351	0.0239	0.0165
N47240	0.0717	0.0500	0.0351	0.0239	0.0165
N47290	0.1076	0.0750	0.0526	0.0358	0.0248
N47300	0.1076	0.0750	0.0526	0.0358	0.0248
N47350	0.1435	0.1000	0.0702	0.0477	0.0331
N47360	0.1435	0.1000	0.0702	0.0477	0.0331

TABLE A.1: The reduced frequencies of pitching K for all cases shown in the figures in this appendix.

Case Nr.	α_M [°] $r/R = 0.30$	α_M [°] $r/R = 0.47$	α_M [°] $r/R = 0.63$	α_M [°] $r/R = 0.80$	α_M [°] $r/R = 0.95$	α_Ω [°]
N47020	4.5	2.0	-1.9	-5.8	-8.4	2.37
N47030	13.8	11.6	7.8	4.1	1.9	4.79
N47050	10.7	8.4	4.5	0.8	-1.5	2.50
N47090	10.6	8.3	4.4	0.7	-1.6	2.37
N47140	6.5	4.0	0.1	-3.7	-6.2	1.19
N47150	14.4	12.3	8.6	4.9	2.7	1.27
N47170	15.6	13.5	9.8	6.0	3.8	6.28
N47180	21.0	19.8	15.8	12.0	9.8	5.84
N47230	15.5	13.5	9.7	6.0	3.8	6.50
N47240	20.9	19.9	15.8	12.1	9.9	5.98
N47290	15.8	13.7	9.9	6.2	4.0	6.46
N47300	21.0	20.1	16.0	12.2	10.1	5.98
N47350	15.7	13.6	9.8	6.1	3.9	6.33
N47360	20.9	20.0	16.0	12.2	10.1	5.98

TABLE A.2: The mean AOA and the pitching amplitude for all cases shown in the figures in this appendix.

A.1 Radial location $r/R = 0.30$

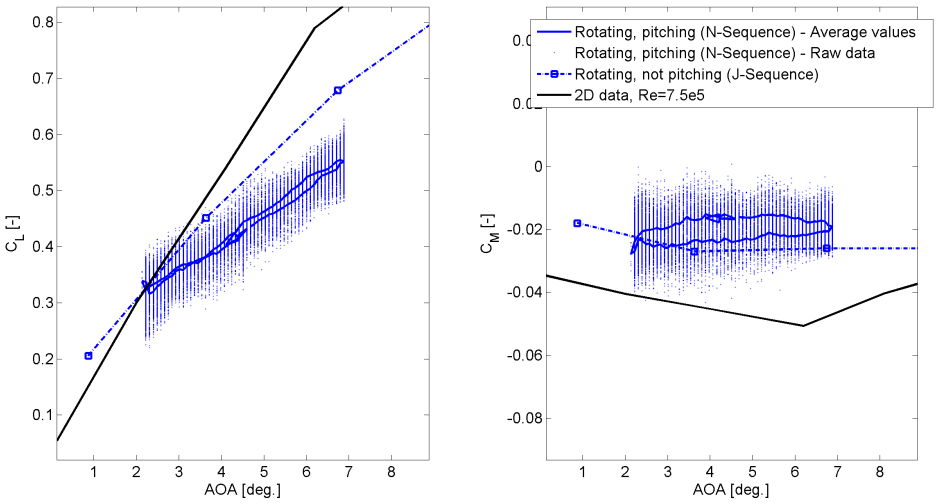

FIGURE A.1: Case N47030: Lift and moment polars at $\alpha_M = 13.9°$, $\alpha_\Omega = 4.79°$, $r/R = 0.30$, $K = 0.090$.

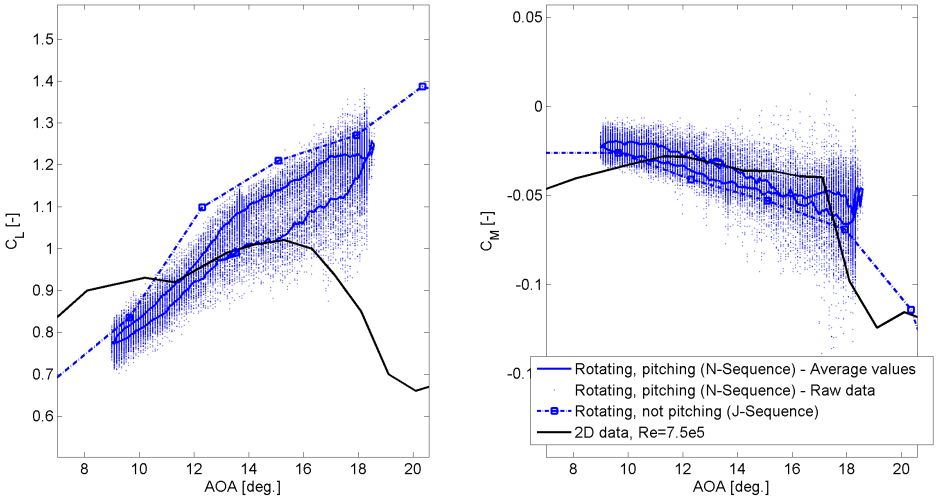

FIGURE A.2: Case N47030: Lift and moment polars at $\alpha_M = 13.9°$, $\alpha_\Omega = 4.79°$, $r/R = 0.30$, $K = 0.090$.

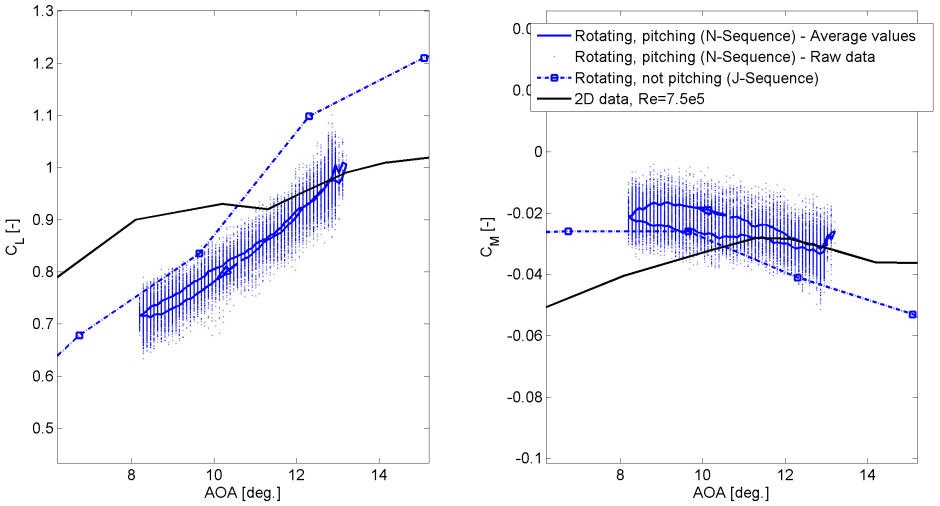

FIGURE A.3: Case N47050: Lift and moment polars at $\alpha_M = 10.7°$, $\alpha_\Omega = 2.50°$, $r/R = 0.30$, $K = 0.1076$.

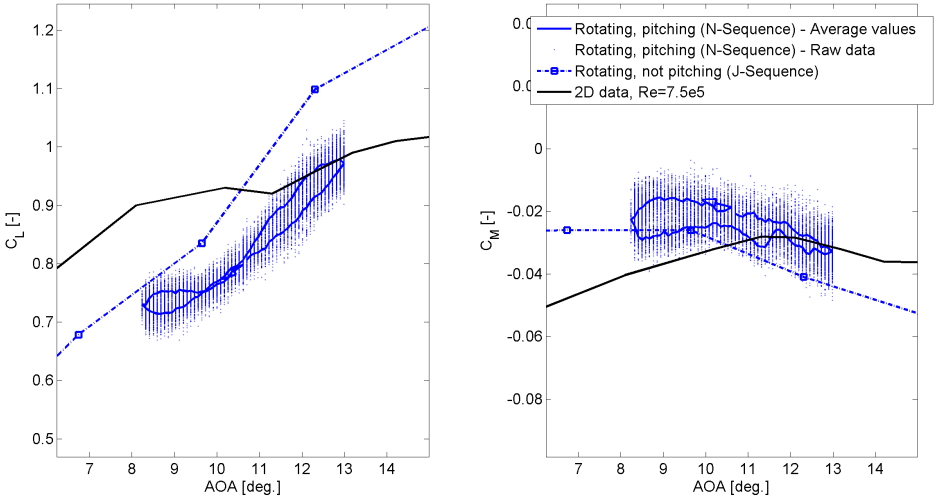

FIGURE A.4: Case N47090: Lift and moment polars at $\alpha_M = 10.6°$, $\alpha_\Omega = 2.37°$, $r/R = 0.30$, $K = 0.1434$.

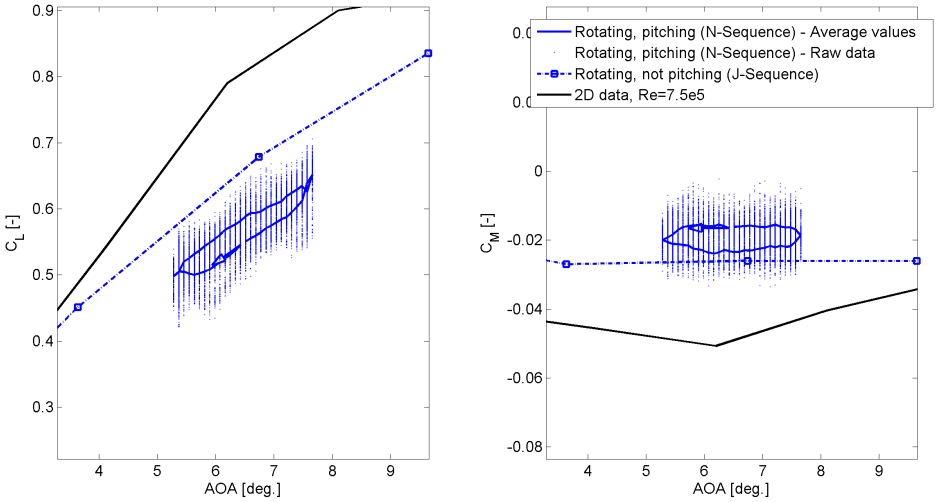

FIGURE A.5: Case N47140: Lift and moment polars at $\alpha_M = 6.5°$, $\alpha_\Omega = 1.19°$, $r/R = 0.30$, $K = 0.1793$.

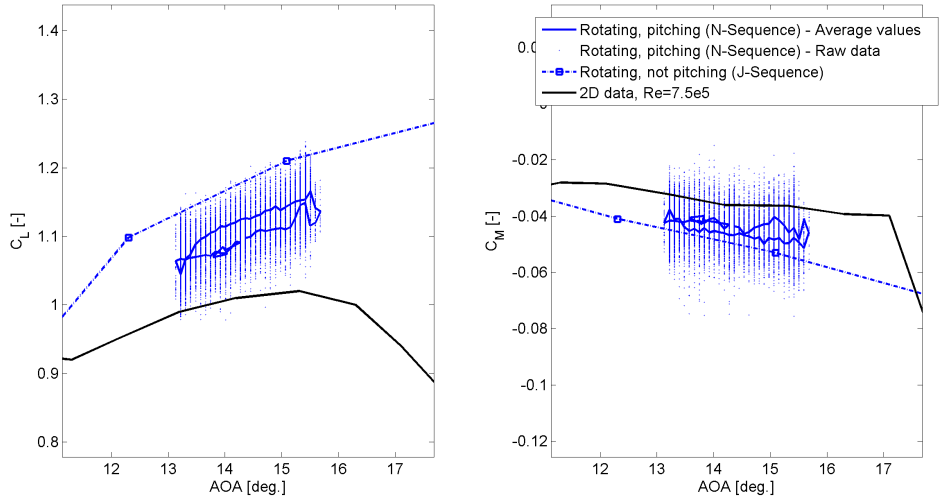

FIGURE A.6: Case N47150: Lift and moment polars at $\alpha_M = 14.4°$, $\alpha_\Omega = 1.27°$, $r/R = 0.30$, $K = 0.1793$.

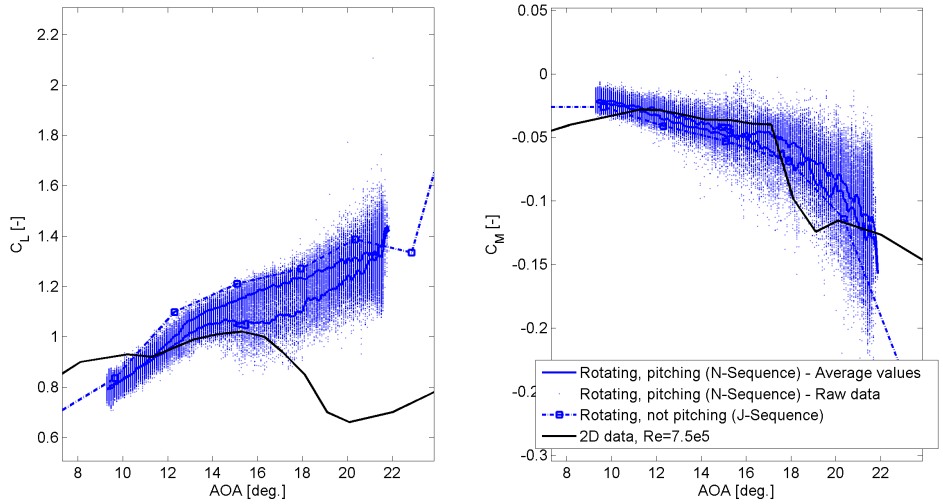

FIGURE A.7: Case N47170: Lift and moment polars at $\alpha_M = 15.6°$, $\alpha_\Omega = 6.28°$, $r/R = 0.30$, $K = 0.0359$.

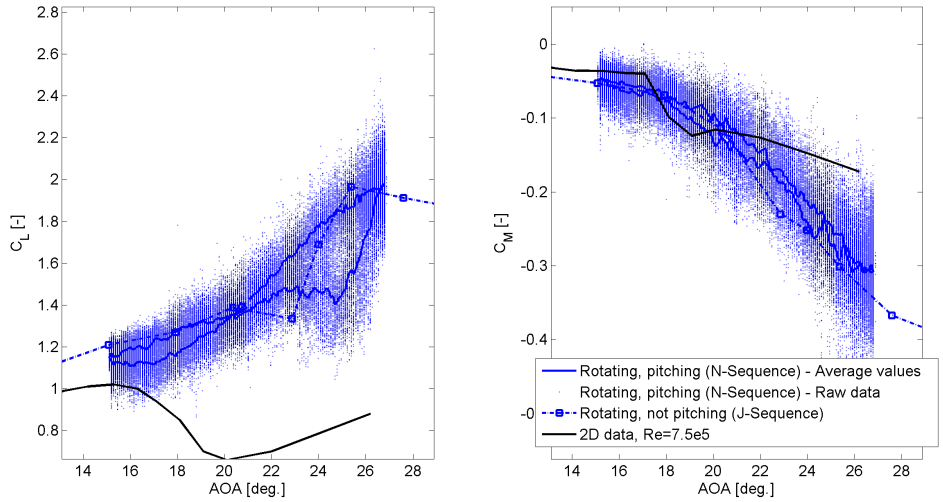

FIGURE A.8: Case N47180: Lift and moment polars at $\alpha_M = 21.0°$, $\alpha_\Omega = 5.84°$, $r/R = 0.30$, $K = 0.0359$.

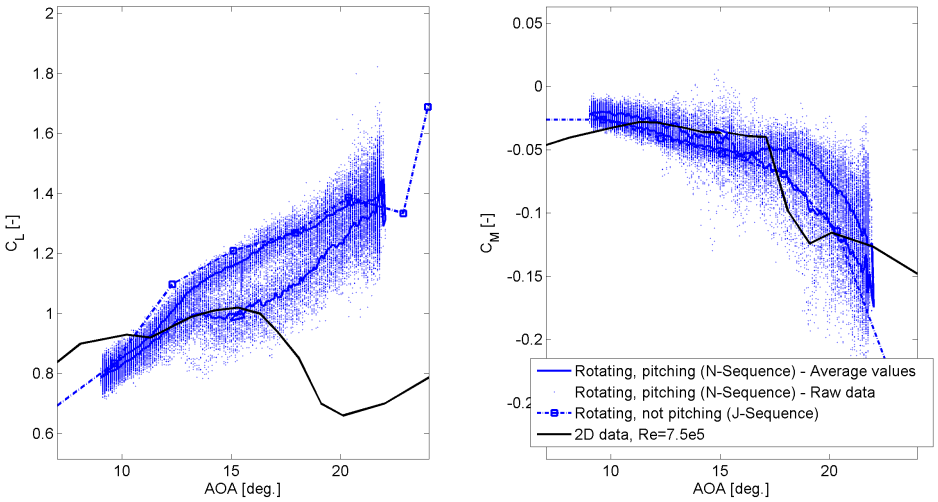

FIGURE A.9: Case N47230: Lift and moment polars at $\alpha_M = 15.5°$, $\alpha_\Omega = 6.50°$, $r/R = 0.30$, $K = 0.0717$.

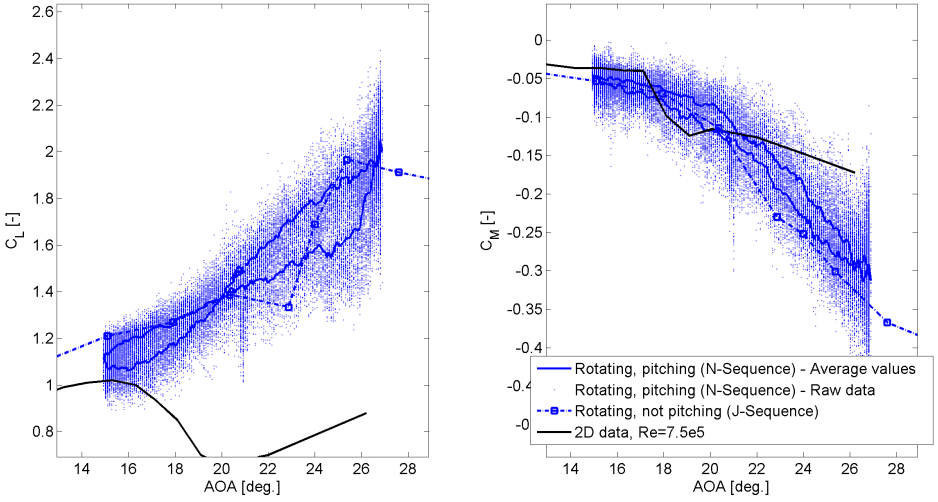

FIGURE A.10: Case N47240: Lift and moment polars at $\alpha_M = 20.9°$, $\alpha_\Omega = 5.98°$, $r/R = 0.30$, $K = 0.0717$.

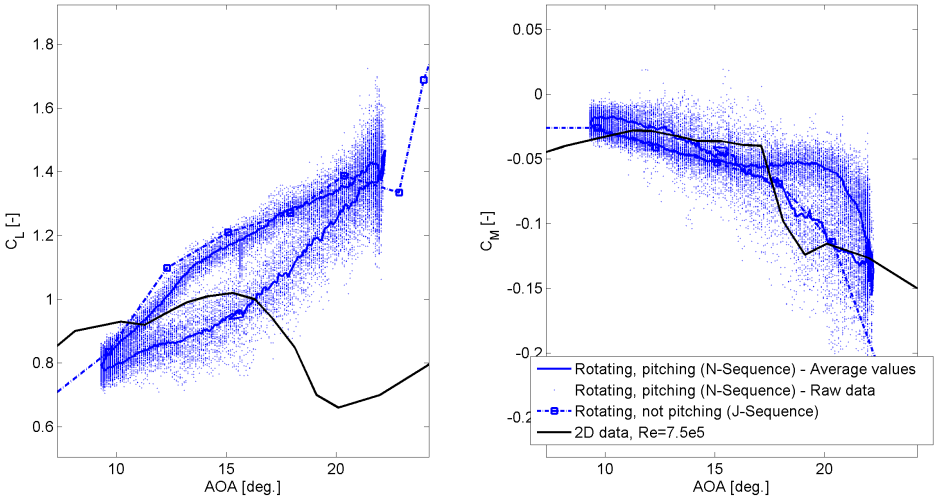

FIGURE A.11: Case N47290: Lift and moment polars at $\alpha_M = 15.8°$, $\alpha_\Omega = 6.46°$, $r/R = 0.30$, $K = 0.1076$.

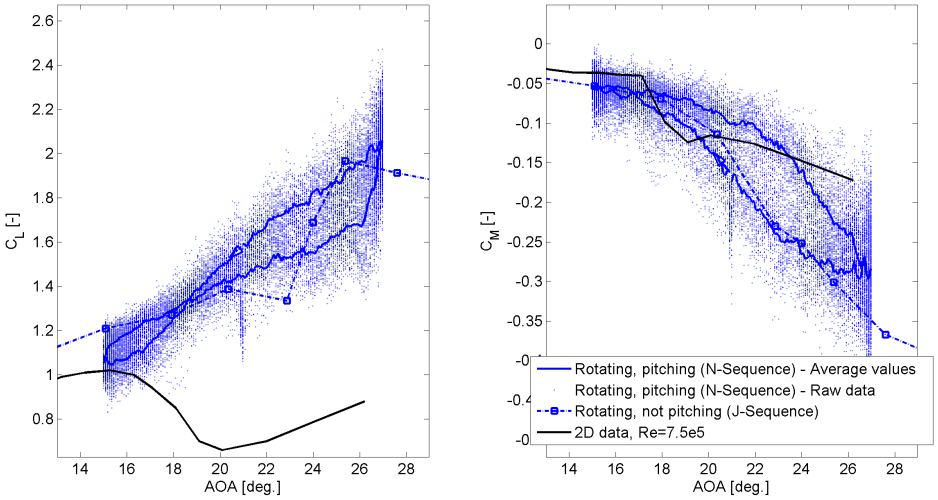

FIGURE A.12: Case N47300: Lift and moment polars at $\alpha_M = 21.0°$, $\alpha_\Omega = 5.98°$, $r/R = 0.30$, $K = 0.1076$.

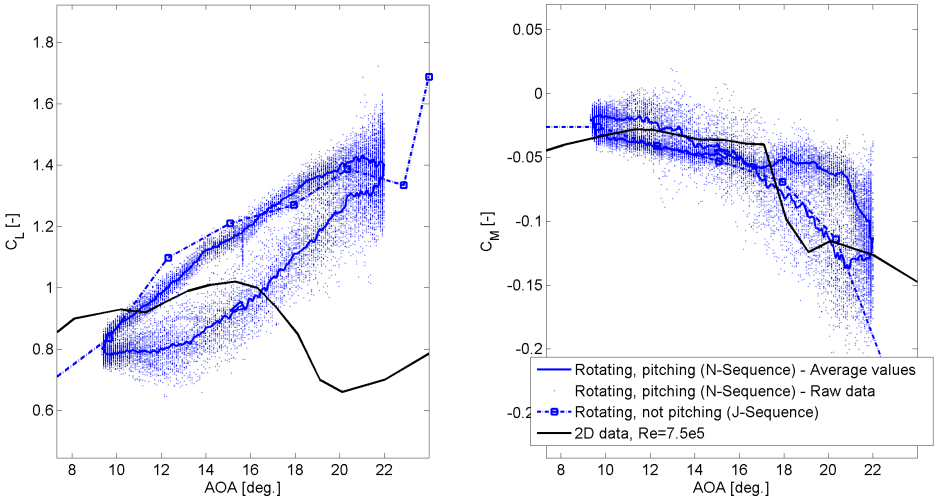

FIGURE A.13: Case N47350: Lift and moment polars at $\alpha_M = 15.7°$, $\alpha_\Omega = 6.33°$, $r/R = 0.30$, $K = 0.1434$.

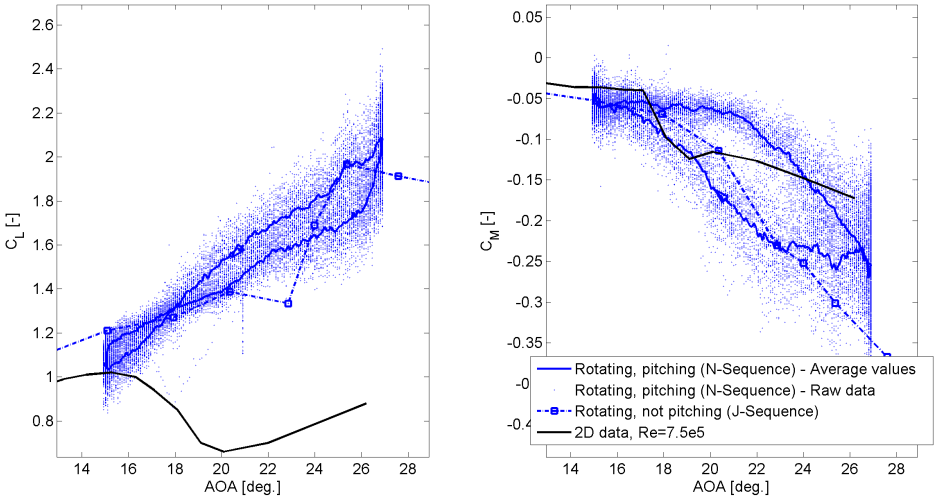

FIGURE A.14: Case N47360: Lift and moment polars at $\alpha_M = 20.9°$, $\alpha_\Omega = 5.98°$, $r/R = 0.30$, $K = 0.1434$.

A.2 Radial location $r/R = 0.47$

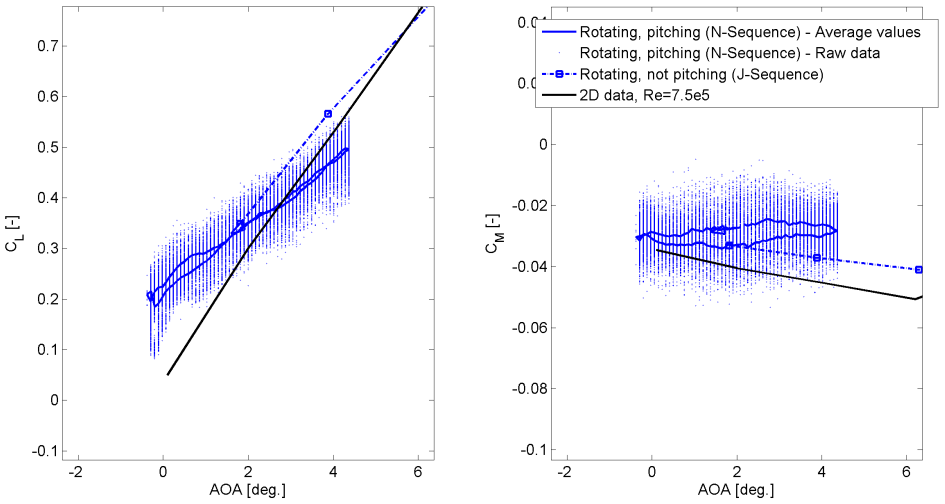

FIGURE A.15: Case N47020: Lift and moment polars at $\alpha_M = 2.0°$, $\alpha_\Omega = 2.37°$, $r/R = 0.47$, $K = 0.0625$.

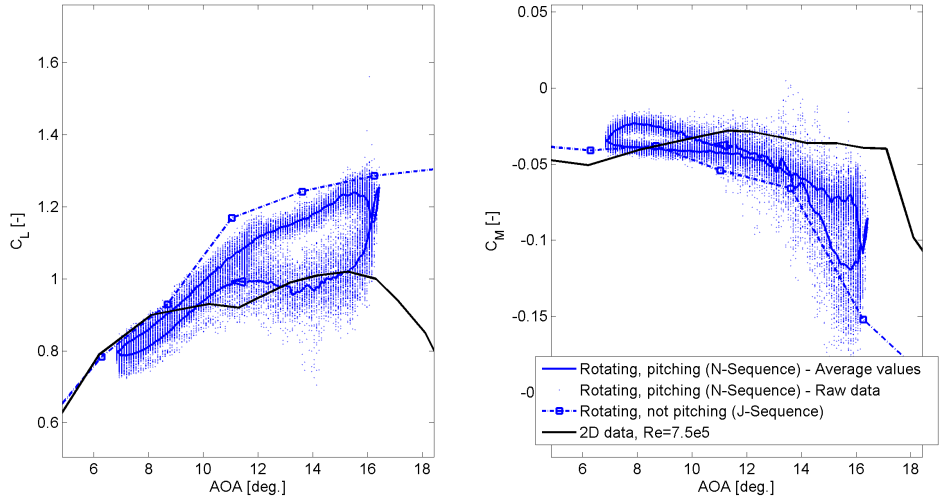

FIGURE A.16: Case N47030: Lift and moment polars at $\alpha_M = 11.6°$, $\alpha_\Omega = 4.79°$, $r/R = 0.47$, $K = 0.0625$.

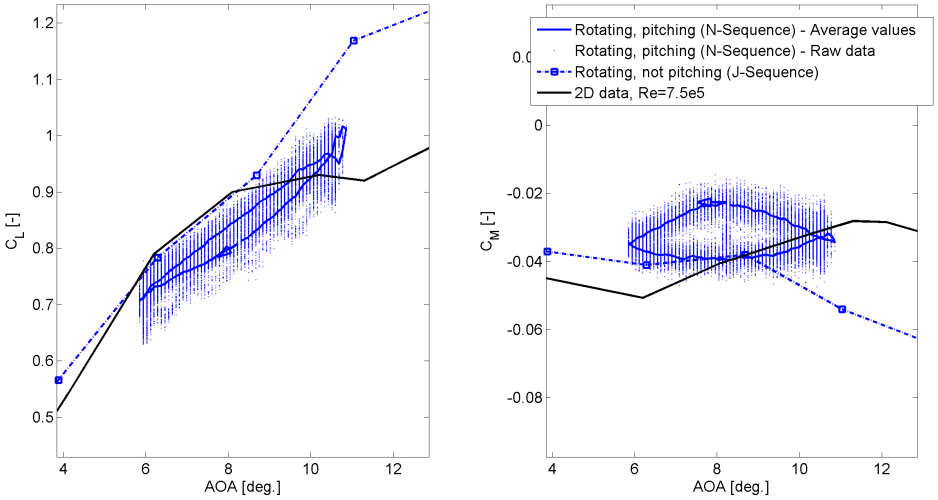

FIGURE A.17: Case N47050: Lift and moment polars at $\alpha_M = 8.4°$, $\alpha_\Omega = 2.50°$, $r/R = 0.47$, $K = 0.0750$.

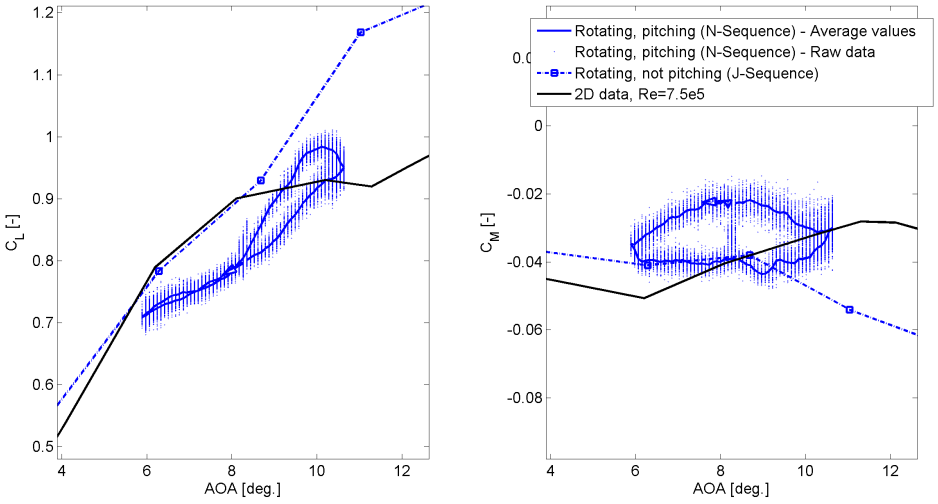

FIGURE A.18: Case N47090: Lift and moment polars at $\alpha_M = 8.3°$, $\alpha_\Omega = 2.37°$, $r/R = 0.47$, $K = 0.1000$.

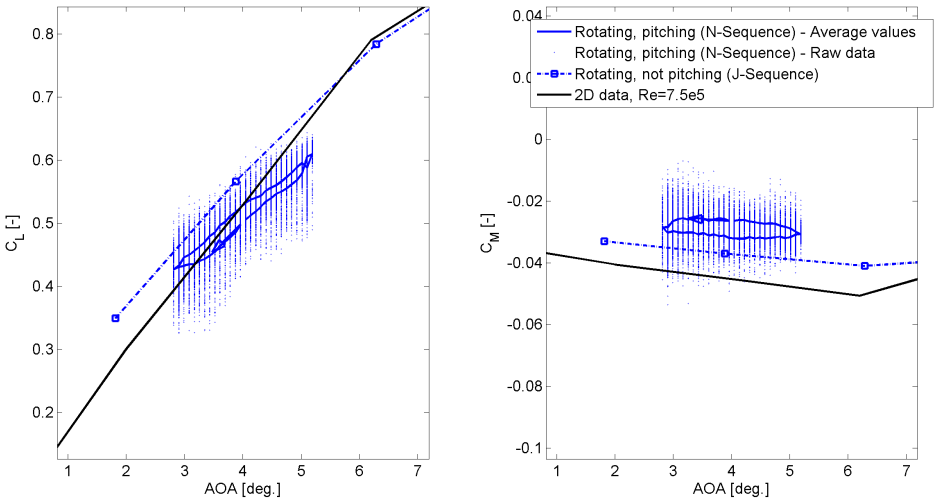

FIGURE A.19: Case N47140: Lift and moment polars at $\alpha_M = 4.0°$, $\alpha_\Omega = 1.19°$, $r/R = 0.47$, $K = 0.1250$.

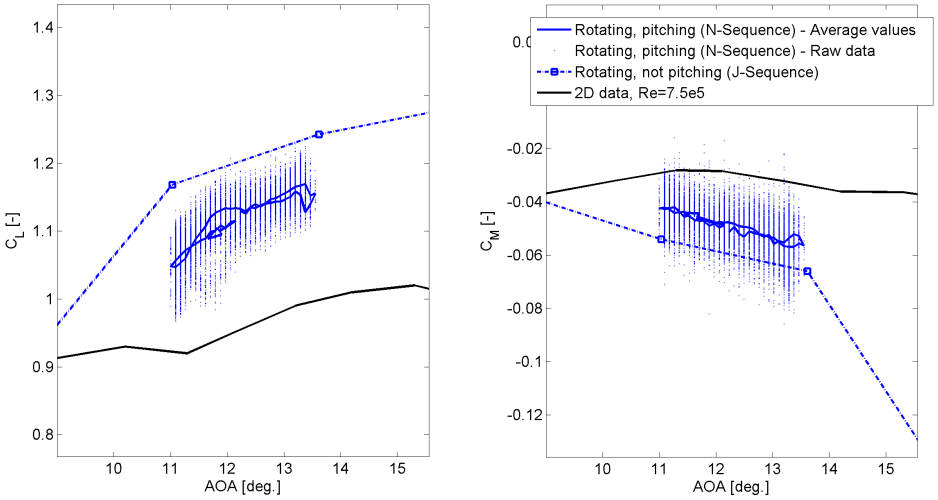

FIGURE A.20: Case N47150: Lift and moment polars at $\alpha_M = 12.3°$, $\alpha_\Omega = 1.27°$, $r/R = 0.47$, $K = 0.1250$.

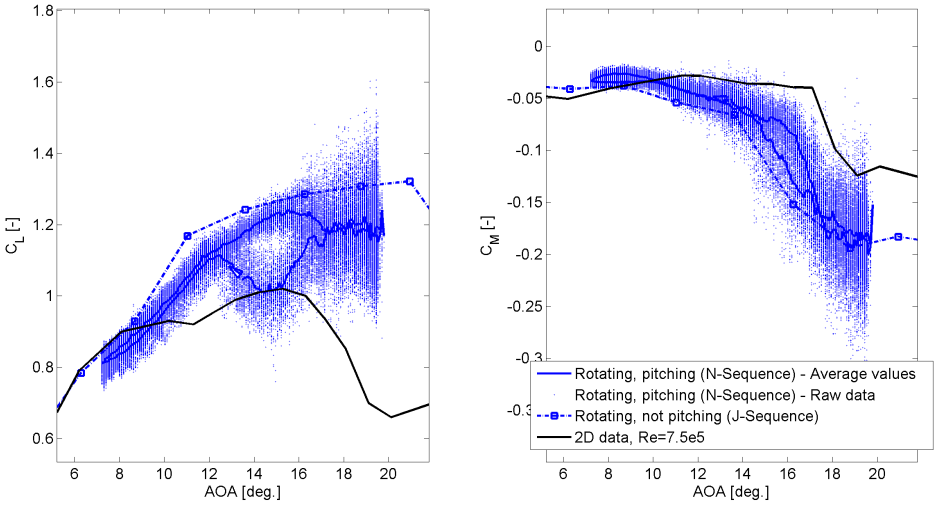

FIGURE A.21: Case N47170: Lift and moment polars at $\alpha_M = 13.5°$, $\alpha_\Omega = 6.28°$, $r/R = 0.47$, $K = 0.0250$.

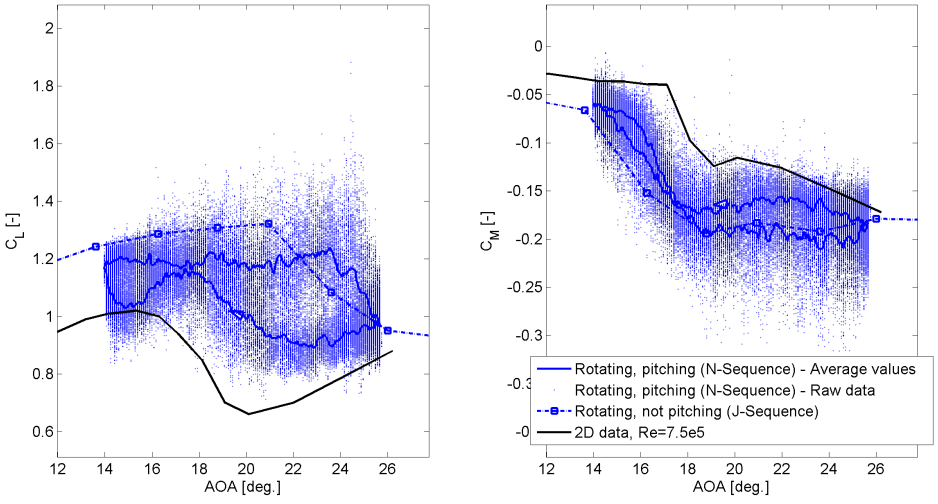

FIGURE A.22: Case N47180: Lift and moment polars at $\alpha_M = 19.8°$, $\alpha_\Omega = 5.84°$, $r/R = 0.47$, $K = 0.0250$.

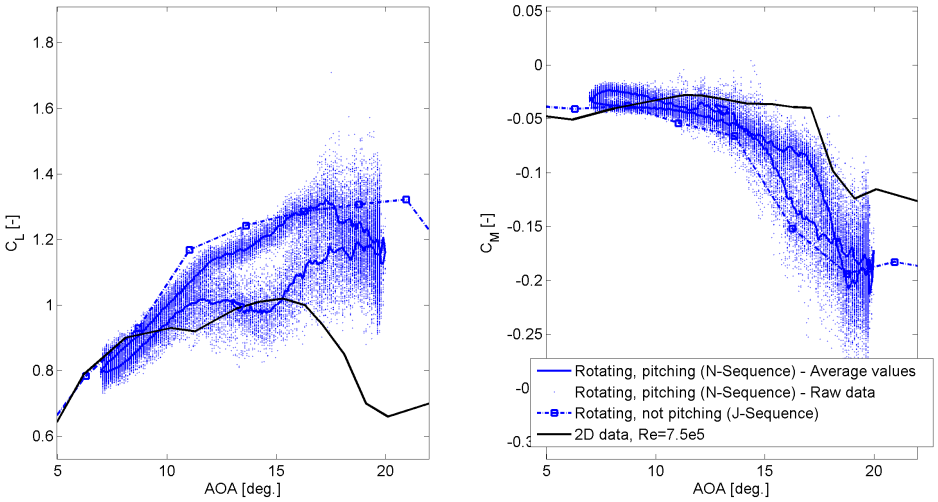

FIGURE A.23: Case N47230: Lift and moment polars at $\alpha_M = 13.5°$, $\alpha_\Omega = 6.50°$, $r/R = 0.47$, $K = 0.0500$.

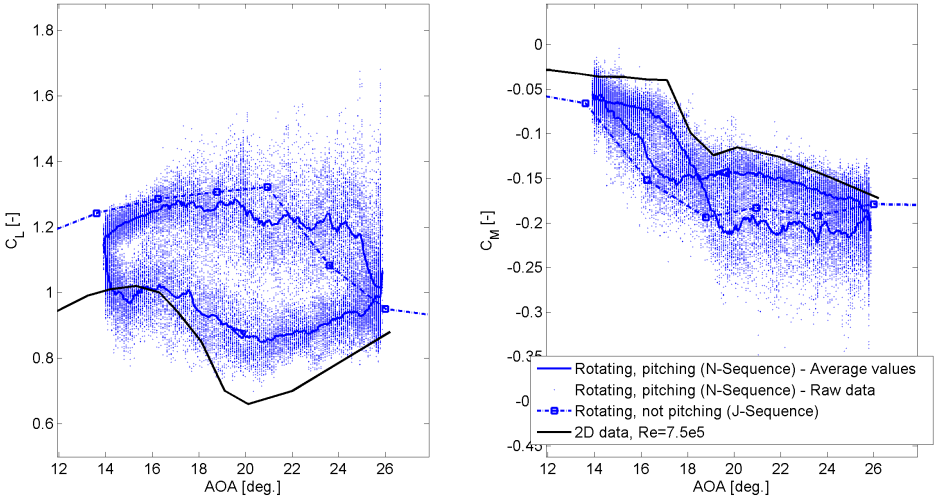

FIGURE A.24: Case N47240: Lift and moment polars at $\alpha_M = 19.9°$, $\alpha_\Omega = 5.98°$, $r/R = 0.47$, $K = 0.0500$.

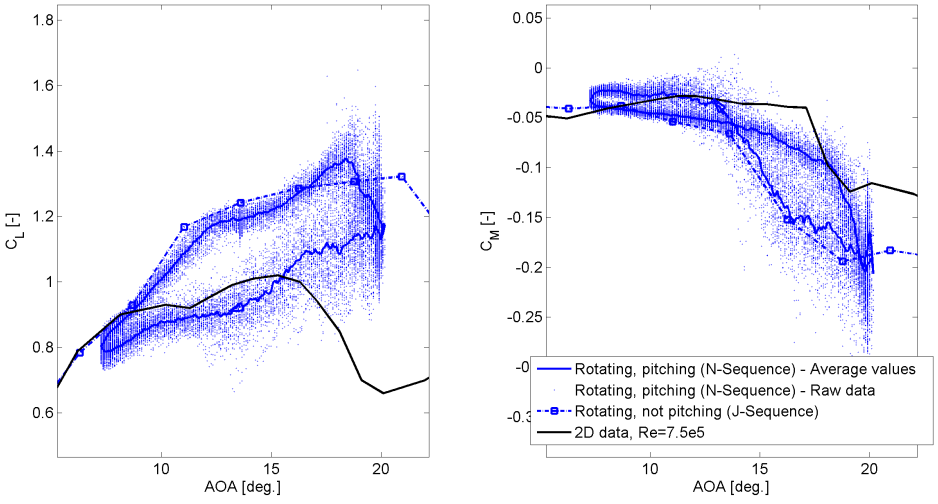

FIGURE A.25: Case N47290: Lift and moment polars at $\alpha_M = 13.7°$, $\alpha_\Omega = 6.46°$, $r/R = 0.47$, $K = 0.0750$.

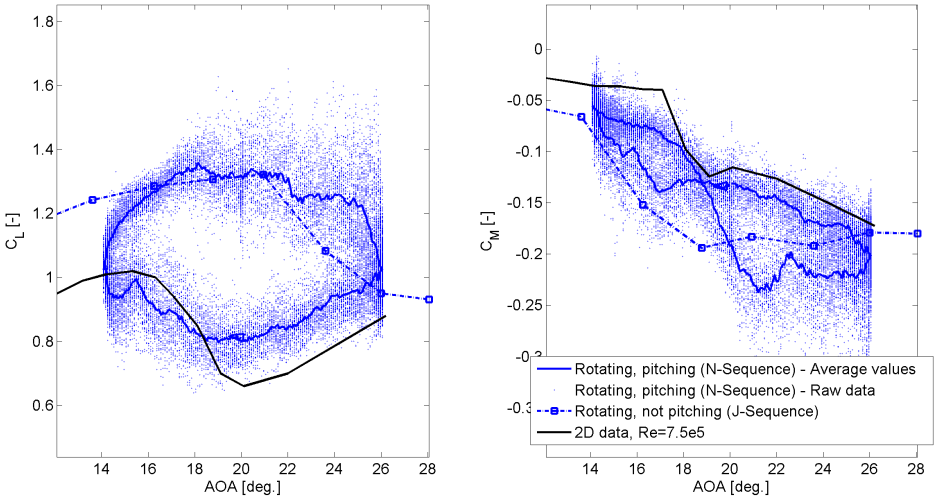

FIGURE A.26: Case N47300: Lift and moment polars at $\alpha_M = 20.1°$, $\alpha_\Omega = 5.98°$, $r/R = 0.47$, $K = 0.0750$.

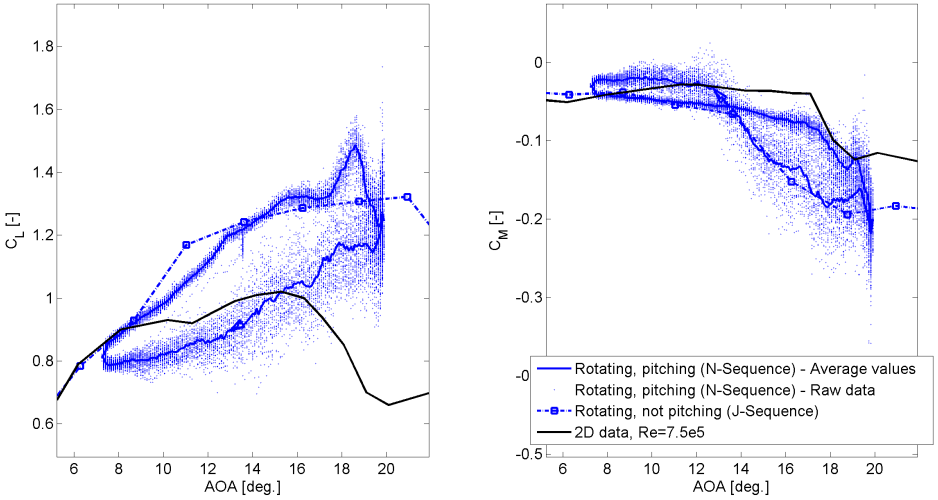

FIGURE A.27: Case N47350: Lift and moment polars at $\alpha_M = 13.6°$, $\alpha_\Omega = 6.33°$, $r/R = 0.47$, $K = 0.1000$.

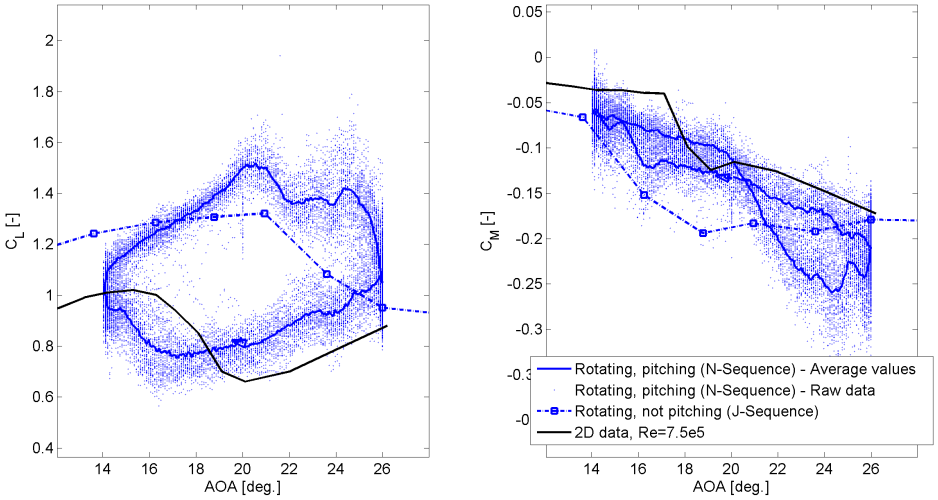

FIGURE A.28: Case N47360: Lift and moment polars at $\alpha_M = 20.0°$, $\alpha_\Omega = 5.98°$, $r/R = 0.47$, $K = 0.1000$.

A.3 Radial location $r/R = 0.63$

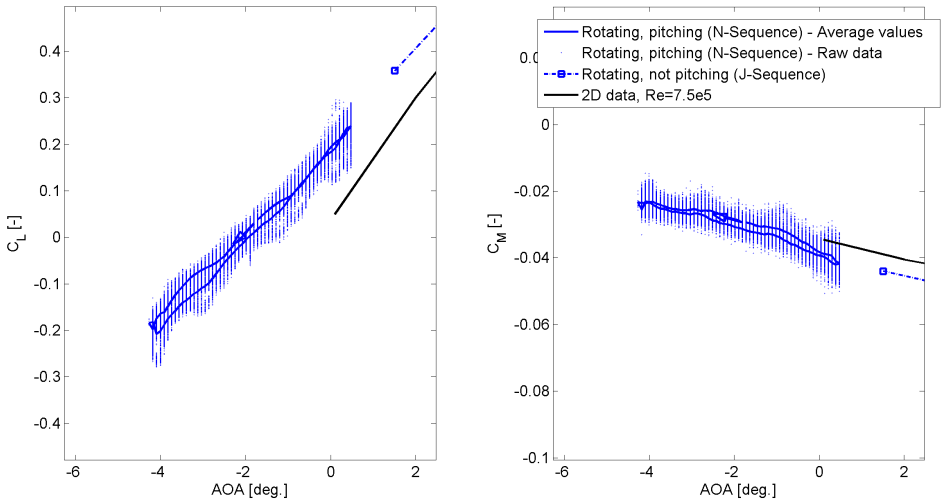

FIGURE A.29: Case N47020: Lift and moment polars at $\alpha_M = -1.9°$, $\alpha_\Omega = 2.37°$, $r/R = 0.63$, $K = 0.0439$.

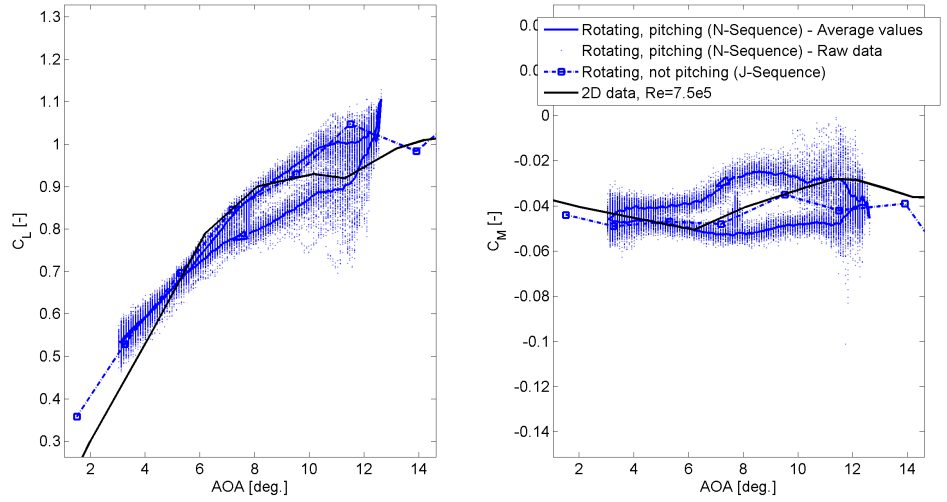

FIGURE A.30: Case N47030: Lift and moment polars at $\alpha_M = 7.8°$, $\alpha_\Omega = 4.79°$, $r/R = 0.63$, $K = 0.0439$.

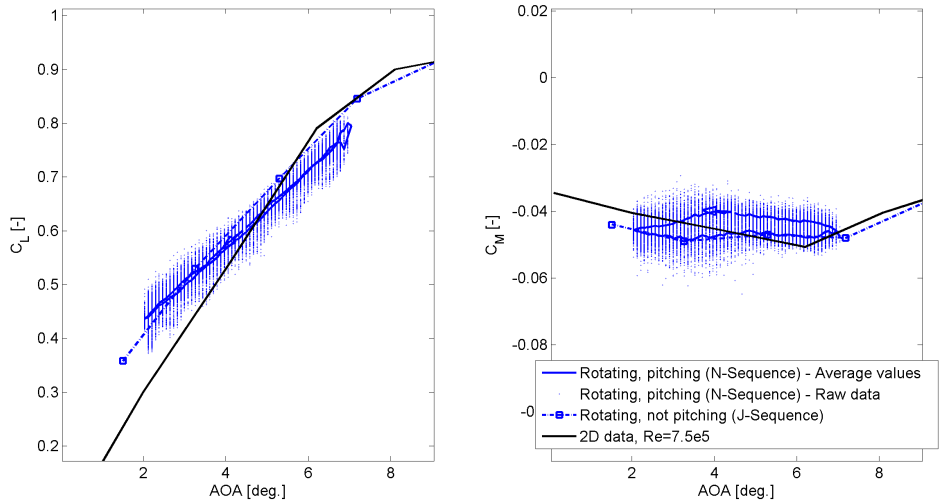

FIGURE A.31: Case N47050: Lift and moment polars at $\alpha_M = 4.5°$, $\alpha_\Omega = 2.50°$, $r/R = 0.63$, $K = 0.0526$.

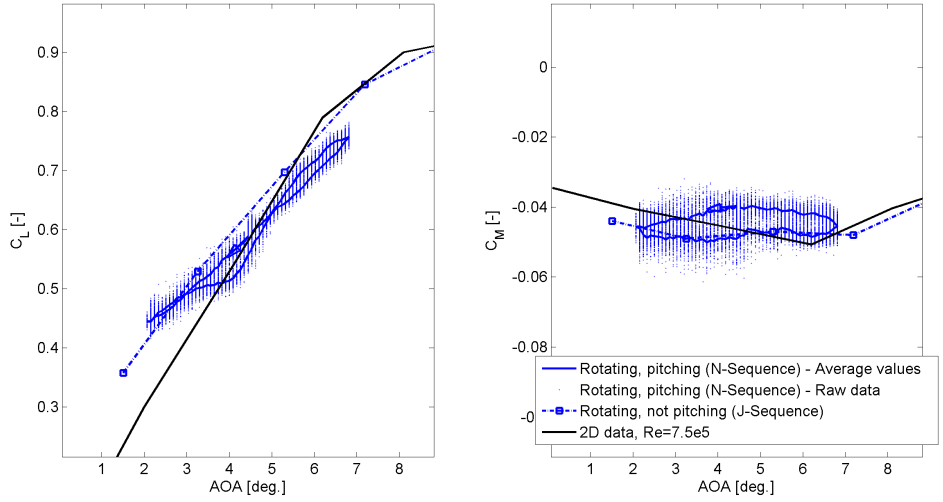

FIGURE A.32: Case N47090: Lift and moment polars at $\alpha_M = 4.4°$, $\alpha_\Omega = 2.37°$, $r/R = 0.63$, $K = 0.0702$.

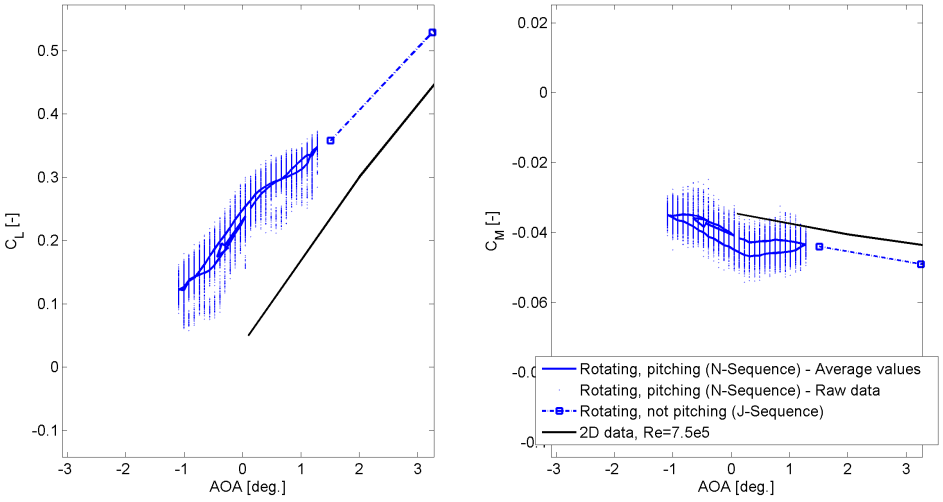

FIGURE A.33: Case N47140: Lift and moment polars at $\alpha_M = 0.1°$, $\alpha_\Omega = 1.19°$, $r/R = 0.63$, $K = 0.0877$.

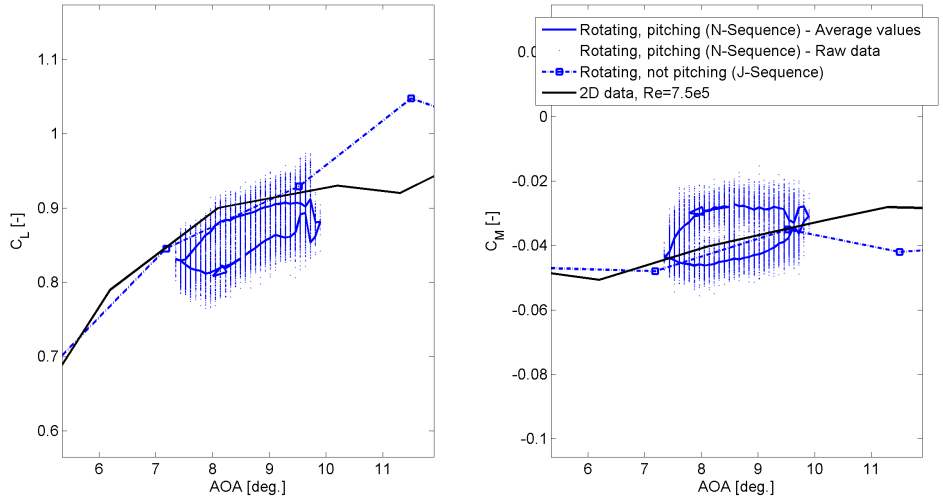

FIGURE A.34: Case N47150: Lift and moment polars at $\alpha_M = 8.6°$, $\alpha_\Omega = 1.27°$, $r/R = 0.63$, $K = 0.0877$.

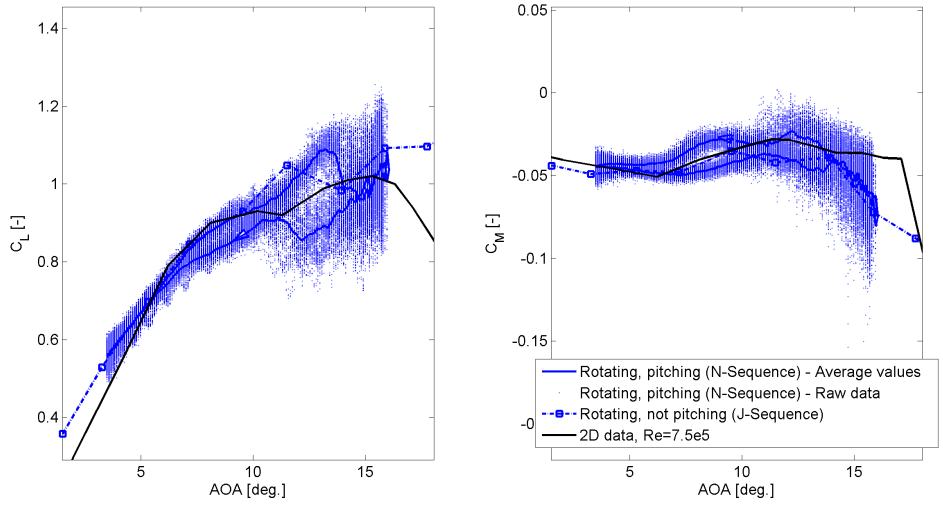

FIGURE A.35: Case N47170: Lift and moment polars at $\alpha_M = 9.8°$, $\alpha_\Omega = 6.28°$, $r/R = 0.63$, $K = 0.0175$.

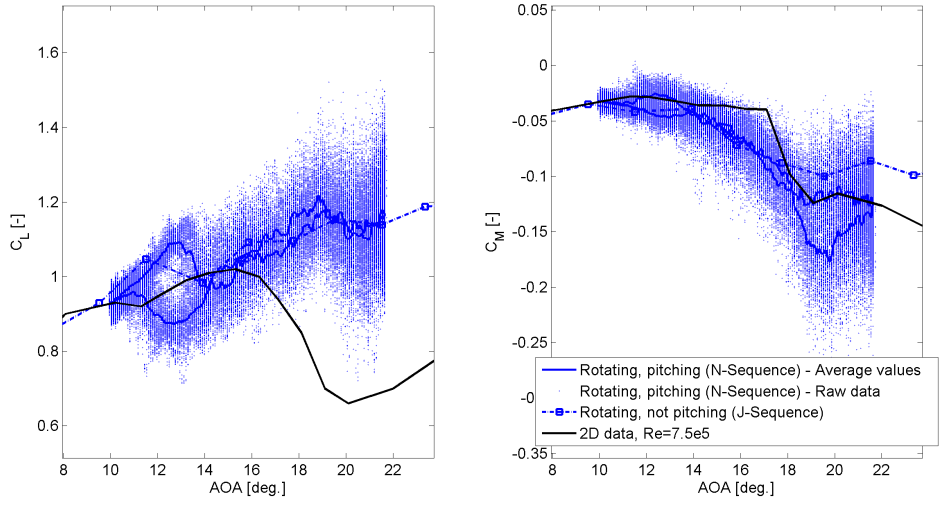

FIGURE A.36: Case N47180: Lift and moment polars at $\alpha_M = 15.8°$, $\alpha_\Omega = 5.84°$, $r/R = 0.63$, $K = 0.0175$.

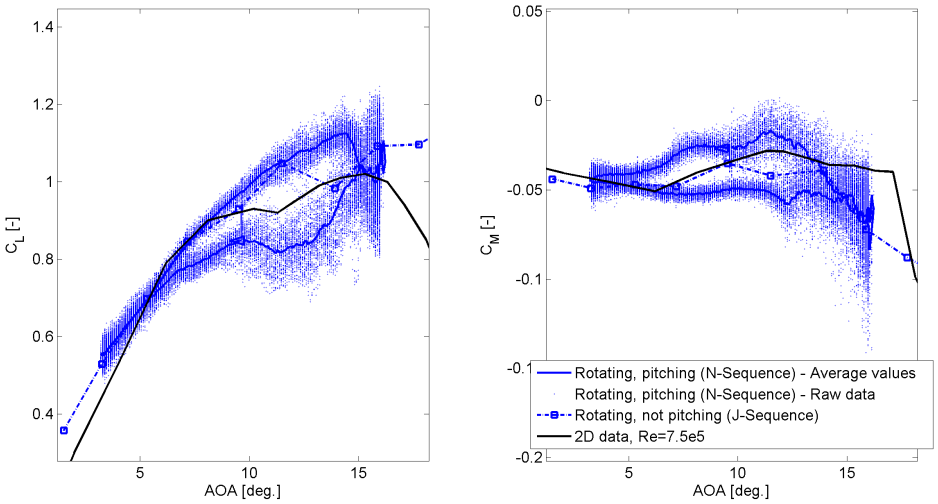

FIGURE A.37: Case N47230: Lift and moment polars at $\alpha_M = 9.7°$, $\alpha_\Omega = 6.50°$, $r/R = 0.63$, $K = 0.0351$.

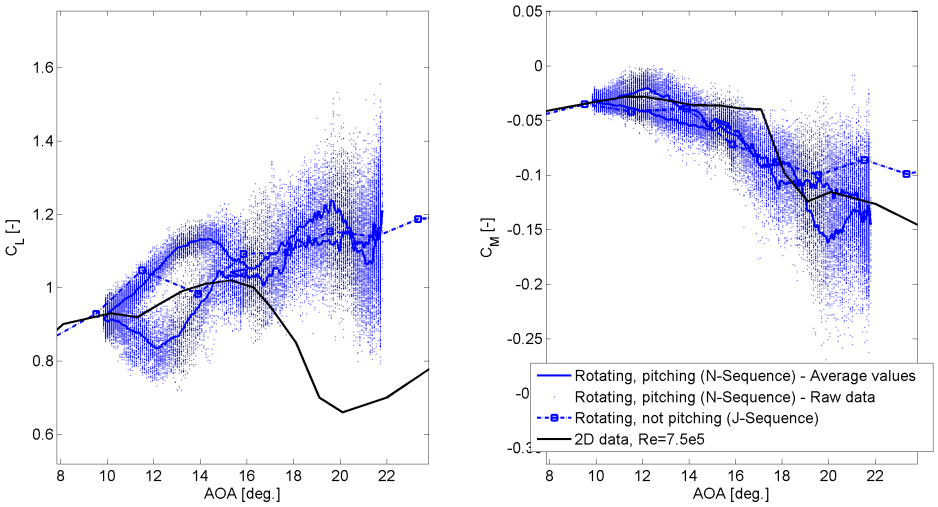

FIGURE A.38: Case N47240: Lift and moment polars at $\alpha_M = 15.8°$, $\alpha_\Omega = 5.98°$, $r/R = 0.63$, $K = 0.0351$.

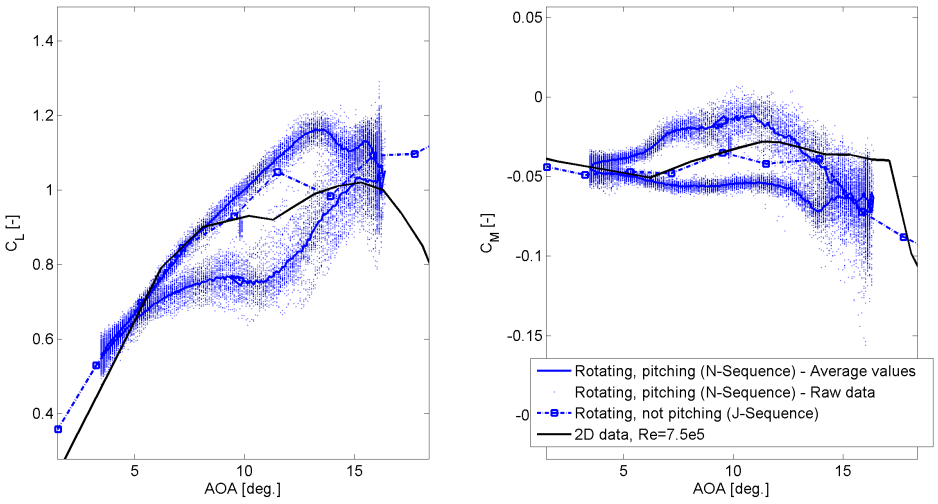

FIGURE A.39: Case N47290: Lift and moment polars at $\alpha_M = 9.9°$, $\alpha_\Omega = 6.46°$, $r/R = 0.63$, $K = 0.0526$.

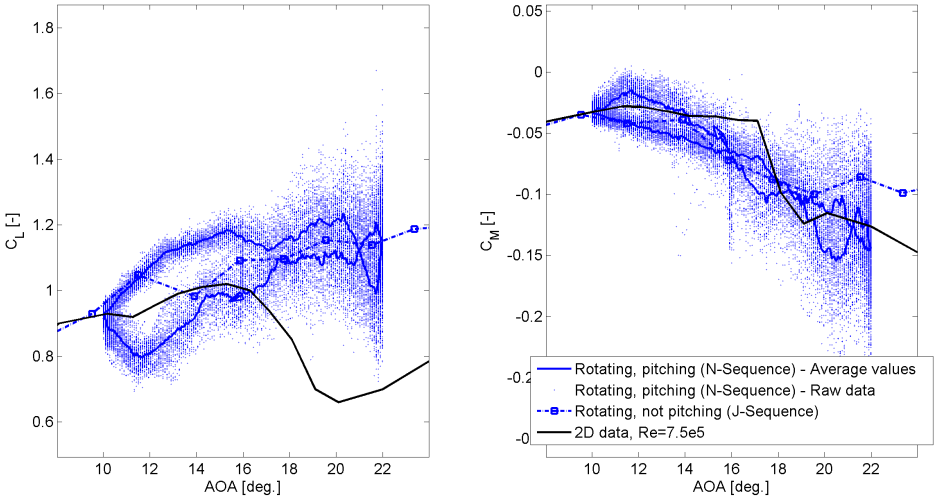

FIGURE A.40: Case N47300: Lift and moment polars at $\alpha_M = 16.0°$, $\alpha_\Omega = 5.98°$, $r/R = 0.63$, $K = 0.0526$.

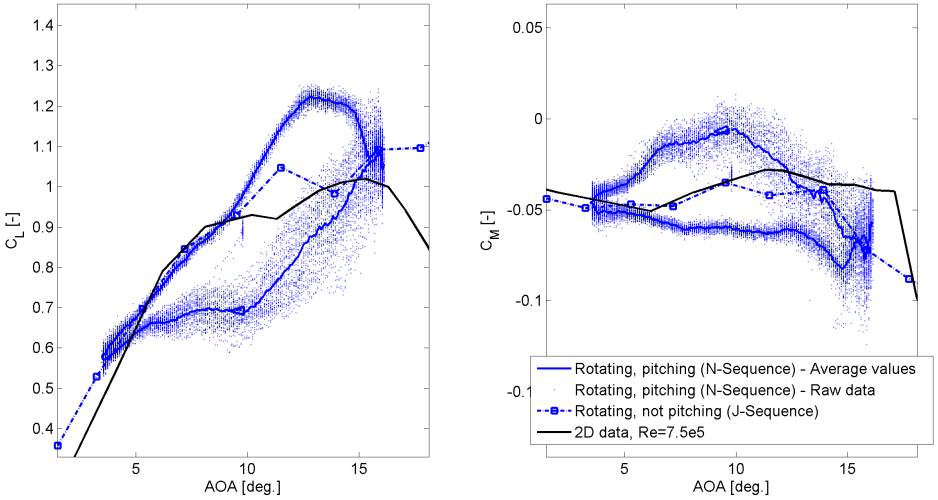

FIGURE A.41: Case N47350: Lift and moment polars at $\alpha_M = 9.8°$, $\alpha_\Omega = 6.33°$, $r/R = 0.63$, $K = 0.0702$.

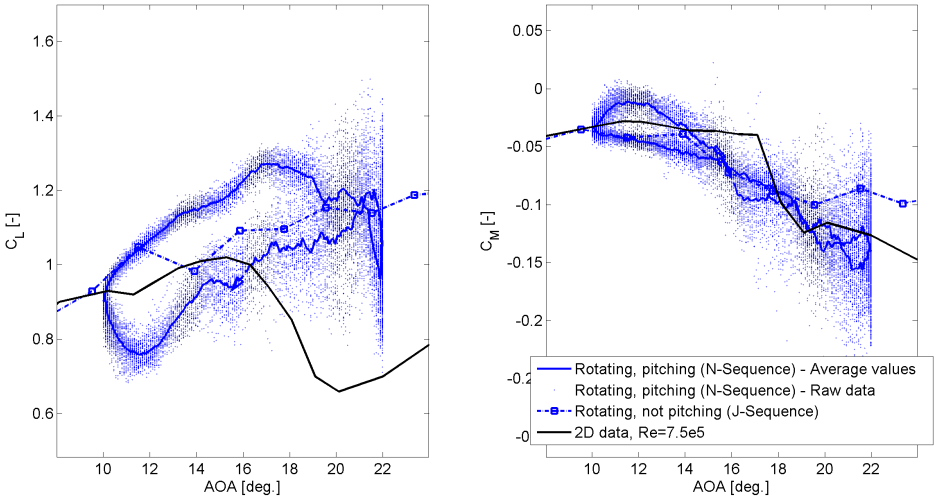

FIGURE A.42: Case N47360: Lift and moment polars at $\alpha_M = 16.0°$, $\alpha_\Omega = 5.98°$, $r/R = 0.63$, $K = 0.0702$.

A.4 Radial location $r/R = 0.80$

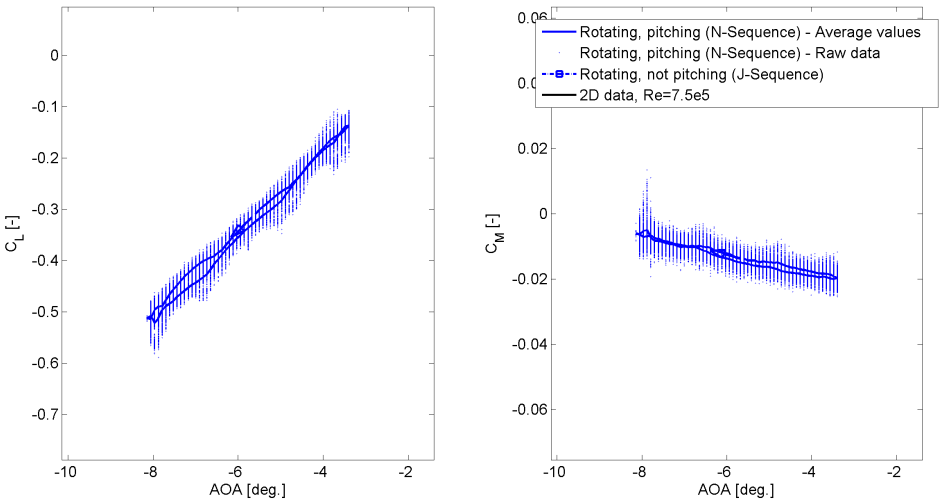

FIGURE A.43: Case N47020: Lift and moment polars at $\alpha_M = -5.8°$, $\alpha_\Omega = 2.37°$, $r/R = 0.80$, $K = 0.0298$.

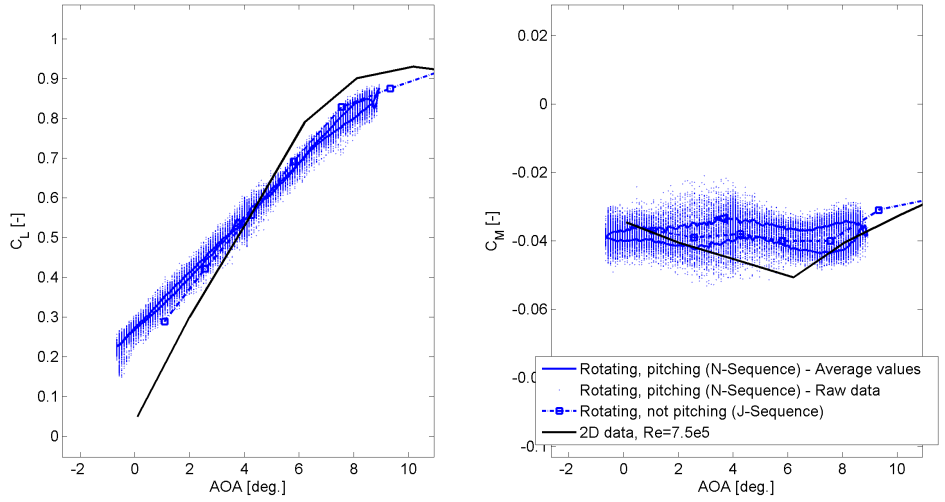

FIGURE A.44: Case N47030: Lift and moment polars at $\alpha_M = 4.1°$, $\alpha_\Omega = 4.79°$, $r/R = 0.80$, $K = 0.0298$.

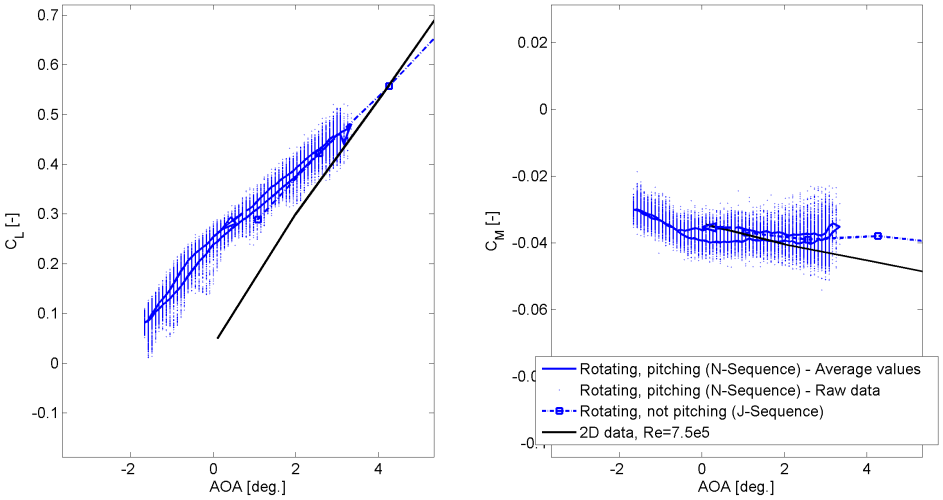

FIGURE A.45: Case N47050: Lift and moment polars at $\alpha_M = 0.8°$, $\alpha_\Omega = 2.50°$, $r/R = 0.80$, $K = 0.0358$.

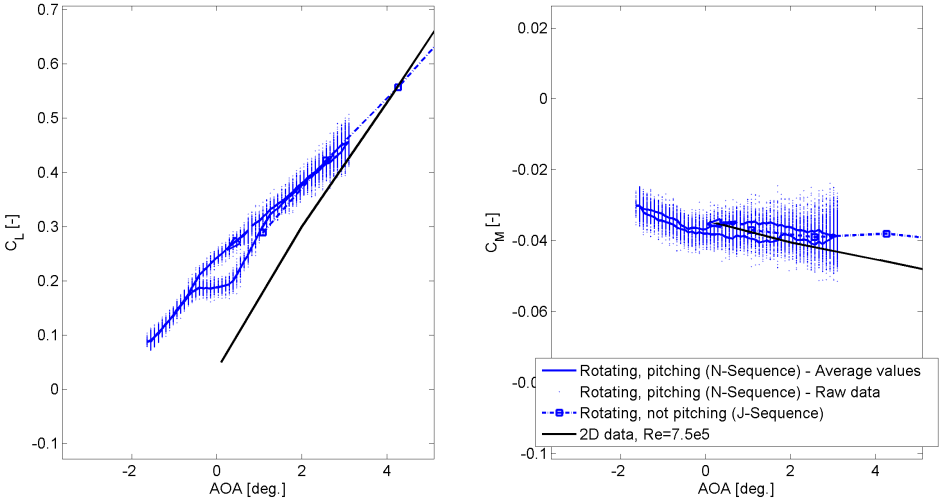

FIGURE A.46: Case N47090: Lift and moment polars at $\alpha_M = 0.7°$, $\alpha_\Omega = 2.37°$, $r/R = 0.80$, $K = 0.0477$.

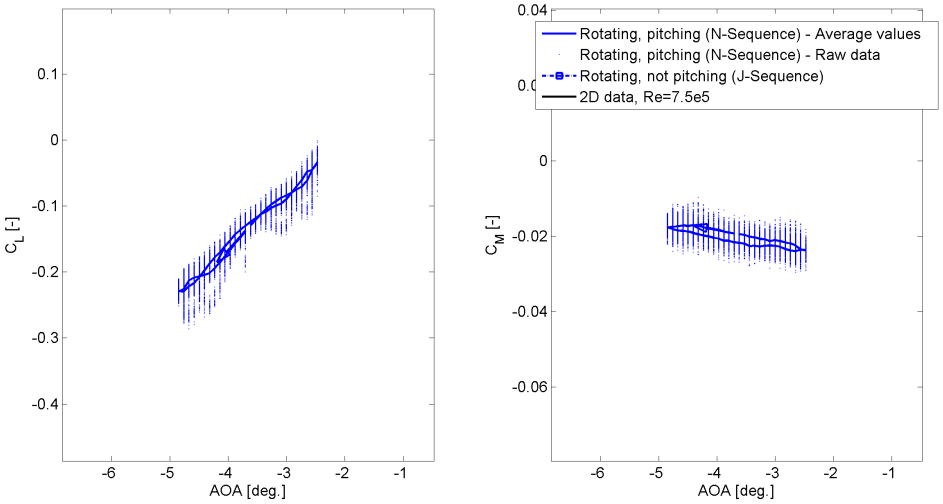

FIGURE A.47: Case N47140: Lift and moment polars at $\alpha_M = -3.7°$, $\alpha_\Omega = 1.19°$, $r/R = 0.80$, $K = 0.0596$.

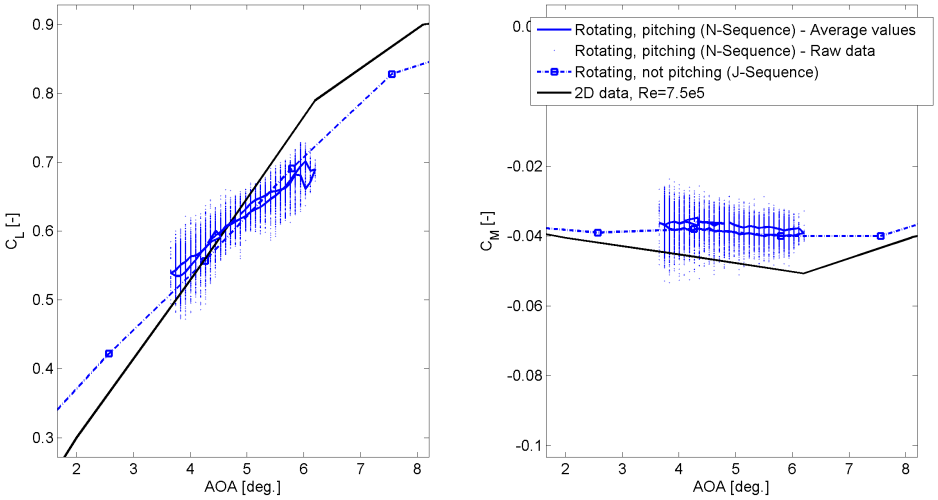

FIGURE A.48: Case N47150: Lift and moment polars at $\alpha_M = 4.9°$, $\alpha_\Omega = 1.27°$, $r/R = 0.80$, $K = 0.0596$.

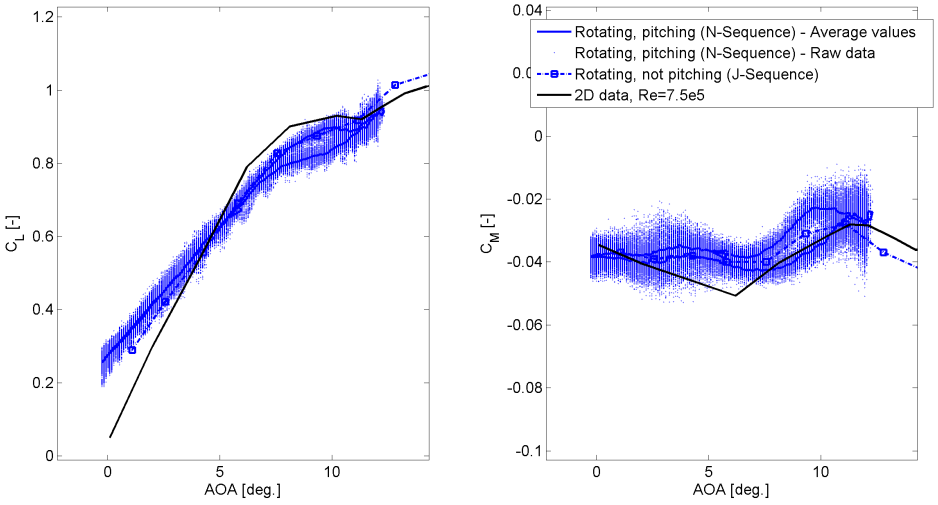

FIGURE A.49: Case N47170: Lift and moment polars at $\alpha_M = 6.0°$, $\alpha_\Omega = 6.28°$, $r/R = 0.80$, $K = 0.0119$.

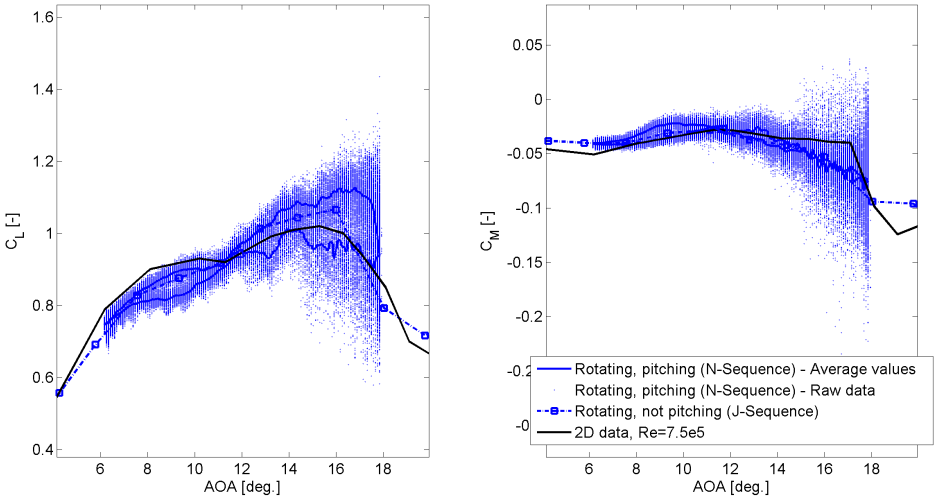

FIGURE A.50: Case N47180: Lift and moment polars at $\alpha_M = 12.0°$, $\alpha_\Omega = 5.84°$, $r/R = 0.80$, $K = 0.0119$.

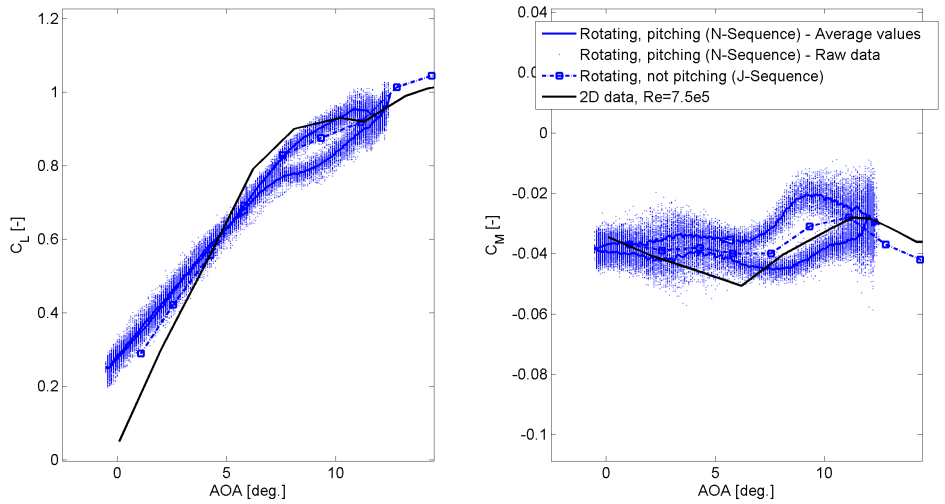

FIGURE A.51: Case N47230: Lift and moment polars at $\alpha_M = 6.0°$, $\alpha_\Omega = 6.50°$, $r/R = 0.80$, $K = 0.0239$.

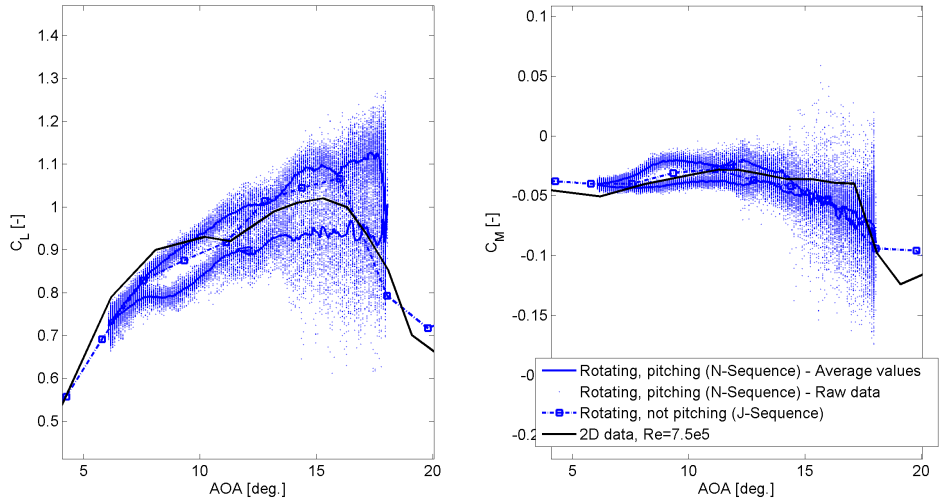

FIGURE A.52: Case N47240: Lift and moment polars at $\alpha_M = 12.1°$, $\alpha_\Omega = 5.98°$, $r/R = 0.80$, $K = 0.0239$.

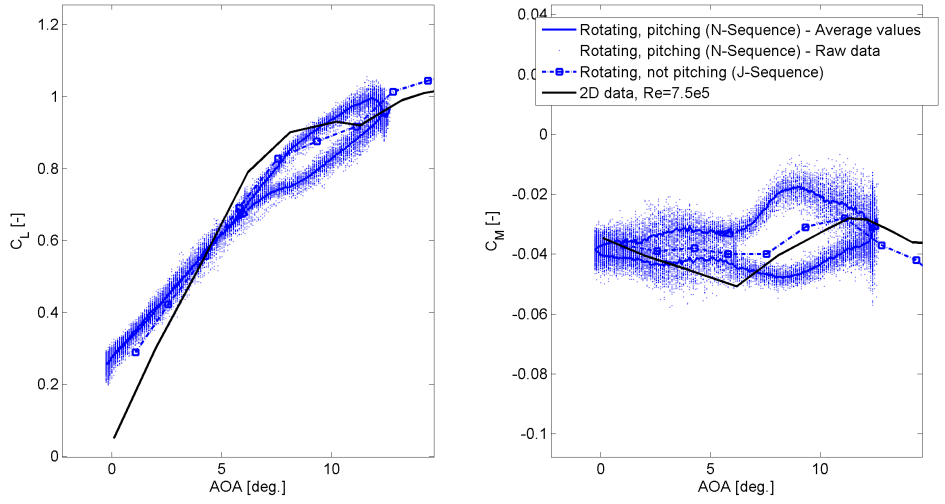

FIGURE A.53: Case N47290: Lift and moment polars at $\alpha_M = 6.2°$, $\alpha_\Omega = 6.46°$, $r/R = 0.80$, $K = 0.0358$.

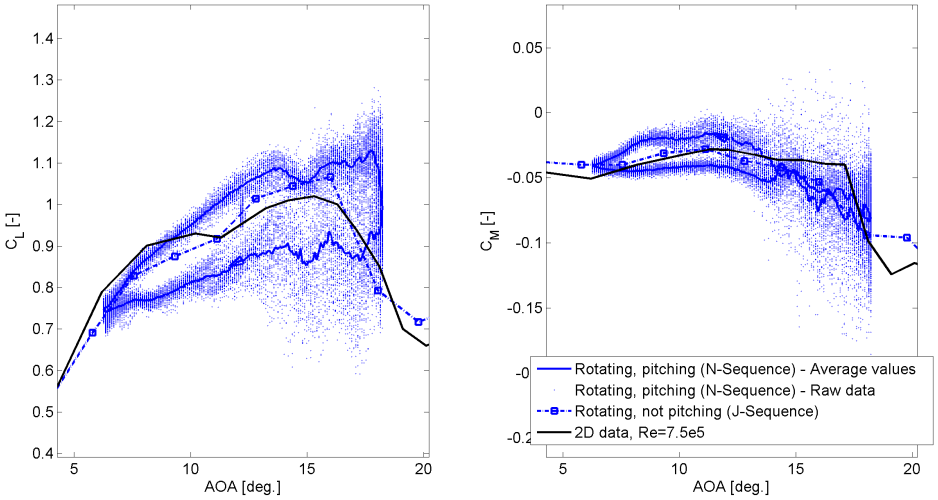

FIGURE A.54: Case N47300: Lift and moment polars at $\alpha_M = 12.2°$, $\alpha_\Omega = 5.98°$, $r/R = 0.80$, $K = 0.0358$.

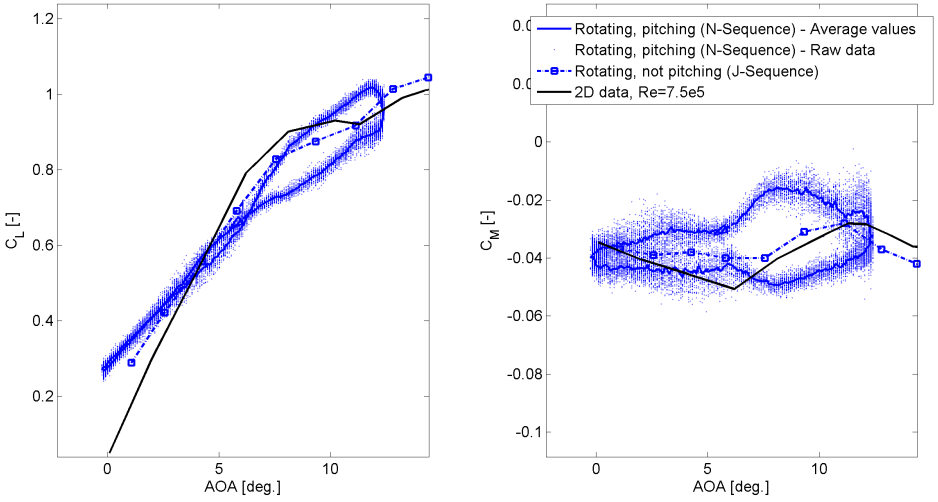

FIGURE A.55: Case N47350: Lift and moment polars at $\alpha_M = 6.1°$, $\alpha_\Omega = 6.33°$, $r/R = 0.80$, $K = 0.0477$.

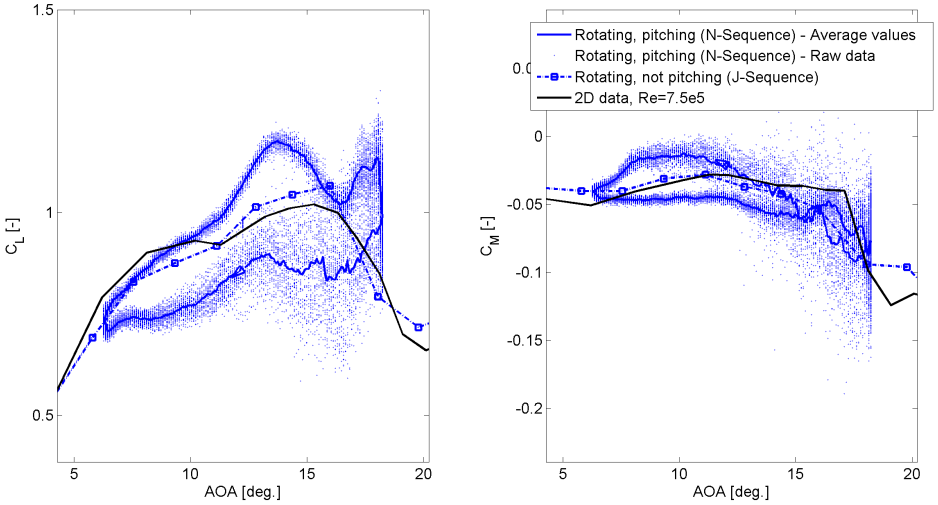

FIGURE A.56: Case N47360: Lift and moment polars at $\alpha_M = 12.2°$, $\alpha_\Omega = 5.98°$, $r/R = 0.80$, $K = 0.0477$.

A.5 Radial location $r/R = 0.95$

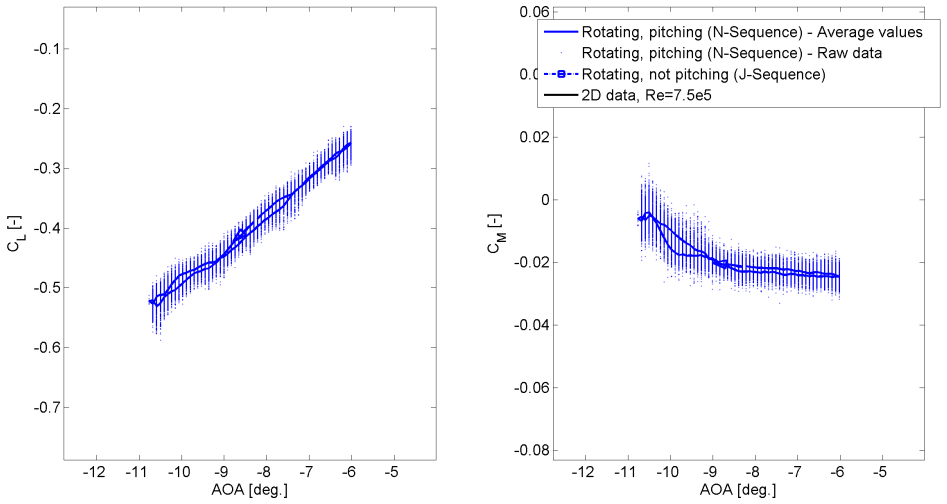

FIGURE A.57: Case N47020: Lift and moment polars at $\alpha_M = -8.4°$, $\alpha_\Omega = 2.37°$, $r/R = 0.95$, $K = 0.0207$.

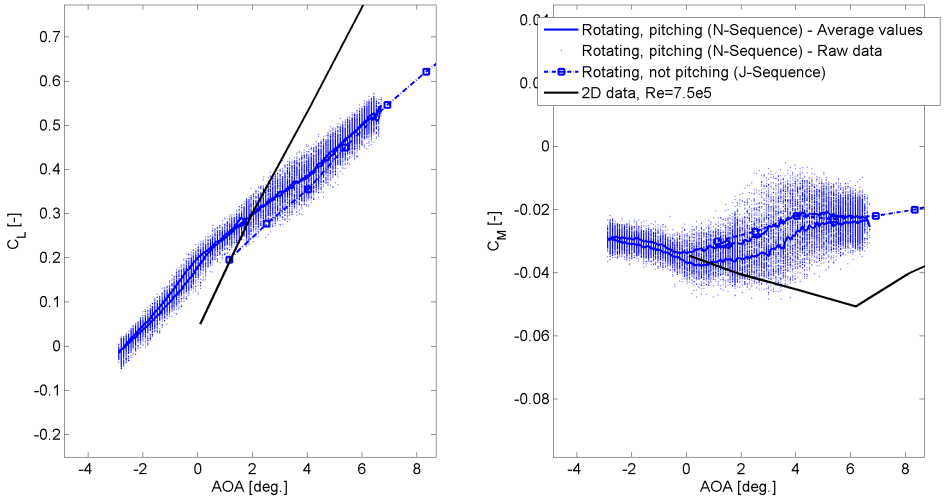

FIGURE A.58: Case N47030: Lift and moment polars at $\alpha_M = 1.9°$, $\alpha_\Omega = 4.79°$, $r/R = 0.95$, $K = 0.0207$.

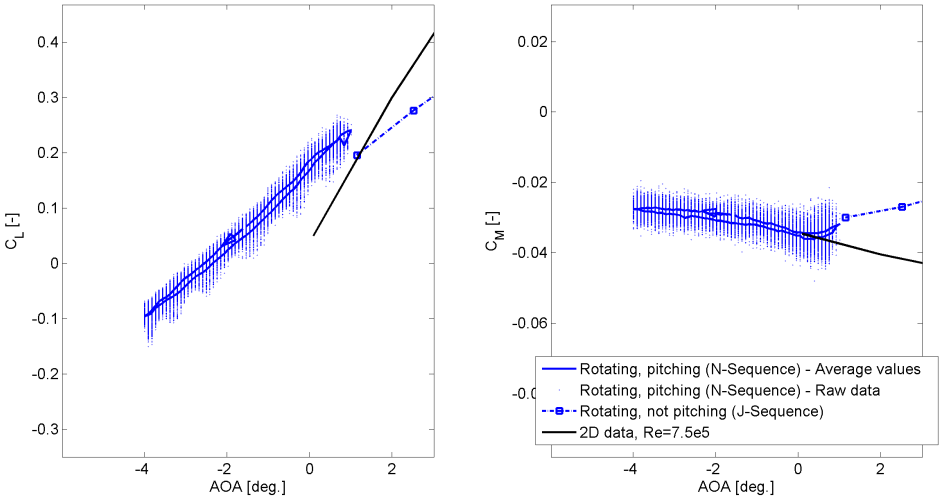

FIGURE A.59: Case N47050: Lift and moment polars at $\alpha_M = -1.5°$, $\alpha_\Omega = 2.50°$, $r/R = 0.95$, $K = 0.0248$.

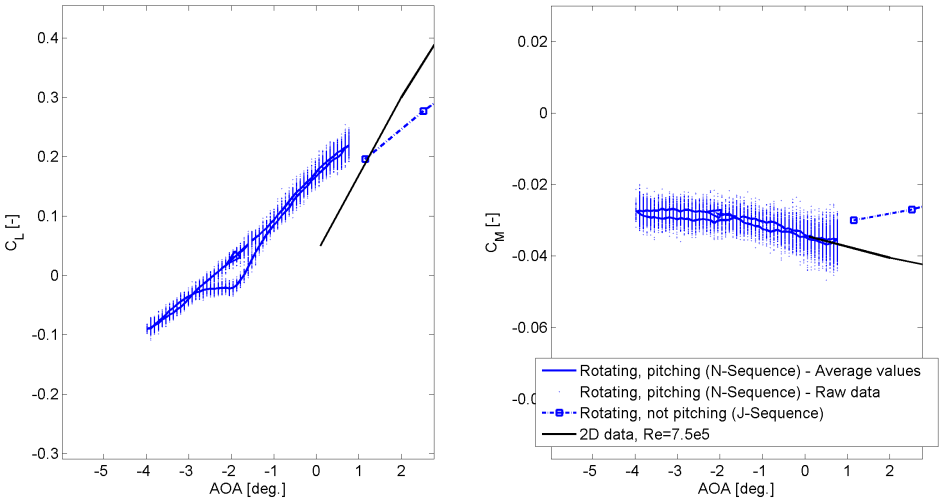

FIGURE A.60: Case N47090: Lift and moment polars at $\alpha_M = -1.6°$, $\alpha_\Omega = 2.37°$, $r/R = 0.95$, $K = 0.0331$.

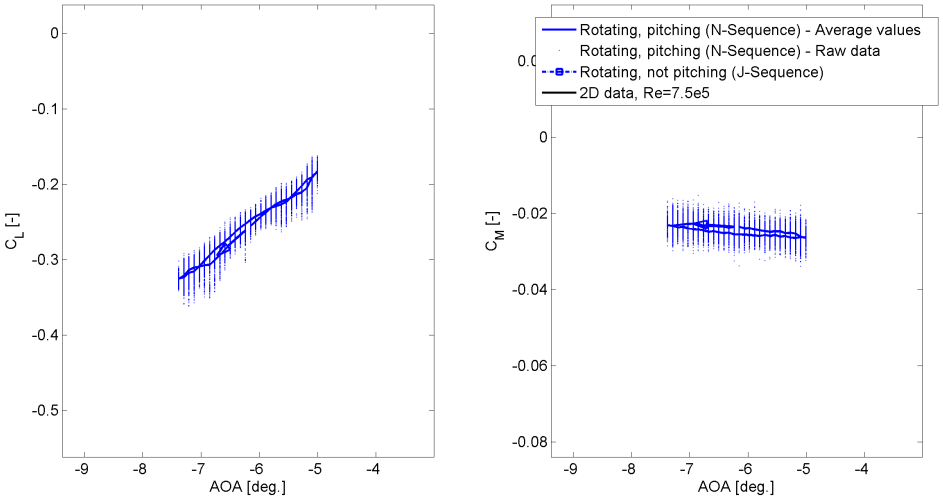

FIGURE A.61: Case N47140: Lift and moment polars at $\alpha_M = -6.2°$, $\alpha_\Omega = 1.19°$, $r/R = 0.95$, $K = 0.0413$.

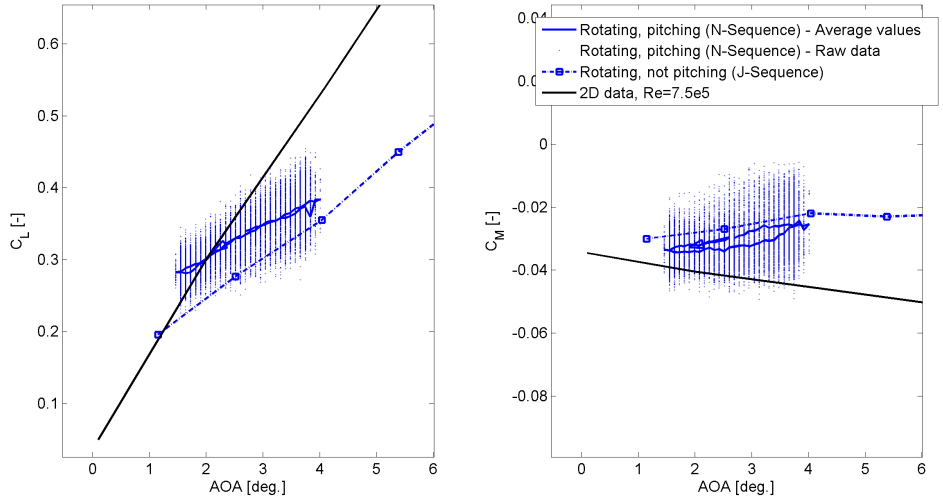

FIGURE A.62: Case N47150: Lift and moment polars at $\alpha_M = 2.7°$, $\alpha_\Omega = 1.27°$, $r/R = 0.95$, $K = 0.0413$.

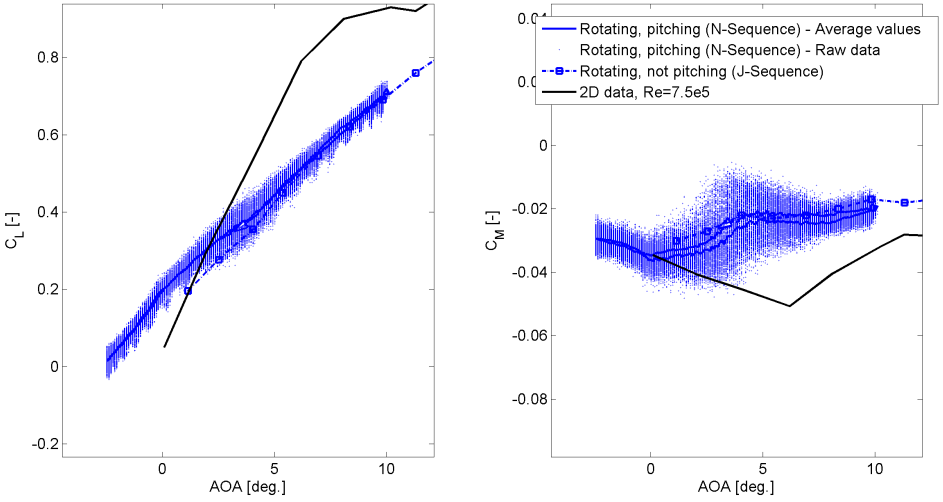

FIGURE A.63: Case N47170: Lift and moment polars at $\alpha_M = 3.8°$, $\alpha_\Omega = 6.28°$, $r/R = 0.95$, $K = 0.0083$.

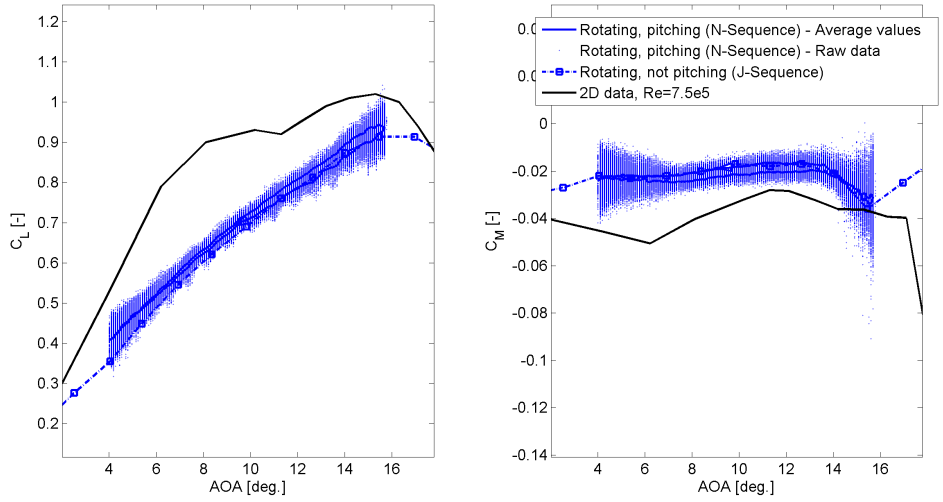

FIGURE A.64: Case N47180: Lift and moment polars at $\alpha_M = 9.8°$, $\alpha_\Omega = 5.84°$, $r/R = 0.95$, $K = 0.0083$.

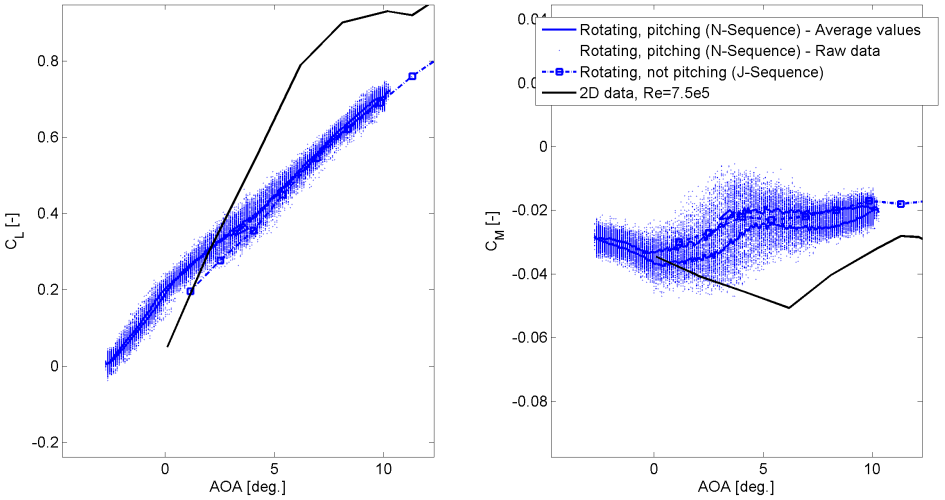

FIGURE A.65: Case N47230: Lift and moment polars at $\alpha_M = 3.8°$, $\alpha_\Omega = 6.50°$, $r/R = 0.95$, $K = 0.0165$.

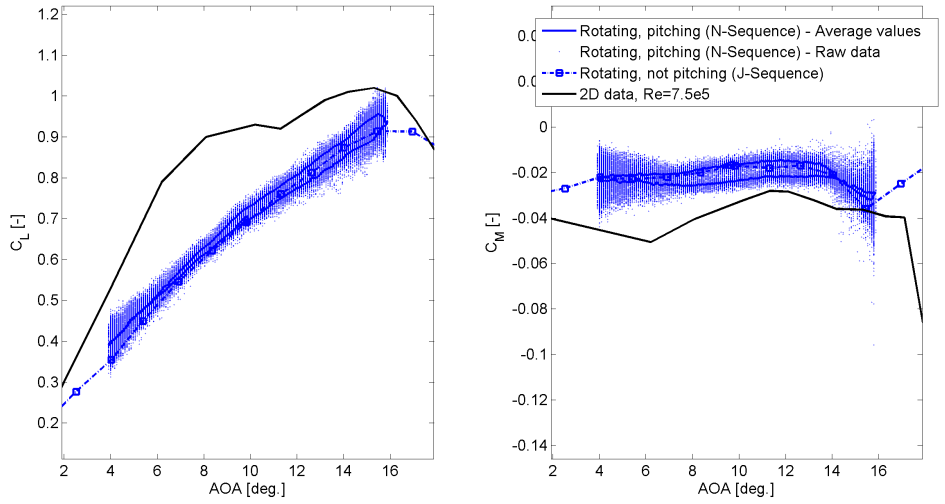

FIGURE A.66: Case N47240: Lift and moment polars at $\alpha_M = 9.9°$, $\alpha_\Omega = 5.98°$, $r/R = 0.95$, $K = 0.0165$.

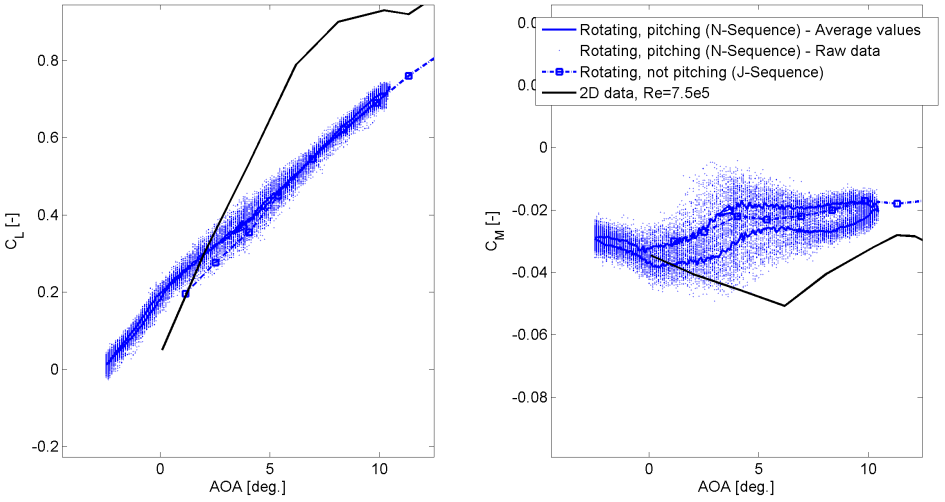

FIGURE A.67: Case N47290: Lift and moment polars at $\alpha_M = 4.0°$, $\alpha_\Omega = 6.46°$, $r/R = 0.95$, $K = 0.0248$.

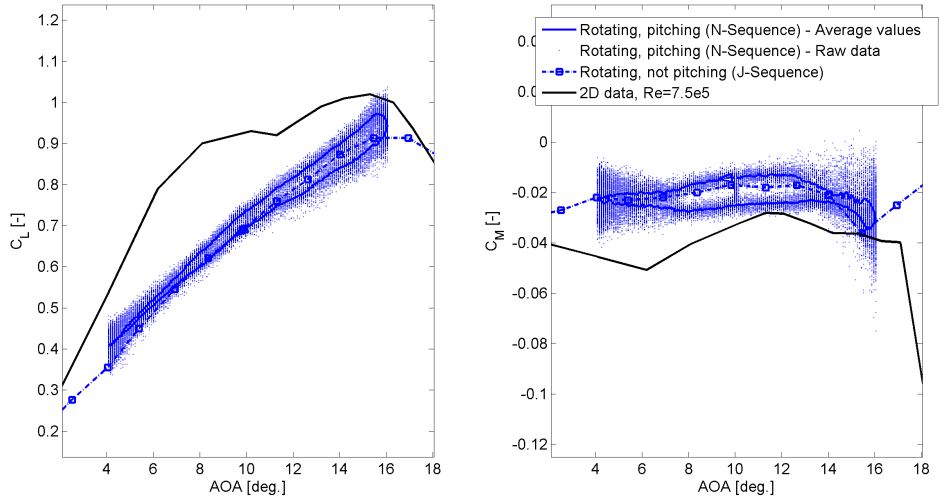

FIGURE A.68: Case N47300: Lift and moment polars at $\alpha_M = 10.1°$, $\alpha_\Omega = 5.98°$, $r/R = 0.95$, $K = 0.0248$.

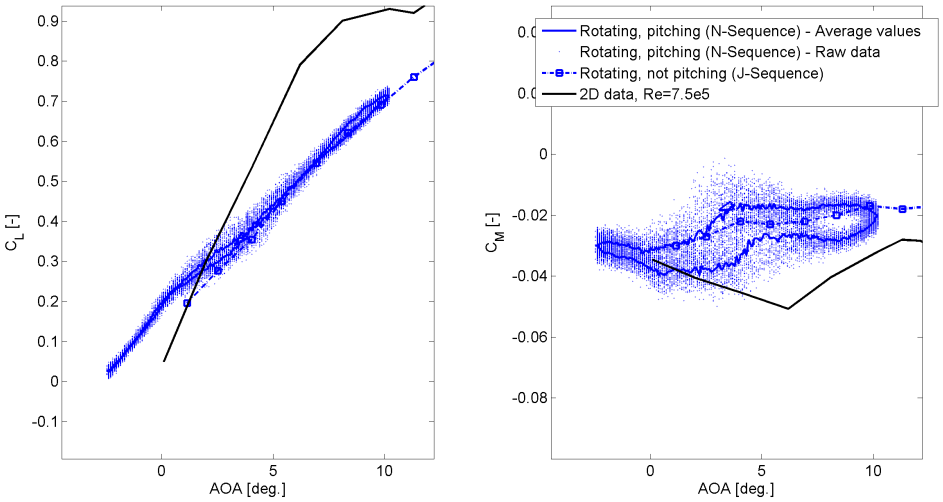

FIGURE A.69: Case N47350: Lift and moment polars at $\alpha_M = 3.9°$, $\alpha_\Omega = 6.33°$, $r/R = 0.95$, $K = 0.0331$.

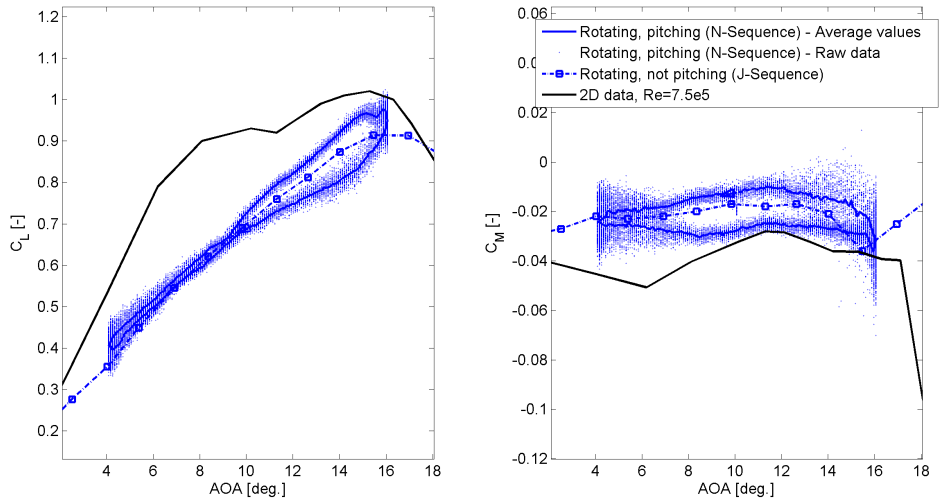

FIGURE A.70: Case N47360: Lift and moment polars at $\alpha_M = 10.1°$, $\alpha_\Omega = 5.98°$, $r/R = 0.95$, $K = 0.0331$.

Bibliography

[1] J.G. Schepers, K. Boorsma, T. Cho, S. Gomez-Iradi, P. Schaffarczyk, A. Jeromin, W.Z. Shen, T. Lutz, K. Meister, B. Stoevesandt, S. Schreck, D. Micallef, R. Pereira, T. Sant, H. Madsen, and N. Sorensen. Final report of IEA task 29, mexnext (phase 1): Analysis of mexico wind tunnel measurements. Technical Report ECN-E–12-004, ECN, 2012.

[2] M.M. Hand, D.A. Simms, L.J. Fingersh, D.W. Jager, J.R. Cotrell, S. Schreck, and S.M. Larwood. Unsteady Aerodynamics Experiment Phase VI: Wind Tunnel Test Configurations and Available Data Campaigns. Technical Report NREL/TP-500-29955, NREL, Golden, CO, USA, December 2001.

[3] K. Boorsma and J.G. Schepers. Description of experimental setup. Technical Report ECN-X–11-120, ECN, 2011. Confidential report.

[4] M.H. Hansen, M. Gaunaa, and H.A. Madsen. A beddoes-leishman type dynamic stall model in state-space and indicial formulations. Technical Report Risø-R-1354, Risø-DTU, June 2004.

[5] International Energy Agency (IEA). World energy outlook 2012. doi: 10.1787/weo-2012-en.

[6] J.G. Schepers. *Engineering models in wind energy aerodynamics: Development, implementation and analysis using dedicated aerodynamic measurements*. PhD thesis, Technische Universiteit Delft, 2012.

[7] Jens Nørkær Sørensen. Aerodynamic aspects of wind energy conversion. *Annual Review of Fluid Mechanics*, 43:427–448, 2011.

[8] H. Glauert. *Airplane Propellers*, volume IV, chapter Aerodynamic Thoery, pages 169–360. New York: Springer, 1935.

[9] M.O.L. Hansen and J. Johansen. Tip studies using CFD and computation with tip loss models. *Wind Energy*, 7:343–356, 2004.

[10] W.Z. Shen, R. Mikkelsen, and J.N. Sørensen. Tip loss correction for wind turbine computations. *Wind Energy*, 8:457–475, 2005.

[11] E. Branlard. Wind turbine tip-loss corrections: Review, implementation and investigation of new models. Master's thesis, Technical University of Denmark (DTU), 2011.

[12] M.O.L. Hansen. *Aerodynamics of Wind Turbines.* The Cromwell Press, UK, 1 edition, 2000.

[13] J.G. Leishman. *Principles of Helicopter Aerodynamics*, chapter 9. Cambridge Aerospace. Cambridge University Press, 2006. ISBN 9780521858601.

[14] H. Snel, J.G. Schepers, and B. Montgomerie. The MEXICO project (Model Experiments in Controlled Conditions): The database and first results of data processing and interpretation. In *Journal of Physics: Conference Series 75*, 2007.

[15] Gijs A.M. van Kuik. The lanchester–betz–joukowsky limit. *Wind Energy*, 10(3): 289–291, 2007. ISSN 1099-1824. doi: 10.1002/we.218.

[16] Tony Burton, David Sharpe, Nick Jenkins, and Ervin Bossanyi. *Aerodynamics of Horizontal-Axis Wind Turbines*, pages 41–172. John Wiley & Sons, Ltd, 2002. ISBN 9780470846063. doi: 10.1002/0470846062.ch3.

[17] F. Rasmussen and H.A. Madsen. Derivation of three-dimensional airfoil data on the basis of experiment and theory. In *Proc. of the 2nd Symposium on Aerodynamics of Wind Turbines*, pages 150–159, Lyngby, Denmark, 1988. IEA.

[18] W.H.H. Banks and G.E. Gadd. Delaying effect of rotation on laminar separation. *AIAA*, 1(4):941–942, 1963.

[19] W.J. McCroskey. Measurements of boundary layer transition, separation and streamline direction on rotating blades. Technical Report TN D-6321, NASA, 1971.

[20] D.H. Wood. A three-dimensional analysis of stall-delay on a horizontal-axis wind turbine. *Journal of Wind Engineering and Industrial Aerodynamics*, 37:1–14, 1991.

[21] J. C. Narramore and R. Vermeland. Navier-stokes calculations of inboard stall delay due to rotation. *Journal of aircraft*, 29(1):73–78, 1992.

[22] H. Snel, R. Houwink, and J. Bosschers. Sectional prediction of lift coefficients on rotating wind turbine blades in stall. Technical Report ECN-C–93-052, 1994.

[23] C. Lindenburg. Modeling of rotational augmentation based on engineering considerations and measurements. In *Proc. of the European Wind Energy Conference*, London, UK, 2004.

[24] Z. Du and M.S. Selig. A 3-D stall-delay model for horizontal axis wind turbine performance prediction. In *36th AIAA Aerospace Sciences Meeting and Exhibit*. ASME Wind Energy Symposium, Reno, NV, USA, 1998. AIAA-98-0021.

[25] Zhaohui Du and M. S. Selig. The effect of rotation on the boundary layer of a wind turbine blade. *Renewable Energy*, 20(2):167–181, 2000.

[26] W.Z. Shen and J.N. Sørensen. Quasi-3D Navier–Stokes model for a rotating airfoil. *Journal of Computational Physics*, 150(2):518–548, April 1999. ISSN 0021-9991. doi: 10.1006/jcph.1999.6203.

[27] G.P. Corten. Inviscid stall model. In *Proc. of the 14th IEA Symposium*, USA, 2000. NREL.

[28] P.K. Chaviaropoulos and M.O.L. Hansen. Investigating three-dimensional and rotational effects on wind turbine blades by means of a quasi-3d navier-stokes solver. *Journal of Fluids Engineering*, 122:330–336, 2000.

[29] C. Bak, J. Johansen, and P.B. Andersen. Three-dimensional corrections of airfoil characteristics based on pressure distributions. In *Proc. of the European Wind Energy Conference*, Athens, Greece, 2006.

[30] C. Sicot, P. Devinant, S. Loyer, and J. Hureau. Rotational and turbulence effects on a wind turbine blade. investigation of the stall mechanisms. *Journal of Wind Engineering and Industrial Aerodynamics*, 96(8–9):1320–1331, August 2008. ISSN 0167-6105. doi: 10.1016/j.jweia.2008.01.013.

[31] Horia Dumitrescu, Vladimir Cardos, and Alexandru Dumitrache. Modelling of inboard stall delay due to rotation. In *Journal of Physics: Conference Series*, volume 75, 2007. doi: 0.1088/1742-6596/75/1/012022.

[32] J.M. Savino and T.W. Nyland. Wind turbine flow visualization studies. Technical report, NASA Lewis research center, 1985.

[33] A. Gross, H. F. Fasel, T. Friederich, and M. J. Kloker. Numerical investigation of rotational augmentation for s822 wind turbine airfoil. *Wind Energy*, 15(8):983–1007, 2012. ISSN 1099-1824. doi: 10.1002/we.540.

[34] S. Guntur and N.N. Sørensen. Comments on a recent research article by gross et al. (2012). *Wind Energy*, August 2013. Accepted for publication.

[35] A. Bjorck. Dynamic stall and three-dimensional effects. Technical Report EC DXGII Joule II Project No. JOU2-CT93-0345, The aeronautical institute of Sweden, 1995.

[36] Horia Dumitrescu and V. Cardos. Inboard boundary layer state on wind turbine blades. *ZAMM-Journal of Applied Mathematics and Mechanics/Zeitschrift fur Angewandte Mathematik und Mechanik*, 89(3):163–173, 2009.

[37] H. Dumitrescu and V. Cardos. Inboard stall delay due to rotation. *Journal of Aircraft*, 49(1):101–107, 2012.

[38] L.W. Carr. Progress in analysis and prediction of dynamic stall. *Journal of aircraft*, 25(1):7–17, January 1988.

[39] L. E. Ericsson and J. P. Reding. Fluid mechanics of dynamic stall part i. unsteady flow concepts. *Journal of fluids and structures*, 2(1):1–33, 1988.

[40] L. E. Ericsson and J. P. Reding. Fluid mechanics of dynamic stall part II. prediction of full scale characteristics. *Journal of Fluids and Structures*, 2(2):113–143, 1988.

[41] J. Katz and A. Plotkin. *Low-Speed Aerodynamics*, chapter 2. Cambridge Aerospace Series. Cambridge University Press, 2001. ISBN 9780521665520.

[42] S.J. Schreck, M. Robinson, M. Hand, and D. Simms. Hawt dynamic stall response asymetries under yawed flow conditions. *Wind Energy*, 3:215–232, 2000. doi: 10.1002/we.40.

[43] S.J. Schreck, M.C. Robinson, M.M. Hand, and D.A. Simms. Blade dynamic stall vortex kinematics for a horizontal axis wind turbine in yawed conditions. *J. Solar Energy Engineering*, 123:272–281, 2001. doi: 10.1115/1.1408307.

[44] Stig Øye. Dynamic stall simulated as a time lag of separation. In *Proc. of EWEC*, Thessaloniki, Greece, October 1994.

[45] J.W. Larsen, S.R.K. Nielsen, and S. Krenk. Dynamic stall model for wind turbine airfoils. *Journal of Fluids and Structures*, 23(7):959 – 982, 2007. ISSN 0889-9746. doi: http://dx.doi.org/10.1016/j.jfluidstructs.2007.02.005.

[46] F. Rasmussen, J. T. Petersen, and H. A. Madsen. Dynamic stall and aerodynamic damping. *Journal of Solar Energy Engineering*, 121(3):150–155, August 1999. ISSN 0199-6231. doi: 10.1115/1.2888426.

[47] S.J. Schreck and M. Robinson. Rotational augmentation of horizontal axis wind turbine blade aerodynamic response. *Wind Energy*, 5:133–150, 2002. doi: 10.1002/we.68.

[48] Ricardo Balbino dos Santos Pereira. Validating the Beddoes-Leishman Dynamic Stall Model in the Horizontal Axis Wind Turbine Environment. 2010. URL https://dspace.ist.utl.pt/bitstream/2295/725322/1/TeseIST_Final.pdf.

[49] J.G. Leishman and T.S. Beddoes. A semi-empirical model for dynamic stall. *Journal of the American Helicopter Society*, 34(3):3–17, 1989. doi: 10.4050/JAHS.34.3.

[50] Leonardo Bergami, Mac Gaunaa, and Joachim Heinz. Indicial lift response function: an empirical relation for finite-thickness airfoils, and effects on aeroelastic simulations. *Wind Energy*, 16(5):681–693, 2013. ISSN 1099-1824. doi: 10.1002/we.1516.

[51] Lucas Pascal. Analysis of mexico measurements. Technical Report ECN-Memo-09-010, Energy Research Center of the Netherlands (ECN), January 2009.

[52] S. Guntur and N.N. Sørensen. An evaluation of several methods of determining the local angle of attack on wind turbine blades. In *Proc. of the Science of making Torque from Wind*, Oldenburg, Germany, October 2012.

[53] Niels N. Sørensen. CFD modelling of laminar-turbulent transition for airfoils and rotors using the $\gamma - \widetilde{\mathrm{Re}}_\theta$ model. *Wind Energy*, 12(8):715–733, 2009. ISSN 1099-1824. doi: 10.1002/we.325.

[54] A. Bechmann, N.N. Sørensen, and F. Zahle. CFD simulation of the mexico rotor. *Wind Energy*, 14:677–689, 2011.

[55] C. Lindenburg. Investigation into rotor blade aerodynamics: Analysis of the stationary measurements on the UAE phase-VI rotor in the NASA-Ames wind tunnel. Technical Report ECN-C–03-025, ECN, The Netherlands, 2003.

[56] S. Guntur, C. Bak, and N.N. Sørensen. Analysis of 3D Stall Models for Wind Turbine Blades Using Data from the MEXICO Experiment. In *Proc. of the 13th International Conference on Wind Engineering*, Amsterdam, the Netherlands, 2011.

[57] M.O.L. Hansen, N.N. Sørensen, J.N. Sørensen, and J.A. Mikkelsen. Extraction of lift, drag and angle of attack from computed 3D viscous flow around a rotating blade. In *Proc. of the European Wind Energy Conference*, pages 499–501, Dublin, 1997.

[58] J. Johansen and N.N. Sørensen. Airfoil charecteristics from 3D CFD rotor computations. *Wind Energy*, 7:283–294, 2004.

[59] C. Bak, N. Troldborg, and H.A. Madsen. DAN-AERO MW: Measured airfoil characteristics for a MW rotor in atmospheric conditions. Proc. of EWEA, 2011.

[60] H. Snel, R. Houwink, J. Bosschers, W.J. Piers, G.J.W. van Bussel, and A. Bruining. Sectional prediction of 3-D effects for stalled flow on rotating blades and comparison with measurements. In *Proc. of the European Community Wind Energy Conference*, pages 395–399, March 1993.

[61] A.D. Gardner and K. Richter. Influence of rotation on dynamic stall. *Journal of the American Helicopter Society*, 58:032001, 2013. doi: 10.4050/JAHS.58.032001.

[62] S. Guntur and N.N. Sørensen. A study on rotational augmentation using CFD analysis of flow in the inboard region of the mexico rotor blades. *Wind Energy*, August 2013. Accepted for publication.

[63] B. Akay, D. Ragni, C.J. Simão Ferreira, and G.J.W. van Bussel. Experimental investigation of the root flow in a horizontal axis wind turbine. *Wind Energy*, pages n/a–n/a, 2013. ISSN 1099-1824. doi: 10.1002/we.1620.

[64] Alvaro Gonzalez and Xabier Munduate. Three-dimensional and rotational aerodynamics on the NREL phase VI wind turbine blade. *Journal of Solar Energy Engineering*, 130(3):031008, 2008. doi: 10.1115/1.2931506.

[65] Srinivas Guntur, Niels N. Sørensen, and Scott Schreck. Dynamic stall on rotating airfoils: A look at the n-sequence data from the NREL phase VI experiment. *Key Engineering Materials*, 569-570:611–619, July 2013. ISSN 1662-9795. doi: 10.4028/www.scientific.net/KEM.569-570.611.

[66] Srinivas Guntur, Niels. N. Sørensen, Scott Schreck, and Leonardo Bergami. Dynamic stall in the inboard parts of the NREL Phase VI rotor operating in axial and continuously pitching conditions. *Wind Energy*, August 2013. (submitted).

[67] N.N. Sørensen and S. Schreck. Computation of the national renewable energy laboratory Phase-VI rotor in pitch motion during standstill. *Wind Energy*, 15: 425–442, 2012.

[68] Frederik Zahle, Christian Bak, Srinivas Guntur, Niels Troldborg, and Niels N. Sørensen. Comprehensive Aerodynamic Analysis of a 10 MW Wind Turbine Rotor Using 3D CFD. In *52nd Aerospace Sciences Meeting*, Maryland, USA, January 2014. AIAA.

[69] H. Snel. Scaling laws for the boundary layer flow on rotating wind turbines. *Proceedings of the fourth IEA symposium on the aerodynamics of wind turbines*, January 1991.

[70] N.N. Sørensen, J.A. Michelsen, and S. Schreck. Navier–Stokes Predictions of the NREL Phase VI Rotor in the NASA Ames 80 ft × 120 ft Wind Tunnel. *Wind Energy*, 5:151–169, 2002.

[71] L. Prandtl. Applications of modern hydrodynamics to aeronautics. Technical Report NACA Report No. 116, Gottingen University, 1921.

[72] W.Z. Shen, M.O.L. Hansen, and J.N. Sørensen. Determination of angle of attack (aoa) for rotating blades. In Joachim Peinke, Peter Schaumann, and Stephan Barth, editors, *Wind Energy*, Proceedings of the Euromech Colloquium, pages 205–209. Springer Berlin Heidelberg, 2007. ISBN 978-3-540-33865-9. doi: 10.1007/978-3-540-33866-6_37.

[73] W.Z. Shen, M.O.L. Hansen, and J.N. Sørensen. Determination of the angle of attack on rotor blades. *Wind Energy*, 12:91–98, 2009.

[74] S.P. Breton, F.N. Coton, and G. Moe. A study on rotational effects and different 3D stall models using a prescribed wake vortex scheme and NREL Phase VI experiment data. *Wind energy*, 11:459–482, 2008.

[75] T. Sant, G. van Kuik, and G.J.W van Bussel. Estimating the Angle of Attack from Blade Pressure Measurements on the NREL Phase VI Rotor Using a Free Wake Vortex Model: Axial Conditions. *Wind Energy*, 9:549–577, 2006.

[76] G. Yu, X. Shen, X. Zhu, and Z. Du. An insight into the separate flow and stall delay for HAWT. *Renewable Energy*, 36:69–76, 2011.

[77] J.A. Michelsen. Basis3d - a platform for development of multiblock pde solvers. Technical Report AFM 92-05, Technical University of Denmark (DTU), 1992.

[78] J.A. Michelsen. Block structured multigrid solution of 2d and 3d elliptic pde's. Technical Report AFM 94-06, Technical University of Denmark (DTU), 1994.

[79] N.N. Sørensen. *General Purpose Flow Solver Applied to Flow over Hills.* PhD thesis, Technical University of Denmark (DTU), 1994. Risø-R-827-(EN).

[80] Anders Ahlström. *Aeroelastic Simulation of Wind Turbine Dynamics.* PhD thesis, Department of Mechanics, Royal Institute of Technology, SE-100 44 Stockholm, Sweden, 2005.

[81] Niels N. Sørensen, A. Bechmann, P-E. Réthoré, and F. Zahle. Near wake reynolds-averaged Navier–Stokes predictions of the wake behind the MEXICO rotor in axial and yawed flow conditions. *Wind Energy*, 2012. ISSN 1099-1824. doi: 10.1002/we.1559.

[82] S. Schreck, T. Sant, and D. Micallef. Rotational Augmentation Disparities in the MEXICO and UAE Phase VI Experiments. In *Proc. of Science of Making Torque From Wind*, number NREL/CP-500-47759, 2010.

[83] Niels N. Sørensen and H.Aa. Madsen. Modelling of transient wind turbine loads during pitch motion. In *Proceedings (online)*, Athens, Greece, 2006. European Wind Energy Association.

[84] E.J. Jumper, S.J. Schreck, and R.L. Dimmick. Lift-Curve Characteristics for an Airfoil Pitching at Constant Rate. In *AIAA 24th Aerospace Sciences Meeting*, number AIAA-86-0117, Reno, Nevada, USA, January 1986.

[85] J. Gordon Leishman. Challenges in modelling the unsteady aerodynamics of wind turbines. *Wind Energy*, 5(2-3):85–132, 2002. ISSN 1099-1824. doi: 10.1002/we.62.

[86] R.B. Green, R.A.McD. Galbraith, and A.J. Niven. Measurements of the dynsmic stall vortex convection speed. *The aeronautical journal of the royal aeronautical society*, 96(958):319–325, October 1992.

[87] M.R. Visbal. On the formation and control of the dynamic stall vortex on a pitching airfoil. In *29th aerospace sciences meeting*, Reno, Nevada, USA, January 1991. AIAA.

[88] J. Johansen, N.N. Sørensen, and S.J. Schreck. Detached-Eddy Simulation of Flow Around the NREL Phase VI Blade. *Wind Energy*, 5:185–197, 2002.

[89] Leonardo Bergami and Mac Gaunaa. *ATEFlap Aerodynamic Model, a dynamic stall model including the effects of trailing edge flap deflection.* Denmark. Forskningscenter Risoe. Risoe-R. Danmarks Tekniske Universitet, Risø Nationallaboratoriet for Bæredygtig Energi, 2012. ISBN 978-87-550-3934-6.

[90] T. Theodorsen. General theory of aerodynamic instability and the mechanism of flutter. *NACA Report*, 496, 1935.

[91] J.g. Holierhoek, J.b. de Vaal, A.h. van Zuijlen, and H. Bijl. Comparing different dynamic stall models. *Wind Energy*, 16(1):139–158, 2013. ISSN 1099-1824. doi: 10.1002/we.548.

[92] M.O.L. Hansen, J.N. Sørensen, S. Voutsinas, N. Sørensen, and H.Aa. Madsen. State of the art in wind turbine aerodynamics and aeroelasticity. *Progress in Aerospace Sciences*, 42(4):285–330, June 2006. ISSN 0376-0421. doi: 10.1016/j.paerosci.2006.10.002.

[93] Alvaro Gonzalez and Xabier Munduate. Unsteady modelling of the oscillating s809 aerofoil and nrel phase vi parked blade using the beddoes-leishman dynamic stall model. *Journal of Physics: Conference Series*, 75(1):012020, 2007.

[94] J. A. Michelsen. Basis3D - A Platform for Development of Multiblock PDE Solvers. Technical Report AFM 92-05, Technical University of Denmark, Department of Fluid Mechanics, Technical University of Denmark, December 1992.

[95] J. A. Michelsen. Block structured Multigrid solution of 2D and 3D elliptic PDE's. Technical Report AFM 94-06, Technical University of Denmark, Department of Fluid Mechanics, Technical University of Denmark, May 1994.

[96] N. N. Sørensen. General Purpose Flow Solver Applied to Flow over Hills. Risø-R-827-(EN), Risø National Laboratory, Roskilde, Denmark, June 1995.

[97] F. R. Menter. Zonal Two Equation k-ω Turbulence Models for Aerodynamic Flows. *AIAA paper 1993-2906*, 1993.

[98] F.R. Menter and M. Kuntz. *The Aerodynamics of Heavy Vehicles: Trucks, Buses, and Trains*, volume 19 of *Lecture Notes in Applied and Computational Mechanics*, chapter Adaptation of Eddy-Viscosity Turbulence Models to Unsteady Separated Flow Behind Vehicles, pages 339–352. Springer, 2004.

[99] M. Strelets. Detached Eddy Simulation of Massively Separated Flows. AIAA Paper 2001-0879, Russian Scientific Center "Applied Chemistry" St. Petersburg, 2001.

[100] F. R. Menter, R. B. Langtry, S. R. Likki, Y. B. Suzen, P. G. Huang, and S. Völker. A Correlation-Based Transition Model Using Local Variables, Part I - Model Formulation. In *Proceedings of ASME Turbo Expo 2004, Power for Land, Sea, and Air*, Vienna, Austria, June 14-17 2004. ASME. GT2004-53452.

[101] Franck Bertagnolio, Flemming Rasmussen, Niels N. Sørensen, Jeppe Johansen, and Helge Aagaard Madsen. A stochastic model for the simulation of wind turbine blades in static stall. *Wind Energy*, 13(4):323–338, 2010.

[102] J. H. Ferziger and M. Peric. *Computational Methods for Fluid Dynamics*. Springer-Verlag, 1996.

[103] R. B. Langtry, J. Gola, and F. R. Menter. Predicting 2D Airfoil and 3D Wind Turbine Rotor Performance using a Transition Model for General CFD Codes. AIAA-paper-2006-0395, 2006.

DTU Wind Energy is a department of the Technical University of Denmark with a unique integration of research, education, innovation and public/private sector consulting in the field of wind energy. Our activities develop new opportunities and technology for the global and Danish exploitation of wind energy. Research focuses on key technical-scientific fields, which are central for the development, innovation and use of wind energy and provides the basis for advanced education at the education.

We have more than 240 staff members of which approximately 60 are PhD students. Research is conducted within nine research programmes organized into three main topics: Wind energy systems, Wind turbine technology and Basics for wind energy.

Danmarks Tekniske Universitet
DTU Vindenergi
Nils Koppels Allé
Bygning 403
2800 Kgs. Lyngby
Phone 45 25 25 25

info@vindenergi.dtu.dk
www.vindenergi.dtu.dk

ISBN 978-87-92896-57-5